ABSTRACT

Depositional and Diagenetic Controls on Reservoir Quality and Petrophysical Response of the DeBroeck Member of the Rodessa Formation in Northwest Louisiana

Ian M. Byram, M.S.

Committee Chairperson: Stephen I. Dworkin, Ph.D.

The DeBroeck Member of the Lower Cretaceous Rodessa Formation is an overlooked hydrocarbon reservoir in Northwest Louisiana. The formation was deposited on a carbonate platform within the North Louisiana Salt Basin. Core analysis identified fourteen lithofacies within the DeBroeck Member with maximum porosity and permeability values of 21.3% and 49.6 mD. The lithofacies indicate a shallow, open marine depositional environment. Porosity is present as primary interparticle/intraparticle and secondary moldic. Petrographic and SEM imaging show that porosity and permeability are affected by carbonate mud recrystallization and calcite, anhydrite, and pyrite cementation. Diagenesis occurred in three stages: marine, meteoric, and burial, with all stages affecting porosity and permeability. Advanced porosity analysis determined that large amounts of microporosity/irreducible water are present within the formation, causing the resistivity log response to appear 'water-wet'. Backscatter SEM image analysis shows that pyrite is locally abundant and interconnected within stylolites, which also affects the formation's petrophysical response.

Depositional and Diagenetic Controls on Reservoir Quality and Petrophysical Response of the DeBroeck Member of the Rodessa Formation in Northwest Louisiana

by

Ian M. Byram, B.S., B.B.A

A Thesis

Approved by the Department of Geosciences

_____

Stacy C. Atchley, Ph.D., Chairperson

Submitted to the Graduate Faculty of
Baylor University in Partial Fulfillment of the
Requirements for the Degree
of

Master of Science

Approved by the Thesis Committee

_____

Stephen I. Dworkin, Ph.D., Chairperson

_____

Stacy C. Atchley, Ph.D.

_____

Bryan F. Shaw, Ph.D.

Accepted by the Graduate School

December 2016

_____

J. Larry Lyon, Ph.D., Dean

Page bearing signatures is kept on file in the Graduate School.

TABLE OF CONTENTS

LIST OF FIGURES

LIST OF TABLES

LIST OF EQUATIONS

ACKNOWLEDGMENTS

First and foremost, I would like to thank Dr. Ken Carlile, along with Camterra Resources, Inc. and JAG Operating, LLC for providing the data and the opportunity to work on such a great project. Without this data, or the help and guidance provided by Dr. Ken Carlile this thesis would not have been possible.

I am also grateful to the faculty, students, and staff within the Department of Geosciences at Baylor University, who were critical to the success of this thesis. Most notably, I need to thank my advisor, Dr. Steve Dworkin, who provided much needed insight and guidance along the way. I also need to thank my co-advisors, Dr. Stacy Atchley, whose teachings in carbonate reservoirs and petroleum geology were essential to this project, and Dr. Bryan Shaw. Additionally, I need to thank my colleague on this project, Daniel Parizek, who completed a complementary study and helped with this research.

My family also deserves many thanks, most importantly my parents, geologists Kevin and Claudia Byram. Without my parent's support and advice, this thesis would not have been possible. Finally, I need to thank the various people who provided additional data, guidance, insight, and advice along the way: Marvin Markley, Dan Buller of Halliburton, Jim Hankla of Baker Hughes, Paul Marchand of Camterra Resources, Inc., and Dr. Bernd Zechmann of Baylor University.

CHAPTER ONE

Introduction

Overview

The Early Cretaceous Rodessa formation is a prolific oil and gas reservoir in the Gulf Coast area. This formation has been a production target since the late 1920s with the discovery well, the Sligo Syndicate Jeter #1, being completed in Louisiana on April 1, 1928 in sec. 23, T-17-N, R-12-W at a depth of 4,272' (Roberts and Lock, 1988). The Rodessa, which is Albian-Aptian in age (107.5-109.5 mya), is laterally equivalent to the outcropping Glen Rose Formation of Texas, and both formations are part of the Trinity Group (Yurewicz et al. 1993). The Rodessa and Glen Rose Formations were deposited in shallow marine environments on a broad carbonate platform.

The Rodessa Formation is subdivided into a number of different members, including but not limited to, the Bacon, Hill, Gloyd, Dees, and Young Members. Although several studies have been conducted on the Rodessa, very little is known about this formation, especially in NW Louisiana. Furthermore, studies of specific members of the Rodessa are even less common. The informally named DeBroeck Member is one unit that has been ignored, likely because of its low resistivity response to electric logging tools. Because of this, the DeBroeck Member has been classified by many as a "wet" zone in NW Louisiana and passed up in terms of both exploration and study. Recently however, a highly productive well has been completed in this zone, pointing to the fact that even though the resistivity log shows the zone as "wet", the member may be a future

exploration target. Because of this, the DeBroeck Member is appropriate for further investigation of its depositional setting, porosity and permeability evolution, and cementation history in order to determine if it is indeed a candidate for future exploration.

Objectives

The objective of this study is to investigate factors affecting reservoir quality as well as to assess wireline log responses exhibited by the DeBroeck Member of the Rodessa. The specific study goals are as follows:

1) Determine environments of deposition for each facies

2) Investigate the types, occurrence, and evolution of porosity and permeability

3) Investigate the diagenetic history of the DeBroeck Member with particular emphasis on the types of cement and the timing of cementation

4) Identify the factor(s) causing the abnormally low resistivity readings within the DeBroeck Member of the Rodessa Formation

Daniel Parizek, a contemporary and collaborating M.S. student within the Baylor University Department of Geosciences, is completing a complementary study to determine the distribution of the reservoir within the study area, and determine those area(s) that are most prospective for future development drilling.

Study Area

The study area lies within both West Elm Grove Field and Caspiana Field on the border of the Sabine Uplift and the North Louisiana Salt Basin in NW Louisiana. The two main wells this study focuses on are the Camterra Resources B. DeBroeck 33-#1 located in West Elm Grove Field in sec. 33, T-16-N, R-13-W and the Jag Operating McFerren

36-#2 located in Caspiana Field in sec. 36, T-16-N, R-14-W. The location of the study area and the two wells with core are shown in Figure 1.1.

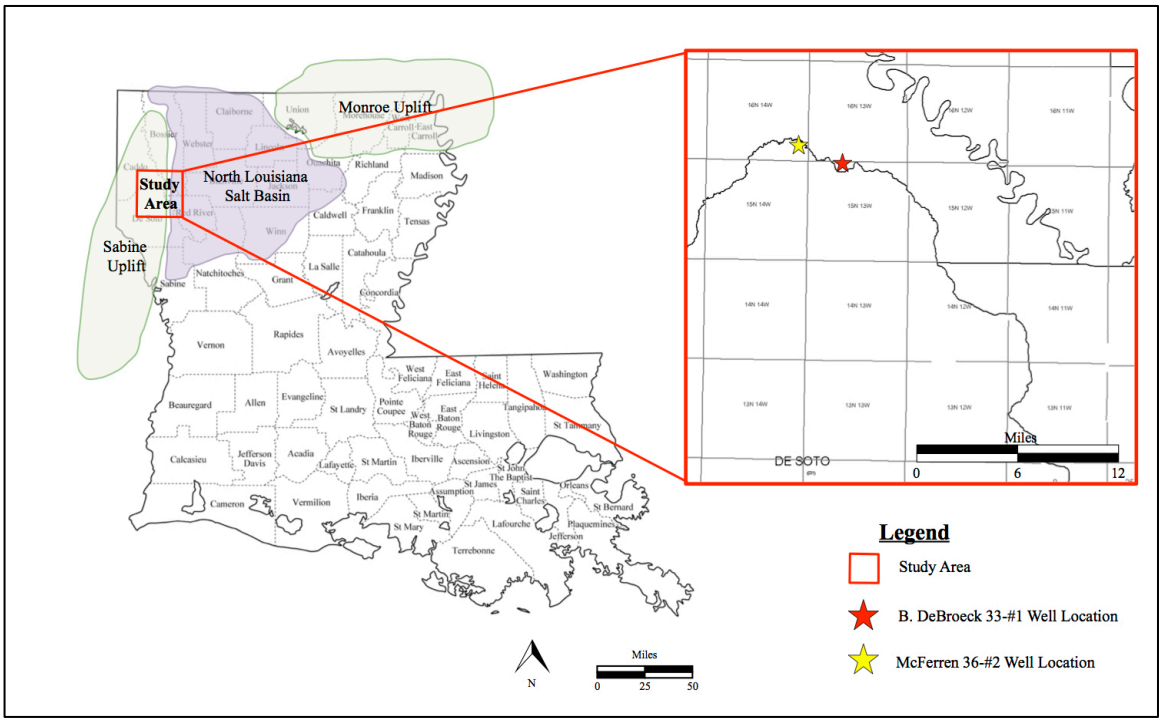

Figure 1.1. Regional study area map showing the study area and locations of the cored wells used in the study (modified from Li 2006).

Regional Geology

The dominant geologic features in the study area are the Sabine Uplift, the North Louisiana Salt Basin, and the Monroe Uplift, which are shown in Figure 1.2. The formation of these geologic features is directly linked to the tectonic history of the Gulf of Mexico, which has been dominated by extensional rift tectonics and wrench faulting (Mancini et al. 2005). Li (2006) has summarized the geologic history of the North Louisiana Salt Basin in terms of three phases: 1) a phase of crustal extension and

thinning, 2) a phase of rifting and seafloor spreading, and 3) a phase of thermal subsidence.

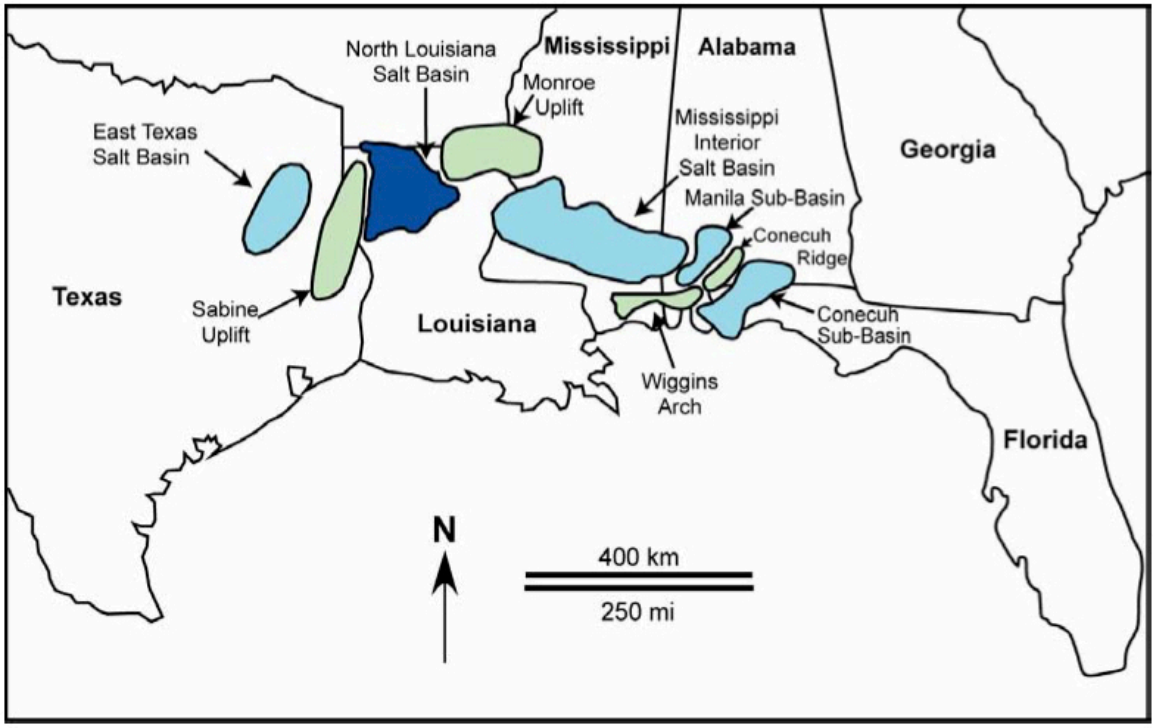

Figure 1.2. Jurassic basins and uplifts within the Gulf Coast region (from Li, 2006).

Tectonic Evolution

During the end of the Proterozoic to the early Paleozoic the northern margin of the Gulf of Mexico Basin was characterized as a passive margin (Lowrie et al. 1993). This North American passive margin was disturbed in the Late Paleozoic by the collision of the South American Plate in an event known as the Ouachita Orogeny (Jackson and Laubach 1988; Lowrie et al. 1993). South of the Ouachita Orogenic Belt lies the Sabine Terrane, which is comprised of thick continental crust resulting from a portion of the South American Plate or an independent microcontinent accreting to the North American

Plate during the Ouachita Orogeny (Lowrie et al. 1993). During the Pennsylvanian Desmoinesian stage (330-310 mya), plate collision ended and the collision tectonics and magmatism ceased (Lowrie et al. 1993). This was followed by a period of widespread uplift and erosion that was likely caused by a rising mantle plume and rifting in the Lower to Middle Triassic (Lowrie et al. 1993). Localized rifting occurred in the Late Triassic to the south of the Ouachita Orogenic Belt, resulting in the formation of rift grabens up to 60 miles wide throughout the area (Lowrie et al. 1993). Through the processes of rifting and faulting, the crust of the Gulf Coast region became attenuated during the early Jurassic (Lowrie et al. 1993). During the Middle Jurassic a second phase of NW-SE trending crustal extension and thinning occurred, shown in Figure 1.3, and resulted in a series of alternating basement horsts and grabens within the Gulf Coast region (Lowrie et al. 1993). These alternating horsts and grabens formed several major basin and uplift features including the North Louisiana Salt Basin, the East Texas Basin, and the Sabine and Monroe uplifts (Li 2006). The Middle Jurassic also saw the beginning of seawater incursion from the Pacific Basin and the beginning of uplift in the Sabine Uplift region (Li 2006; Lowrie et al. 1993). In the Upper Jurassic (155-130 mya), a phase of seafloor spreading and oceanic crust formation began in the central Gulf of Mexico (Li 2006). During the Oxfordian Stage, seafloor spreading coupled with widespread and prolonged marine transgression led to the initial formation of the ancestral Gulf of Mexico (Li 2006). Additionally, regional subsidence of the North Louisiana Salt Basin area began during the Upper Jurassic (Lowrie et al. 1993). The North Louisiana Salt Basin provided sediment accommodation with a maximum sediment thickness of 27,000 ft. (Lowrie et al. 1993). The Monroe and Sabine uplifts flank the North Louisiana Salt

Basin to the east and west respectively, and the Sabine Uplift separates it from the East Texas Basin (Lowrie et al. 1993; Li 2006).

By the Late Jurassic, the rifted continental crust had cooled. This strengthened the lithosphere and caused regional subsidence that was amplified by sediment loading (Nunn 1990). During the Late Jurassic, the deep Gulf of Mexico also experienced sea floor spreading that added to subsidence as the crust cooled (Jackson and Laubach 1988; Lowrie et al. 1993; Nunn 1990; Li 2006). Although the North Louisiana Salt Basin was an actively subsiding depocenter throughout the Mesozoic and into the Cenozoic, subsidence and sediment accumulation rates were highest in the Jurassic (Li 2006; Mancini et al. 2006). This high rate of subsidence in the Jurassic led to widespread

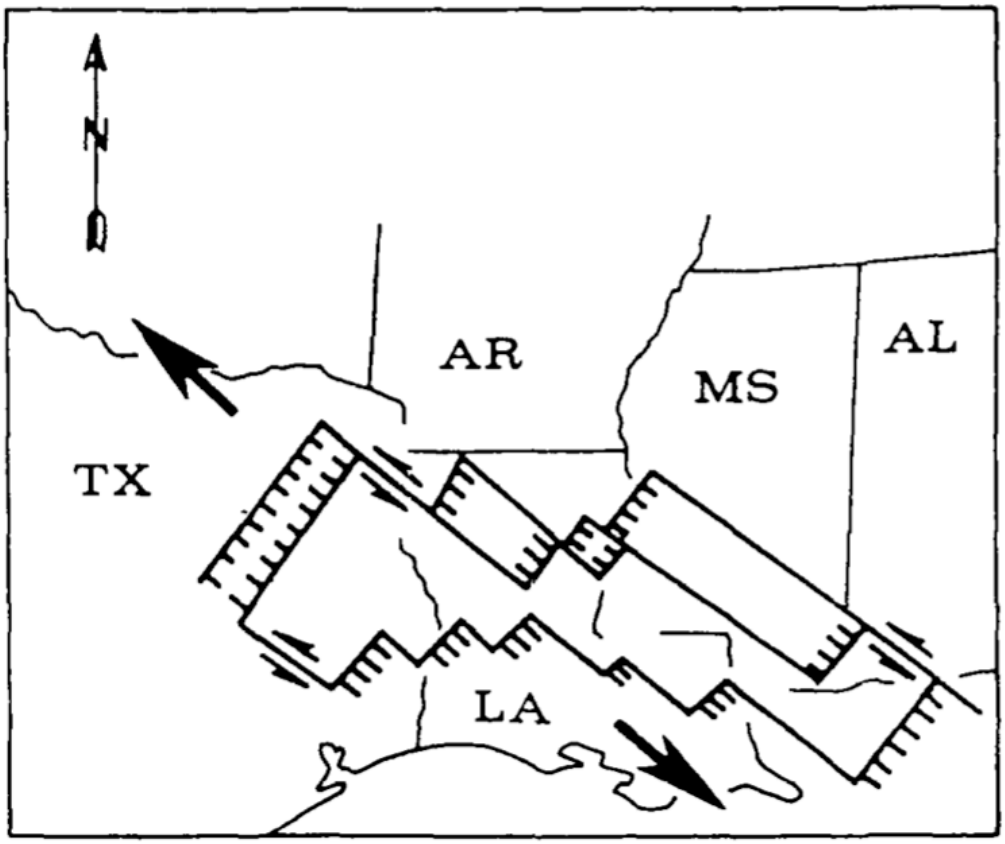

Figure 1.3. Map showing the northwest trending extension in the Gulf Coast region (from Lowrie et al. 1993).

marine transgression and sediment infilling of basement lows, which aided the development of an Early Cretaceous carbonate platform (Li 2006; Lowrie et al. 1993). The platform margin followed the tectonic hinge zone, which resulted in both thin and thick transitional crust (Li 2006; Mancini et al. 2006). Within the platform, salt deformation continued throughout the Lower Cretaceous and formed localized topographic highs in the North Louisiana Salt Basin. These paleobathymetric highs served as the nucleation site for patch reefs and carbonate shoals (Yurewicz et al. 1993).

The tectonics of the Lower Cretaceous were dominated by the cessation of seafloor spreading in the Gulf of Mexico and by the continued tectonic subsidence of the North Louisiana Salt Basin (Lowrie et al. 1993). The Middle Cretaceous saw the formation of a widespread unconformity in the Gulf of Mexico Basin, the formal initiation of the Sabine Uplift, and a dramatic slowing of the subsidence within the North Louisiana Salt Basin (Lowrie et al. 1993). By the Late Cretaceous, the Sabine Uplift was structurally lower than the North Louisiana Salt Basin, but remained higher than the East Texas Basin. A second period of reactivation of the Sabine Uplift occurred in the Eocene, coincident with the Laramide Orogeny, and resulted in 650 ft. of uplift (Seni and Jackson 1983).

Depositional History

The sedimentary record of the Lower Cretaceous in the Gulf of Mexico (including the Rodessa Formation) is characterized by alternating marine transgressions and regressions (Figure 1.4). Figure 1.5 presents a stratigraphic column for the region with the Rodessa Limestone Members highlighted. Yurewicz et al. (1993) grouped the Rodessa Formation as well as the overlying Ferry Lake Anhydrite and the underlying

Bexar Shale as one sequence stratigraphic interval termed the "Upper Aptian-Lower Albian Rodessa and Ferry Lake Sequence". The lowermost formation of this sequence, the Bexar Shale, is a widespread marine mudrock that abruptly overlies an Aptian-aged limestone formation termed the James Lime (Yurewicz et al. 1993). The Bexar is interpreted as the dominant portion of the transgressive systems tract that makes up this sequence and is comprised mainly of siliciclastic and calcareous shales along with lesser micritic limestones (Yurewicz et al. 1993). Yurewicz et al. (1993) interprets the Rodessa Formation as the latest transgressive or earliest highstand depositional portion of this sequence.

The Rodessa is comprised almost entirely of carbonates, but is known to have minor siliciclastic members as well (Triyana 2003). For example, the Hill Sand is a member of the Rodessa Formation that is comprised of fine-grained quartz sandstone (Frizzell 1987). A number of other members of this formation are recognized as sandstone as well, including portions of the Jeter Member and the Carlisle Member. These sandstones occur more frequently in parts of Southern Arkansas and Eastern Texas. However in this study area the Rodessa is almost always a limetone, especially the DeBroeck Member, which this study focuses on. The Rodessa Formation was deposited on a broad, shallow, and possibly rimmed marine carbonate platform (Yurewicz et al. 1993). Yurewicz et al. (1993) goes on to describe that this Lower Cretaceous carbonate platform was likely characterized by four different environmental zones: a broad, restricted, shallow marine platform interior or lagoon; a narrow, well-circulated, shallow marine outer platform; a well-defined platform margin; and a foreslope that dipped gradually into the central Gulf of Mexico.

The uppermost formation of the sequence is the Ferry Lake Anhydrite, which is comprised of widespread platform evaporites with lesser amounts of interbedded carbonates (Yurewicz et al. 1993; Forgotson Jr 1963). The Ferry Lake Formation is interpreted as a highstand deposit, and the platform margin that was present during its deposition must have been a continuous restricting complex that acted as a sill/barrier in order for such extensive platform evaporites to form (Yurewicz et al. 1993; Forgotson Jr, 1963).

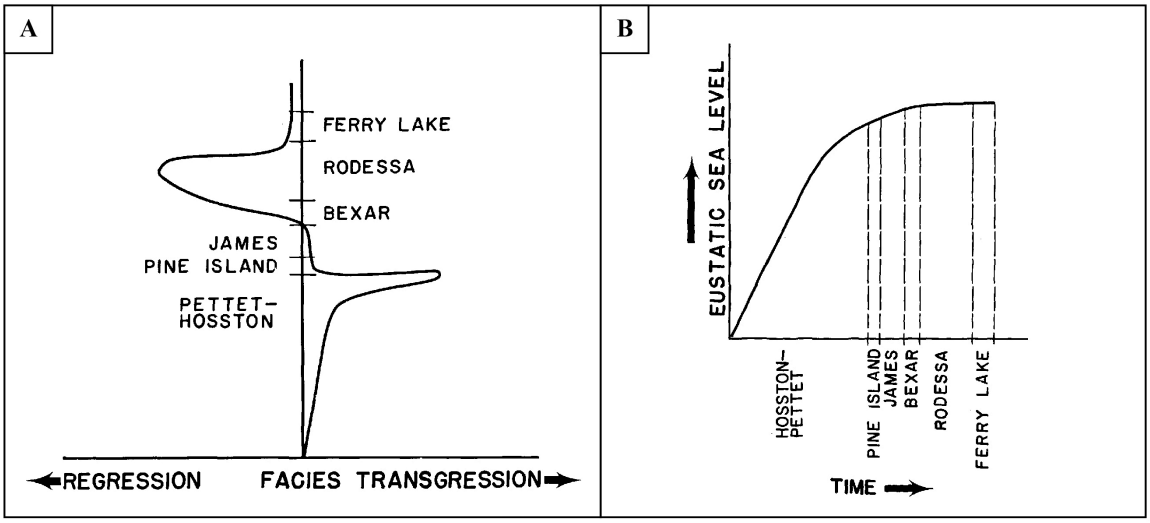

Figure 1.4. Lower Cretaceous sea level history within the Gulf Coast region. A) History of transgression and regression B) History of eustatic sea level (from Bushaw 1968).

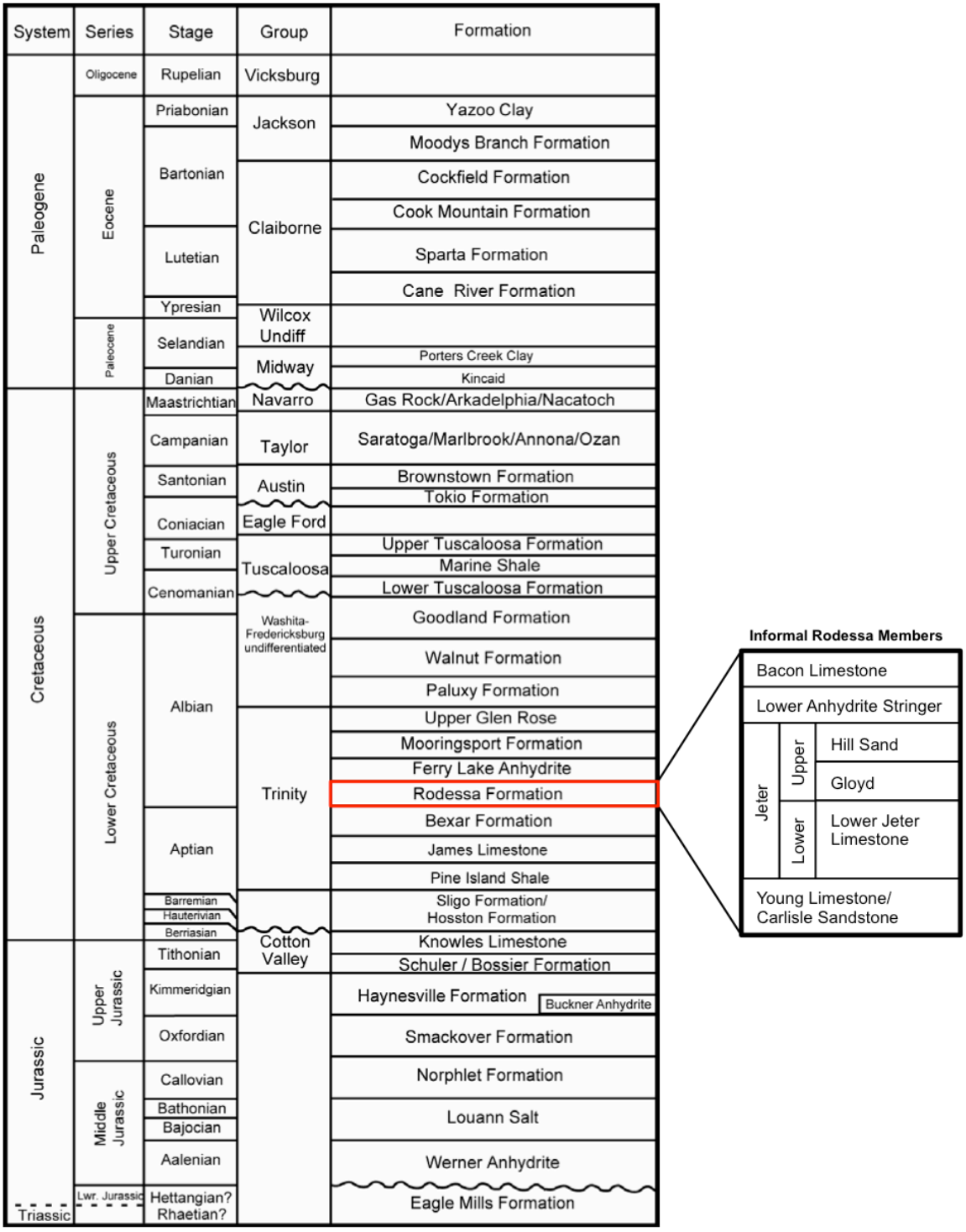

Figure 1.5. Lithostratigraphic correlation chart for the North Louisiana Salt Basin highlighting the Rodessa Limestone and its informal members (modified from Li 2006).

CHAPTER TWO

Field Studies

A few studies conducted on the Rodessa provide some background into the lithologic character, lateral extent, and the field/production history. The nearest location of a Rodessa study to the present study area is the Sligo Field, which is 10 miles away (Roberts and Lock, 1988).

Van Field, Van Zandt County, Texas

Triyana (2004) documents a 225 ft. conventional core that captured almost the entire thickness of the Rodessa in the Van Field area. After describing the core, Triyana (2004) notes seven distinct lithofacies including: 1) Sandstone lithofacies, 2) Peloid-lithoclast packstone to grainstone lithofacies, 3) Carbonaceous sandstone lithofacies, 4) Mollusk packstone lithofacies, 5) Oolitic packstone to grainstone lithofacies, 6) Skeletal mudstone to packstone lithofacies, 7) Oolitic mudstone to grainstone lithofacies.

After describing the core and noting unique lithofacies, Triyana went on to divide the Rodessa into two separate zones: the lower Carlisle Member (facies 1 and 2) and the upper limestones (facies 3 through 7). In terms of environments of deposition, lithofacies 1 is interpreted as high-energy tidal channel deposits and lithofacies 2 as distal deltaic or lagoonal deposits. Facies 3, which overlies the Carlisle Member and is the beginning of the upper limestone zone, is interpreted as a tidal flat deposit. The remaining components of the upper limestone zone, Facies 4-7, are all interpreted as lagoonal to lower intertidal.

Triyana (2004) states that the primary reservoir rock within the Rodessa Formation in the Van Field area is the Carlisle Sandstone zone. This zone is an oil-bearing medium to coarse-grained sandstone with an avg. porosity of 8-11% and permeability ranging from 46 md to 846 mD.

Running Duke Field, Houston County, Texas

Keith and Pittman (1983) studied the Rodessa in Running Duke Field using core from five different wells to describe the lithologic character of the Rodessa and to compare the descriptions to log response and production values. Six distinct lithofacies are noted and include: 1) Coral-algal-rudist packstone, 2) Rudistid packstone, 3) Coral-peloid packstone, 4) Peloid-intraclast packstone, 5) Ooid-skeletal grainstone, 6) Mollusk-foram wackestone to packstone.

According to the study, the individual lithofacies represent environments associated with biohermal buildups on the broad carbonate platform. These buildups were initiated with the coral-algal-rudist packstone facies followed by the rudist packstone, which overlies the initial buildup. The remaining packstone facies were deposited over the rudist packstone, ending with the ooid skeletal grainstone. In terms of environments of deposition, the coral-algal-rudist packstone facies is interpreted as a patch reef/carbonate buildup, whereas the remaining packstone facies are interpreted as back reef deposits. The ooid-skeletal grainstone facies is interpreted as a carbonate shoal environment.

The Running Duke Field is a small domal structure that historically produces natural gas from the ooid-skeletal grainstone facies. The porosity in this facies was determined to range from 7% to 14%, with the porosity being bimodal in nature. The

water saturation in this zone can be 55% or higher, but due to the intragranular microporosity, a large portion of the water is bound by capillary pressure and is immovable. Because of this, the ooid-skeletal facies is the primary reservoir rock for the Rodessa in this field.

An additional study on the Running Duke Field was conducted by Asquith and Jacka (1992). In this study the reservoir rocks within the Rodessa Formation consist of ooid grainstones, ooid skeletal grainstones, and skeletal grainstones. Asquith and Jacka (1992) also recognized bimodal porosity, however, they focused on the reservoir potential enhanced by early fresh water diagenesis, which created the bimodal porosity system. This porosity system consists of both intragranular microporosity and intergranular megaporosity, with the microporosity being the cause of the high water saturation in the reservoir. Using a combination of mercury injection and petrographic analysis, the authors were able to correct the water saturation values from 69.4% to an effective water saturation value of 34.9%. This large correction in effective reservoir water saturation demonstrates the true productive potential of the reservoir in this field.

Sligo Field, Bossier Parish, Louisiana

Roberts and Lock (1988) used core from three wells at the Sligo field (ranging in thickness from 51 to 105 ft. long) to identify eight distinct lithofacies including: 1) Miliolid Packstone, 2) Monopleurid Framestone/Packstone, 3) Silty Oyster/Serpulid Packstone, 4) Molluscan Wackestone, 5) Anhydritic Grainstone, 6) Carbonate Mudstone, 7) Shale, 8) Sandstone.

In terms of environments of deposition, the authors note that all the lithofacies are consistent with a restricted platform setting. They also note that the sands were most

likely deposited as tidal flat sands, whereas the shales were most likely deposited in a subtidal setting. The monopleurid and miliolid forams indicate restricted, lagoonal conditions of varying salinities, whereas ooliths, that are minor in abundance, suggest higher energy conditions on shoals within the lagoon.

Sligo Field in NW Louisiana is a domal structure elongated in a north-south orientation that was discovered in the 1920s and has produced abundant amounts of hydrocarbons in the form of oil, natural gas, and condensate. The informal Jeter Member of the Rodessa Formation is productive in the field and contains sandstones and limestones with porosity as high as 20%. The Rodessa produces from sandstones in the western portion of the field, but core analysis shows that sandstones in the study area have low permeability due to cementation.

North Shongaloo-Red Rock Field, Webster Parish, Louisiana

Frizzell (1987) analyzed the Hill Sand Member of the Rodessa Formation in the North Shongaloo-Red Rock Field, which is within the North Louisiana Salt Basin. Frizzell notes that the Hill Sand produces oil and gas, and is composed of sandstone and shale interpreted as meandering fluvial deposits. The Hill Sand reservoir has an average porosity of 26% and an average permeability of 625 md, and ~30% water saturation. Hydrocarbons are entrapped in association with closure on a westerly plunging anticlinal nose (Frizzel, 1987).

Bethany Longstreet Field, Desoto Parish, Louisiana

Foll (1980) focused on the Bethany Longstreet Field, specifically the informally named Young Member of the Rodessa Formation. Foll (1980) subdivided the Young

Member into two units: a lower oolitic limestone and an upper fossiliferous limestone. The author noted that the reservoir produces both oil and gas, has an average porosity of 13%, an average permeability of 30 md, and water saturation ~60%. The abnormally high water saturation can likely be explained by bound water within microporosity, similar to the Running Duke Field analyses by Keith and Pittman (1983) and Asquith and Jacka (1992).

Elm Grove Field, Caddo and Bossier Parishes, Louisiana

Hudsmith (1987) studied the Upper and Lower Members of the Rodessa Formation at Elm Grove Field. Hudsmith recorded gas production from these intervals and noted that the Lower Jeter is a fossiliferous pelletal limestone and the Upper Jeter is an oolitic, dolomitic limestone. Hudsmith determined hydrocarbons are trapped within anticlinal closure adjacent to a fault.

CHAPTER THREE

Methodology

Data

Data for the study was provided by both Camterra Resources, Inc. and JAG Operating, LLC in the form of:

1) Base maps and other supporting maps

2) Digital copies and hard copies of many well logs in the study area

3) Access to IHS Petra Mapping Software

4) Two 30 ft. conventional cores

5) Thin sections and Core Lab core analyses from the cores

This study was completed at Baylor University using the facilities of the Department of Geosciences and the Center for Microscopy and Imaging.

Core Description

This study is based in part on two 30' conventional cores from two wells. The Camterra Resources B. DeBroeck 33-#1 well is located in West Elm Grove Field in sec. 33, T-16-N, R-13-W and was completed in the DeBroeck Zone in February 2015. This well is currently producing from the DeBroeck interval. The second core came from the Jag Operating McFerren 36-#2 well located in Caspiana Field in sec. 36, T-16-N, R-14-W. This well was completed in October 2015 and is currently producing from the DeBroeck Interval. These two wells are approximately 2.9 miles apart.

Standardized core description forms were used to record core attributes including interval thickness, lithology, carbonate texture, lithofacies, sedimentary and biogenic structures, grains/allochems, pore type, and stylolite frequency and orientation. To correctly classify the carbonate rocks, Embry and Klovan's (1971) expanded and modified version of the Dunham (1962) carbonate classification system was used (Figure 3.1). Porosity was characterized using the classification of Choquette and Pray, shown in Figure 3.2 (1970). Carbonate grains were identified with the aid of the 1978 AAPG guide to carbonate rock constituents (Scholle 1978).

<table>
<tr><td colspan="6">Allochthonous limestone original components not organically bound during deposition</td><td colspan="3">Allochthonous limestone original components organically bound during deposition</td></tr>
<tr><td colspan="4">Less than 10% >2mm components</td><td colspan="2">Greater than 10% >2mm components</td><td colspan="3">Boundstone</td></tr>
<tr><td colspan="3">Contains lime mud (<0.02 mm)</td><td>No lime mud</td><td rowspan="3">Matrix supported</td><td rowspan="3">>2mm component supported</td><td rowspan="3">By organisms which act as barriers</td><td rowspan="3">By organisms which encrust and bind</td><td rowspan="3">By organisms which build a rigid framework</td></tr>
<tr><td colspan="2">Mud supported</td><td colspan="2" rowspan="2">Grain supported</td></tr>
<tr><td>Less than 10% grains (>0.02 mm to <2mm)</td><td>Greater than 10% grains</td></tr>
<tr><td>Mudstone</td><td>Wackestone</td><td>Packstone</td><td>Grainstone</td><td>Floatstone</td><td>Rudstone</td><td>Bafflestone</td><td>Bindstone</td><td>Framestone</td></tr>
</table>

Figure 3.1. Modified version of Dunham's 1962 carbonate classification scheme (Embry III and Klovan, 1971).

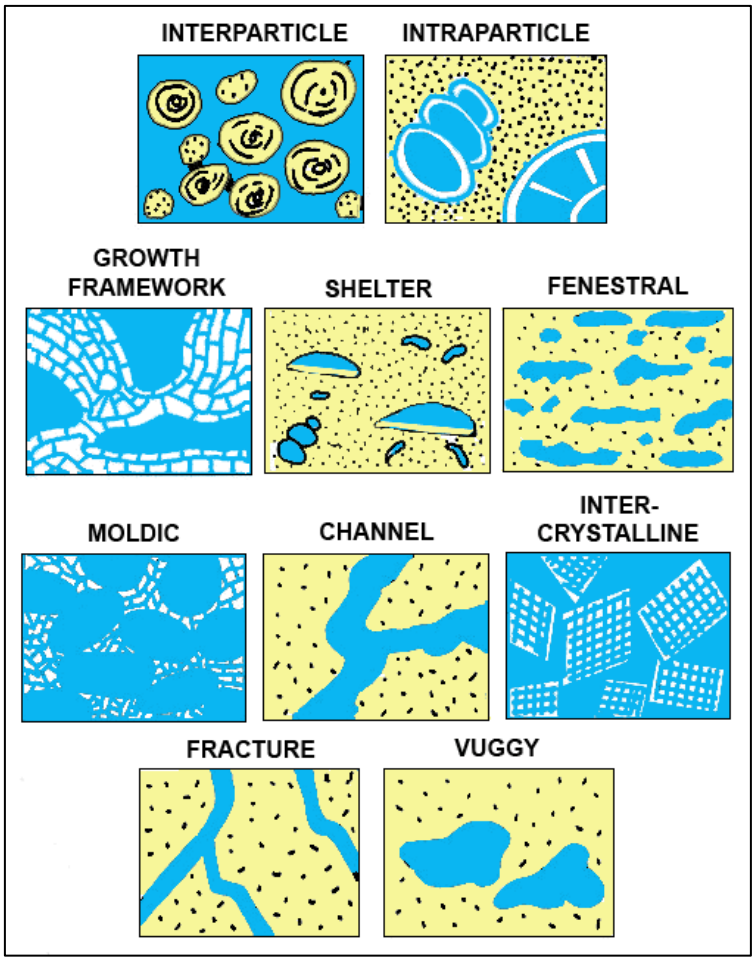

Figure 3.2. Porosity type characterization by Choquette and Pray 1970.

Core Porosity and Permeability Analysis

One-inch by one half-inch plugs were drilled with nitrogen gas as a bit lubricant. Porosity and permeability measurements were made on these plugs by Core Lab. Porosity was calculated using the Summation of Fluids technique (Hensel 1982). For this analysis, a portion of the sample is place into a calibrated mercury pump to measure the bulk volume of the sample via mercury displacement. The gas bulk is measured by injecting mercury into the sample at 750 psi. The sample is placed into a retort cup with a calibrated receiving tube. The samples are retorted to 400 °F to remove pore water and

determine the water bulk. The oven temperature is increased to 1200 °F and the oil is retorted from the sample to determine the oil bulk. The sum of the gas bulk, water bulk, and oil bulk is equal to the porosity. All mercury is recovered. Permeability to air was measured on each sample using unsteady-state method with a Profile Permeameter.

In addition to this standard porosity and permeability analysis, high-pressure mercury injection (HPMI) porosity analysis was conducted on one core plug. This type of analysis injects mercury into the core plug at pressures up to 55,000 psi to ensure all pore space is saturated. HPMI analysis not only allows for an accurate measurement of total porosity, but also allows for the determination of proportions of mega-, macro-, meso-, micro-, and nanoporosity.

Photomicrograph Imaging

Standard photomicrographs were obtained using an Olympus BX51 microscope with a Leica DFC 450 camera attached and Leica Application Suite software. Thin sections and photomicrographs from the B. DeBroeck 33-#1 were also provided by Core Laboratories in Houston, using an Olympus BX41 petrographic microscope imaged by an Insight 2mp digital camera Model 18.2 with Spot Advanced 5.0.15 imaging software. Half of each thin section was stained with Alizarin Red-S in order to differentiate calcite from dolomite, and with potassium ferricyanide to distinguish ferroan carbonate varieties. The thin sections were analyzed using standard petrographic techniques in plane-polarized and cross-polarized light. Incident ultraviolet light was used for the epifluorescent petrographic analysis of the pore system in one sample.

Additional thin sections were obtained from both the B. DeBroeck 33-#1 core and the McFerren 36-#2 core. For the B. DeBroeck 33-#1 core, a total of nineteen additional

thin sections were made by National Petrographic Service, Inc. in Houston, TX. These thin sections were prepared in a similar manner to the Core Laboratories thin sections; however, they were not stained with either Alizarin Red-S or potassium ferricyanide, but they were polished for backscatter analysis. Nine thin sections were cut from the McFerren 36-#2 core and these were prepared in the same way as previously described.

Scanning Electron Microscope Imaging

To aid in the analysis of the two conventional cores, scanning electron microscope imaging and backscatter imaging were used to obtain detailed information concerning the fabric, texture, porosity, and composition of the reservoir rock. For SEM analysis, a total of twenty-one rock stubs were gathered from the two cores: eleven stubs from the B. DeBroeck 33-#1 core and ten stubs from the McFerren 36-#2 core. The rock stubs were collected from the core using a rock hammer and were then labeled and bagged for mounting. The stubs were mounted on round aluminum holders using silver conductive epoxy adhesive and were painted with colloidal silver paste to ensure conductivity between the rock and the aluminum holder. The stubs were then placed in a Leica EM ACE600 sputter coater and coated with ~40 nm of carbon.

The SEM imaging was conducted using a FEI Versa 3D DualBeam SEM/FIB with an EDAX accessory attached. This electron beam instrument is capable of standard SEM imaging as well as backscatter microscopy imaging. Additionally, the energy dispersive X-ray analysis (EDAX) detector provided the ability to accurately identity minerals based on their composition. For standard SEM imaging an accelerating voltage of 10.00 kV was used with a spot size of 5.0 microns, whereas the backscatter imaging was conducted using 20.00 kV accelerating voltage and a spot size of 7.0 microns. The

lower kV and smaller spot size for the standard imaging helped to reduce charging on the rock specimens, and the higher voltage and larger spot size used for the backscatter imaging allowed for images with higher resolution.

Pyrite Image Analysis

In order to determine pyrite abundance in the cores, image analysis software was used to evaluate backscatter images. The image analysis software used for this portion of the study was Cell^F with the particle analysis tool, which is an Olympus Inc. product. To conduct this analysis, backscatter images were imported into the software and gray scales for pyrite were assigned that were subsequently used by the software to determine the proportion of pyrite within the surrounding limestone. The abundance of pyrite generated from this method is considered conservative and is probably lower than the actual percentage because of corrections that had to be made due to grey scale overlap from other components in the limestone.

Isotopic Analysis

Stable isotope ratios were measured on various carbonate phases in the cores in order to evaluate paleoceonographic conditions during carbonate deposition as well as to aid in the understanding of the timing and conditions of cementation. Five samples of fossil shells, carbonate mud, and calcite spar were collected from each well using dental drill bits with a Dremel tool. Carbon and oxygen isotope ratios were determined on these powdered calcite samples by evolving CO_2 gas on a gas bench, which was then analyzed on a Thermo Finnigan Delta V Stable Isotope Mass Spectrometer.

Oxygen isotope ratios were converted to the SMOW scale using equation 1:

$$\delta^{18}O_{SMOW} = 1.03086(\delta^{18}O_{PDB}) + 30.86 \quad (1)$$

Temperatures of calcite precipitation were then calculated using equation 2:

$$\delta\ ^{18}O_{mineral} - \delta\ ^{18}O_{water} = A(10^6/T^2) + B \quad (2)$$

The equation calculates temperatures in Kelvin. The constants 'A' and 'B' for calcite were taken from Friedman and O'Neil (1977) and are: A = 2.78, B = -2.89.

In addition to the temperature of precipitation for calcite, the $\delta^{13}C$ (‰VPDB) value of the fossil shell samples and the carbonate mud samples can be used to reconstruct atmospheric $\delta^{13}CO_2$ (‰VPDB) values at the time of formation using Equation 3 (Romanek et al., 1992).

$$\delta\ ^{13}C_{CaCO3} - \delta\ ^{13}C_{CO2} = 11.98 - 0.12(\text{Temp.}) \quad (3)$$

Capillary Pressure and Formation Resistivity Factor Analysis

Two core plugs were taken from the B. DeBroeck 33-#1 in order to perform capillary pressure analysis and formation resistivity factor analysis. Both of these analyses were conducted using 156,500 ppm NaCl brine as a saturant. The capillary pressure analysis was conducted using ambient confining stress at 22.2 °C, whereas the formation factor analysis was conducted at a confining stress of 1,520 psi at 25 °C. For the capillary pressure analysis the cores were fully saturated using a gas water system. After complete saturation, the capillary pressure was determined using a high-speed centrifuge method while placing the plugs through a series of differing pressures, ranging from 0 psi to 1,000 psi. This analysis allows for the determination of the amount of capillary bound water, aka irreducible water once the data is plotted.

For the formation resistivity factor analysis, the core plugs are placed under simulated reservoir conditions and their electrical properties are tested. The plugs are placed in an insulating holder with electrodes on each end and the electrical properties of the rock are measured. This allows for the determination of accurate 'm' and 'n' values that are used in the equation proposed by Archie (1942).

Saltwater/Formation Water Saturation Analysis

In order to estimate the percentage of pore space saturated by formation water, Archie's (1942) Equation, was used (Eq. 4).

$$S_w = ((a/\Phi^m)*(R_w/R_t))^{1/n} \quad (4)$$

In this equation, 'S_w' is the saltwater saturation in percent, 'a' is the correlation coefficient, 'Φ' is the porosity in percent, 'm' is the cementation factor, 'n' is the saturation exponent, R_w is the formation water resistivity in ohms, and R_t is the formation resistivity. All resistivity measurements are in ohms. This study uses this equation, along with the 'm' and 'n' values determined from the formation factor analysis, to try and estimate the amount of the reservoir saturated by formation water.

CHAPTER FOUR

Results and Discussion

Facies Identification, Description, and Environmental Interpretation

Upon detailed description, a total of fourteen lithofacies were identified. Photomicrograph images were taken of each facies excluding Facies 11 and 13, and SEM images were taken of each facies excluding Facies 2, 10, and 13. The photomicrograph images were used to gain a general understanding of the rock texture, rock composition, porosity distribution and type, major and minor allochems, amount and types of cement, and amount of micritization. The images obtained show that, 1) there is a wide range of allochem type, and that many of the allochems have micritized rims, 2) micritization is a common feature in all facies in both cores, 3) porosity is present as interparticle, intraparticle, and moldic, 4) the most abundant cement in all of the facies is calcite; however, anhydrite, dolomite, and pyrite cements are widely dispersed but occur in small amounts. Figures 4.1 and 4.2 show facies photographs from the core.

The SEM images were used to gain an understanding of the fine scale aspects of the rock, as well as to determine an estimate of the amount of pyrite within the rock. The images obtained indicate that much of the rock consists of microcrystalline calcite and that portions of the rock contain significant proportions of pyrite.

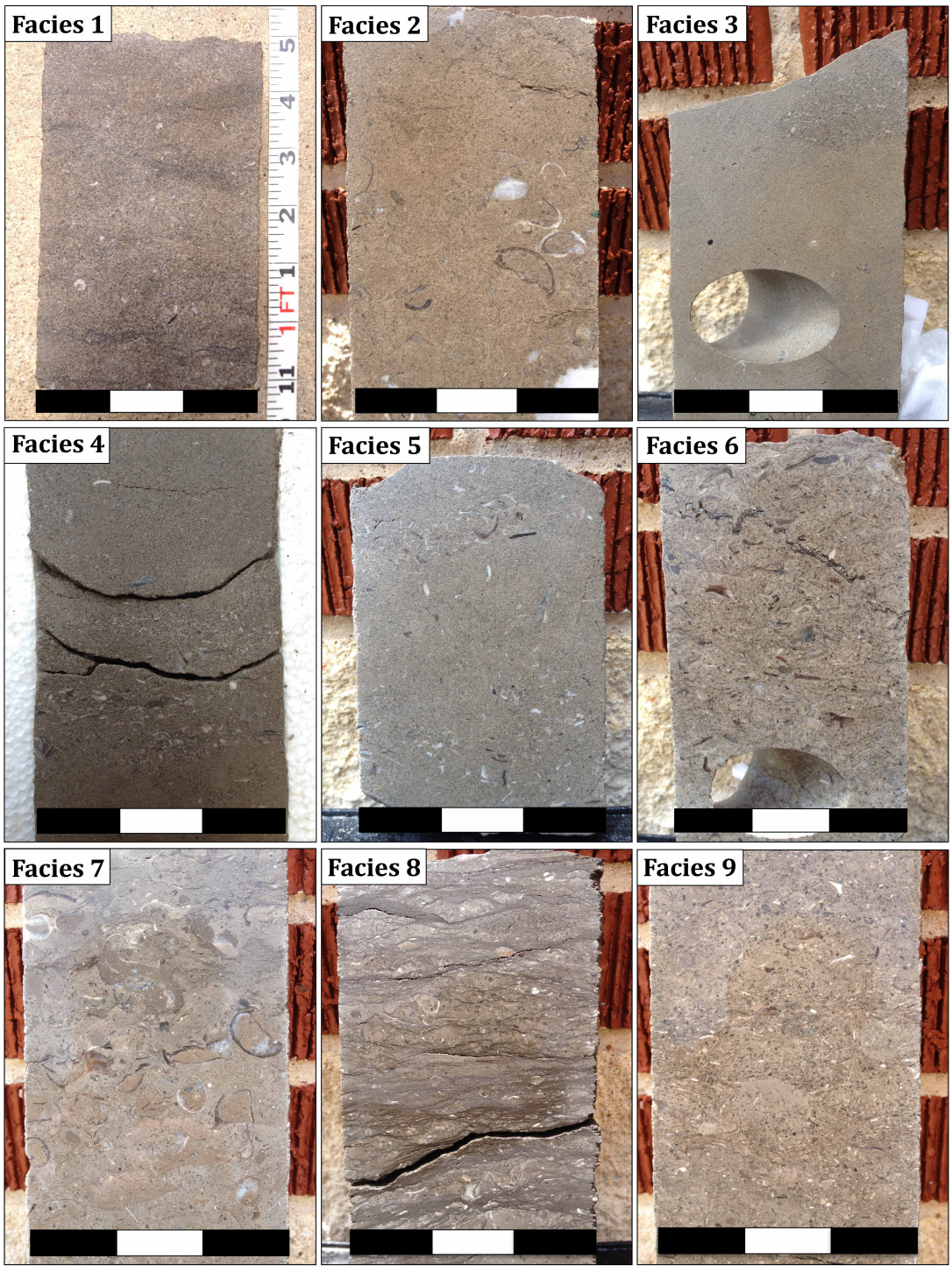

Figure 4.1. Core photographs for facies 1 through 9 (all scale bars are 3 inches). Facies 1) Core photograph from the B. DeBroeck 33-#1 well at 5,118'. Facies 2) Core photograph from the B. DeBroeck 33-#1 well at 5,123'. Facies 3) Core photograph from the B. DeBroeck 33-#1 well at 5,114'. Facies 4) Core photograph from the B. DeBroeck 33-#1 well at 5,111.5'. Facies 5) Core photograph from the B. DeBroeck 33-#1 well at 5,109'. Facies 6) Core photograph from the B. DeBroeck 33-#1 well at 5,106'. Facies 7) Core photograph from the B. DeBroeck 33-#1 well at 5,102'. Facies 8) Core photograph from the B. DeBroeck 33-#1 well at 5,101.5'. Facies 9) Core photograph from the B. DeBroeck 33-#1 well at 5,100'.

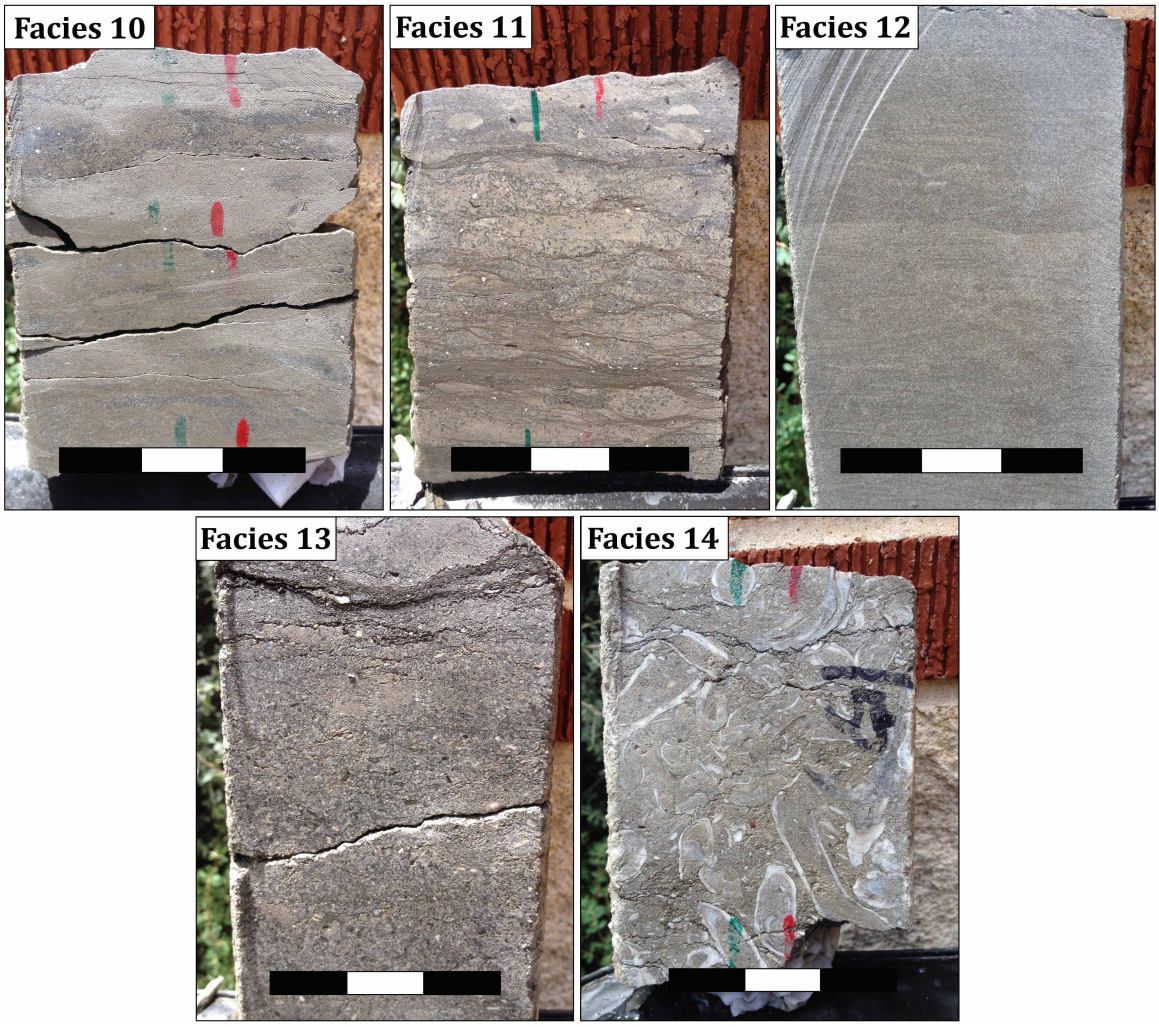

Figure 4.2. Core photographs for facies 10 through14 (all scale bars are 3 inches). Facies 10) Core photograph from the McFerren 36-#2 well at 5,068'. Facies 11) Core photograph from the McFerren 36-#2 well at 5,062'. Facies 12) Core photograph from the McFerren 36-#2 well at 5,059'. Facies 13) Core photograph from the McFerren 36-#2 well at 5,058'. Facies 14) Core photograph from the McFerren 36-#2 well at 5,056'.

1. Burrowed Bioclastic Packstone-Grainstone

Description. Facies 1 is a packstone to grainstone and contains a diverse assemblage of skeletal and non-skeletal carbonate grains (Fig. 4.1 and 4.3). Major grains include rudist fragments, peloids, echinoderms, and intraclasts (Fig. 4.3. A, B, and C) while minor amounts of gastropods (Fig. 4.3.C), radiolaria, foraminifera, bryozoa, coral,

coated grains, grapestones, ostracods, charophytes, and brachiopod fragments (Fig. 4.3.C) are also present. This facies contains *Thalassinoides* burrows (Fig. 4.1), and is cemented by calcite and sparsely nodular anhydrite. Coarse calcite cement (spar) fills allochem molds and interparticle pores (Fig. 4.3. A, B, C and D). Carbonate mud between the allochems is composed of euhedral microspar (Fig. 4.3. D and F) indicating recrystallization of the original micritic matrix. Pyrite cement is also dispersed throughout Facies 1 (Fig. 4.3.E). Horizontal serrate and horsetail stylolites are also present in this facies with an abundance of around five stylolites per foot (Fig. 4.1).

Facies 1 is 9' thick in the DeBroeck well and contains the highest porosity and permeability, which are 21.3% and 49.6 mD, respectively. However, porosity and permeability within this facies have been reduced by the precipitation of calcite and anhydrite cement. Porosity types include interparticle, intraparticle, and moldic pores (Fig. 4.3. A, B, and C). Abundant intergranular porosity is shown in Figure 4.3.A, while moldic porosity can be seen within dissolved allochems in Figure 4.3.B and in the dissolved portions of the gastropod shell in Figure 4.3.C. SEM images reveal microporosity as the black areas between the microcrystalline calcite (Fig. 4.3. D and F). Facies 1 contains pyrite that is shown in Figure 4.3.E where a framboid has been plucked out of the limestone.

Environmental interpretation. The presence of miliolid and orbitolinid foraminifers in this facies along with *Thalassinoides* burrows suggests a shallow, open marine environment that is below wave base with water temperatures between 15°C and 35°C, and a normal salinity (Ross 1979; Yanin and Barboshkin 2011). Orbitolinid

foraminifers are commonly associated with biohermal deposits and often found in fore-reef deposits as well as reef limestones (Douglass 1960).

2. Burrowed Brachiopod Packstone

Description. Facies 2 is a packstone that contains a diverse assemblage of skeletal and non-skeletal carbonate grains (Fig. 4.1 and 4.4). Major grains include brachiopod fragments, peloids, and intraclasts (Fig. 4.4) and lesser amounts of echinoderms, coated grains, foraminifera, and radiolaria. This facies contains *Thalassinoides* burrows (Fig. 4.3). Micritization of allochem grain margins is common (Fig. 4.4. B, C, and D). Cements include sparry calcite, anhydrite, and dolomite (Fig. 4.4. C, D, and E). Calcite spar surrounded by anhydrite (Fig. 4.4. D and E) suggests that anhydrite precipitated after calcite cement. Coarse calcite, dolomite, and anhydrite cement (spar) fills dissolved allochem molds and intergranular areas (Fig. 4.4).

Facies 2 is 9.7" thick in the DeBroeck well. The highest porosity and permeability values are 11.9% and 3.08 mD. Porosity and permeability have been reduced in the facies by the precipitation of calcite, dolomite, and anhydrite cements (Fig. 4.4. A, C, D, E). Porosity in Facies 2 is classified as interparticle, intraparticle, and moldic. Figure 4.4.A and B show the poorly sorted nature of allochems in Facies 2 as well as the abundance of intergranular and moldic porosity. Figure 4.4.C shows a good example of moldic porosity within a micritized and dissolved allochem. Abundant amounts of carbonate mud are also present in this facies as seen in Figures 4.4.C and E.

Environmental interpretation. The presence of miliolid foraminifers and *Thalassinoides* burrows in this facies suggests shallow, normal, open marine conditions with water temperatures above 20°C (Ross 1979; Yanin and Barboshkin 2011). The presence of coated grains suggests an environment that is above fair-weather wave base and waters that are oversaturated with respect to CaCO3; however, their rare occurrence suggests they were allochthonous.

3. Burrowed Peloidal Packstone

Description. Facies 3 is a fine-grained packstone that contains a diverse assemblage of skeletal and non-skeletal carbonate grains (Fig. 4.1 and 4.5). Major grains include peloids, rudist fragments, and intraclasts (Fig. 4.5. A and B) and minor grains include whole specimens or fragments of radiolaria, echinoderms, foraminifera, and gastropod. Figure 4.5.A and B are representative of peloid dominance within this facies. This facies contains *Thalassinoides* burrows (Fig. 4.1 and 4.5.B). Micritization of grain margins is common in this facies (Fig. 4.5.A). Facies 3 is cemented by calcite and anhydrite; anhydrite is sparsely nodular (Fig. 4.5.E). The blocky and pore filling nature of the anhydrite cement is shown in Figure 4.5.E, whereas Figure 4.5.A and B show abundant calcite cement filling the intergranular pore space. Carbonate mud between the allochems is composed of euhedral to subhedral microspar (Fig. 4.5. C and D) that indicates recrystallization of the original micritic matrix. Horizontal serrate and horsetail stylolites are also present in this facies with an abundance of around three stylolites per foot (Fig. 4.1).

Facies 3 is 2’ 8” thick in the DeBroeck well. The highest porosity and permeability values are 18.5% and 25.1 mD. Porosity and permeability have been reduced in this facies by the precipitation of calcite and anhydrite cement (Fig. 4.5. A, B, and E). Porosity is classified as interparticle, intraparticle, and moldic in Facies 3 (Fig. 4.5. A and B). Microporosity is abundant within this facies and lies within/between the microcrystalline calcite grains (Fig. 4.5. C and D). Minor amounts of carbonaceous material are also preserved in the facies as shown in Figure 4.5.E.

Environmental interpretation. The presence of miliolid and orbitolinid foraminifers in this facies along with *Thalassinoides* burrows suggests a shallow, normal marine environment below fair-weather wave base with water temperatures between 15°C and 35°C (Ross 1979; Yanin and Barboshkin 2011). The orbitolinid foraminifers may suggest proximity to a biohermal deposit in a fore-reef or reef setting (Douglass 1960). This facies also appears to have a hard-ground surface, pointing to a possible *Trypanites* ichnofacies.

4. Laminated Bioclastic Grainstone

Description. Facies 4 is a grainstone that contains rudist fragments, peloids, and intraclasts, and minor amounts of radiolaria, echinoderms, foraminifera, gastropods, brachiopod fragments, and coral (Fig. 4.6. A, B, and C). This facies contains horizontal laminations (Fig. 4.1) and is cemented by calcite (Fig. 4.6. A, B, and C). Calcite cement occurs within intergranular, intragranular, and moldic pore spaces (Fig. 4.6. B and C). Micritization of allochem grain margins is common in this facies and the micritized rims of allochems and peloids is composed of subhedral crystals of microspar (Fig. 4.6.D).

Carbonate mud between the allochems is composed of euhedral microspar (Fig. 4.6.E) and indicates recrystallization of the original micritic matrix.

Facies 4 is 2" thick in the DeBroeck well, and 1.25" thick in the McFerren well. No core analysis of porosity and permeability is available; however, porosity is classified as interparticle, intraparticle, and moldic as shown in Figure 4.6. Porosity and permeability within this facies have been reduced by the precipitation of calcite spar within pore spaces. Microporosity is abundant within this facies and lies within/between the microcrystalline calcite grains (Fig. 4.6. D and E). The differences in porosity size are well represented in Figure 4.6.D, where microporosity within microspar lines a vug.

Environmental interpretation. The presence of miliolid foraminifers in this facies suggests a shallow normal marine environment with water temperatures above 20°C (Ross 1979). The presence of horizontal lamination points to a preserved storm event that lowered the wave base, thus forming the sedimentary structures.

5. Burrowed Peloidal Grainstone

Description. Facies 5 is a grainstone that contains rudist fragments, peloids, miliolids, and intraclasts and lesser amounts of brachiopod fragments, gastropods (Fig. 4.7.B), coated grains, ostracods, foraminifera (Fig. 4.7.C), and echinoderms (Fig. 4.7. A, B, and C). This facies contains *Thalassinoides* burrows (Figure 4.1), and is cemented by calcite (Fig. 4.7. A, B, and C). Calcite cement occurs within intergranular, intragranular, and moldic pore spaces (Fig. 4.7. B and C). Micritization of allochem grain margins is common in this facies (Fig. 4.7. A, B, and C) and the micritized rims of allochems and peloids are composed of subhedral crystals of microspar (Fig. 4.7. D and E). Carbonate

mud between the allochems is composed of euhedral microspar (Fig. 4.7.F) that indicates recrystallization of the original micritic matrix. Micritized allochems are surrounded by coarse, blocky calcite cement (Fig. 4.7.C), and suggests that the blocky cement precipitated after allochem micritization.

Facies 5 is 2’ 8” thick in the DeBroeck well. The highest porosity and permeability values are 17.2% and 30.9 mD. Porosity is classified as interparticle, intraparticle, and moldic in Facies 5, and the porosity and permeability have been reduced by the precipitation of calcite cement (Fig. 4.7. B and C). Microporosity is abundant within this facies and occurs within/between the microcrystalline calcite crystals (Fig. 4.7. D, E, and F). The differences in porosity size are well represented in Figure 4.7.F, where microporosity within microspar surround a large vug.

Environmental interpretation. The presence of miliolid foraminifers and *Thalassinoides* burrows in this facies indicates shallow, normal marine conditions with water temperatures above 20°C (Ross 1979; Yanin and Barboshkin 2011). The presence of coated grains suggests an environment of deposition above fair-weather wave base and waters that are oversaturated with respect to CaCO3; however, their rare occurrence suggests they were allochthonous.

6. Rudistid Rudstone

Description. Facies 6 is a rudistic rudstone that also includes a diverse assemblage of minor carbonate grains (Fig. 4.1 and 4.8). Major grains include rudist fragments and peloids, and lesser amounts of intraclasts, coated grains, echinoderms, foraminifera, bryozoa, and gastropods (Fig. 4.8. A, B, C, and D). This facies has no internal structure,

but is cemented by calcite and anhydrite (Fig. 4.8. B, C, and D). Calcite cement occurs within intergranular, intragranular, and moldic pore spaces (Fig. 4.8. C and D). Micritization of allochem grain margins is common in this facies (Fig. 4.8. B, C, and D) and the micritized rims of allochems and peloids are composed of subhedral crystals of microspar (Fig. 4.8.E). Carbonate mud between the allochems is composed of euhedral microspar (Fig. 4.8. D and E) that indicates recrystallization of the original micritic matrix.

Facies 6 is 4' thick in the DeBroeck well. The highest porosity and permeability values are 16.2% and 16.1 mD, and porosity is classified as interparticle, intraparticle, and moldic (Fig. 4.8. A, B, and C). Well preserved intragranular porosity is shown within a preserved planispiral foraminifer in Figure 4.8.D. Porosity and permeability have been reduced in Facies 6 by the precipitation of calcite and anhydrite cement (Fig. 4.8. B, C, and D). Coarse, blocky calcite fills bivalve molds and surrounds micritized allochems (Fig. 4.8.C), and suggests the blocky cement precipitated after the grains were micritized. Microporosity is abundant within this facies and occurs within/between the microcrystalline calcite crystals (Fig. 4.8. E and F).

Environmental interpretation. The presence of miliolid foraminifers in this facies suggests shallow, normal marine conditions with water temperatures above 20°C (Ross 1979). The presence of coated grains indicates an environment of deposition that is above fair-weather wave base and waters that are oversaturated with respect to CaCO3. Because this facies is a rudstone consisting mainly of large rudist fragments, it is interpreted as patch reef flank debris.

7. Burrowed Rudistid Floatstone

Description. Facies 7 is a floatstone that contains a diverse assemblage of skeletal and non-skeletal carbonate grains (Fig. 4.1 and 4.9). Major grains include rudist fragments, peloids, miliolids, radiolaria, and intraclasts, and lesser amounts of gastropods, bivalves, foraminifera, algae, echinoderms (Fig. 4.9.C), ostracods, bryozoa, and charophytes (Fig. 4.9. A, B, and C). This facies contains *Thalassinoides* burrows (Fig. 4.1), and is cemented by calcite and pyrite (Fig. 4.9. A, B, C, and F). Calcite cement occurs within intergranular, intragranular, and moldic pore spaces (Fig. 4.9. B and C). Disseminated pyrite cement is shown in Figure 4.9.F as both fine grained crystals and as large, octahedral crystals. Micritization of allochem grain margins is common (Fig. 4.9. B and C) and the micritized rims of allochems and peloids are composed of subhedral crystals of microspar (Fig. 4.9.D). Carbonate mud between the allochems is composed of euhedral microspar (Fig. 4.9.E) and indicates recrystallization of the original micritic matrix. Horizontal horsetail and serrate stylolites are also present in this facies with an abundance of around ten stylolites per foot.

Facies 7 is 3’ thick in the DeBroeck well, and 5’ 4” thick in the McFerren well. The highest porosity and permeability values are 11% and 1.36 mD, and porosity is classified as interparticle, intraparticle, and moldic. Porosity and permeability have been reduced in Facies 7 by the precipitation of calcite and pyrite cement (Fig. 4.9. B, C, and F). Microporosity is abundant within this facies and occurs within/between the microcrystalline calcite crystals (Fig. 4.9. D, E, and F).

Environmental interpretation. The high amount of carbonate mud in this facies (Figure 4.9.A) suggests a low energy environment of deposition. Therefore, this facies is interpreted as being deposited in a subtidal environment off the edge of a patch reef, with the large rudist fragments being shed off the patch reef.

8. Stylolitic Wackestone-Packstone

Description. Facies 8 is a wackestone to packstone and contains a diverse assemblage of skeletal and non-skeletal carbonate grains (Fig. 4.1 and 4.10). Major grains include rudist fragments, peloids, foraminifera, and intraclasts, and lesser amounts of crinoids, algae, foraminifera, charophytes, ostracods, radiolaria, coated grains, intraclasts, and brachiopod fragments (Fig. 4.10. A, B, and C). This facies contains numerous horizontal horsetail stylolites with an abundance of around ten stylolites per inch (Fig. 4.1 and 4.10.A). Facies 8 is cemented by calcite and pyrite (Fig. 4.10. A, B, E, and F). Calcite cement occurs within intergranular, intragranular, and moldic pore spaces (Fig. 4.10. B and C). Pyrite cement in this facies precipitated as both pyrite framboids and clusters of cubic pyrite (Fig. 4.10. E and F). Micritization of allochem grain margins is common (Fig. 4.10. B and C) and the micritized rims of allochems and peloids are composed of subhedral crystals of microspar (Fig. 4.10.D). Borings from endolithic algae can be seen in Figure 4.10.C. Carbonate mud between the allochems is composed of euhedral microspar (Fig. 4.10.E) and indicates recrystallization of the original micritic matrix.

Facies 8 is 10” thick in the DeBroeck well, and 3.5” thick in the McFerren well. The highest porosity and permeability values are 4.9% and 0.019 mD, and porosity is

classified as interparticle, intraparticle, and moldic. Porosity and permeability have been reduced in Facies 8 by the precipitation of calcite and pyrite cement (Fig. 4.10. B, C, E, and F). Microporosity is abundant within this facies and occurs within/between the microcrystalline calcite crystals (Fig. 4.10. D and E).

Environmental interpretation. The fine-grained allochems along with the lack of large rudist fragments in this facies suggest a low energy environment in deeper water than Facies 7. This facies is interpreted as deposited in a subtidal environment, farther away from the reef margin than Facies 7.

9. Burrowed Bioclastic Floatstone

Description. Facies 9 is a floatstone that contains a diverse assemblage of skeletal and non-skeletal carbonate grains (Fig. 4.1 and 4.11). Major grains include rudist fragments, peloids, miliolids, brachiopod fragments, and intraclasts, and lesser amounts of ooids, coral, algae, foraminifera, radiolaria, crinoids, echinoderms, gastropods, and ostracods (Fig. 4.11. A, B, and C). Horizontal horsetail stylolites are present in this facies with an abundance of around fifteen stylolites per foot (Fig. 4.1). This facies also contains *Thalassinoides* burrows (Fig. 4.1), and is cemented by calcite and pyrite (Fig. 4.11. A, B, C, and E). Calcite cement occurs within intergranular, intragranular, and moldic pore spaces (Fig. 4.11. A, B, and C). Pyrite cement in this facies precipitated as clusters of cubic and octahedral pyrite within the stylolites (Figure 4.11.F). Micritization of allochem grain margins is common (Fig. 4.11. B and C) and the micritized rims of allochems and peloids are composed of subhedral crystals of microspar (Fig. 4.11.D).

Carbonate mud between the allochems is composed of euhedral microspar (Fig. 4.11.E) and indicates recrystallization of the original micritic matrix.

Facies 9 is 3’ 7” thick in the DeBroeck well, and 1’ 3.3” thick in the McFerren well. The highest porosity and permeability values are 4.5% and 0.071 mD, and porosity is classified as interparticle, intraparticle, and moldic. Porosity and permeability have been reduced in Facies 9 by the precipitation of calcite and pyrite cement (Fig. 4.11. B, C, and F). Microporosity is abundant within this facies and occurs within/between the microcrystalline calcite crystals as well as within dissolution holes in calcite spar (Fig. 4.11. D and E).

Environmental interpretation. The abundant mud in this floatstone suggests a low energy environment of deposition. The miliolid foraminifers, orbitolinid foraminifers, and *Thalassinoides* burrows suggest a shallow, normal marine environment below wave base with water temperatures between 15°C and 35°C (Ross 1979; Yanin and Barboshkin 2011). The presence of coated grains suggests an environment of deposition above fair-weather wave base and waters that are oversaturated with respect to CaCO3; however, their rare occurrence suggests they were allochthonous.

10. Burrowed Laminated Mudstone-Wackestone

Description. Facies 10 is a mudstone to wackestone, is dominated by quartz grains, foraminifera, and peloids, but also includes a diverse assemblage of minor carbonate grains (Fig. 4.2 and 4.12). Minor grains include radiolaria, intraclasts, ostracods, echinoderms, brachiopod fragments, and orbitolinid foraminifera (Fig. 4.12). The intraclasts within this facies can be rather large, such as the one shown in Figure

4.12.D. Numerous horizontal horsetail stylolites are present in this facies with clusters containing as many as fifty stylolites per foot (Fig. 4.2). This facies contains *Thalassinoides* burrows (Fig. 4.2), and is cemented by calcite (Fig. 4.12. B, D, and E). Calcite cement is present as both small crystals filling pore space (Fig. 4.12.C), and as large, blocky cement completely replacing dissolved allochems (Fig. 4.12.E). Micritization of allochem grain margins is prevalent (Fig. 4.12.B), and there is an abundant amount of carbonate mud present (Fig. 4.12. D and E).

Facies 10 is 5" thick in the DeBroeck well, and 7' 9" thick in the McFerren well. The highest porosity and permeability values are 2.5% and 0.005 mD and porosity is classified as interparticle, intraparticle, and moldic (Fig. 4.12. B, C, D, and E). Porosity and permeability have been reduced in Facies 10 by the precipitation of calcite cement (Fig. 4.12. C, D, and E). Intact intragranular porosity is present within a well-preserved orbitolinid foraminifer in Figure 4.12.E.

Environmental interpretation. The muddy texture of this rock points to a low energy environment of deposition. Also, the presence of abundant silt-sized quartz grains suggests possible siliciclastic dust or deltaic/fluvial particles settling out in deep, low energy water, below fair-weather wavebase.

11. Burrowed Stylolitic Coated Grain Packstone

Description. Facies 11 is a packstone dominated by non-skeletal grains (Fig. 4.2 and 4.13). Major grains include peloids, ooids, and intraclasts, and lesser amounts of brachiopod fragments, crinoids, and rudist fragments (Fig. 4.2). Numerous horizontal horsetail stylolites are also present in this facies with an abundance of around fifty

stylolites per foot (Fig. 4.2). This facies contains *Thalassinoides* burrows (Fig. 4.2), and is cemented by calcite and pyrite (Fig. 4.13. A, B, C, D, and E). Calcite cement occurs within intergranular, intragranular, and moldic pore spaces. Pyrite cement in this facies precipitated as both pyrite framboids and as clusters of cubic and octahedral pyrite within the stylolites (Fig. 4.13. C and D). Micritization of allochem grain margins is common and the micritized rims are composed of subhedral crystals of microspar (Fig. 4.13.A). Carbonate mud between the allochems is composed of euhedral microspar (Fig. 4.13.B) and indicates recrystallization of the original micritic matrix.

Facies 11 is 1’ 2” thick in the McFerren well. No core analysis of porosity and permeability is available; however, porosity is classified as interparticle, intraparticle, and moldic. Porosity and permeability have been reduced in Facies 11 by the precipitation of calcite and pyrite cement (Fig. 4.13. A, B, C, and D). Microporosity is abundant within this facies and occurs within/between the microcrystalline calcite crystals (Fig. 4.13. A and B). Minor amounts of carbonaceous material are also preserved in the facies as shown in Figure 4.13.E.

Environmental interpretation. The presence of abundant ooids suggests that this facies accumulated in a shallow, slightly hypersaline environment that was above fair-weather wave base. This facies is interpreted as being deposited on the margin of a carbonate shoal based on the abundance of preserved ooids.

12. Laminated Peloidal Grainstone

Description. Facies 12 is a peloid grainstone that includes lesser foraminifera, ostracods, and rudist fragments (Fig. 4.14. A and B). This facies contains horizontal

laminations and current ripples (Fig. 4.2), and is cemented by calcite and pyrite (Fig. 4.14. A, B, and D). Calcite cement occurs within intergranular, intragranular, and moldic pore spaces (Fig. 4.14. A and B). Pyrite cement in this facies precipitated as clusters of cubic and octahedral pyrite within allochem molds and stylolites (Fig. 4.14.D). Micritization of allochem grain margins is common (Fig. 4.14. A and B), and the micritized rims of allochems are composed of subhedral crystals of microspar (Fig. 4.14. E and F). Carbonate mud between the allochems is composed of euhedral microspar (Fig. 4.14.C) and indicates recrystallization of the original micritic matrix.

Facies 12 is 2’ 10” thick in the McFerren well. No core analysis of porosity and permeability is available; however, porosity is classified as interparticle and moldic (Fig. 4.14. A and B). Porosity and permeability have been reduced in Facies 12 by the precipitation of calcite and pyrite cement (Fig. 4.14. B and D). Microporosity is abundant within this facies and occurs within/between the microcrystalline calcite crystals (Fig. 4.14. C and D). An intact ooid can be seen in Figure 4.14.A and B with the internal structure and layering preserved.

Environmental interpretation. Facies 12 is a laminated and current rippled peloid grainstone (Figures 4.14.A and 4.14.B). The presence of fine-scale laminations and current ripples suggests a shallow marine environment of deposition that was above fair-weather wave base.

13. Burrowed Coated Grain Grainstone

Description. Facies 13 is a grainstone consisting primarily of non-skeletal carbonate grains (Fig. 4.2). Major grains include ooids, coated grains, crinoids and

intraclasts, and lesser amounts of gastropods and peloids. This facies contains *Thalassinoides* burrows (Fig. 4.2), and is cemented by calcite. There is a seam of horizontal serrate and horsetail stylolites at the top of the facies with an abundance of around ten per foot. Facies 13 is 6" thick in the McFerren well. The highest porosity and permeability values are 7.9% and 0.01 mD, and porosity is classified as interparticle, intraparticle, and moldic.

Environmental interpretation. The abundance of ooids and coated grains along with a lack of carbonate mud suggest a carbonate "shoal" environment above fair-weather wave base.

14. Rudistid Framestone

Description. Facies 14 is a rudistic framestone dominated by intergrown rudist shells, and ancillary grains dominated by peloids, miliolids, and coated grains (Fig. 4.2, 4.15-1, and 4.15-2) and lesser amounts of foraminifera, bryozoa, radiolaria, intraclasts, and echinoderms (Fig. 4.15-1. A, B, C, and D). Numerous horizontal horsetail and serrate are present in this facies with an abundance of more than fifty stylolites per foot (Fig. 4.2). Rudists occur in apparent growth position (Fig. 4.2), and are cemented by calcite, anhydrite, and pyrite (Fig. 4.15-1. C, 4.15-2. J and K). Calcite cement occurs within intergranular, intragranular, and moldic pore spaces (Fig. 4.15-1. C and D). Pyrite cement in this facies precipitated as framboids of cubic and octahedral pyrite within allochem molds and stylolites (Fig. 4.15-2. H and J). Anhydrite cement precipitated within intergranular and moldic pore spaces (Fig. 4.15-2.K). Micritization of allochem grain margins is common (Fig. 4.15-1. B, C, and D), and the micritized rims of allochems are

composed of subhedral crystals of microspar (Fig. 4.15-2.G). Carbonate mud between the allochems is composed of euhedral microspar (Fig. 4.15-1.F) and indicates recrystallization of the original micritic matrix.

Facies 14 is 11’ thick in the McFerren well. The highest porosity and permeability values are 16% and 5.04 mD, and porosity is classified as interparticle, intraparticle, and moldic. Porosity and permeability have been reduced in Facies 14 by the precipitation of calcite, pyrite, and anhydrite cement (Fig. 4.15-2. G, J, and K). Microporosity is abundant within this facies and occurs within/between the microcrystalline calcite crystals (Fig. 4.15-1. E and F).

Environmental interpretation. This facies consists of a framestone structure of rudists in growth position along with large rudist fragments. The presence of in-situ rudists suggests deposition as a patch reef.

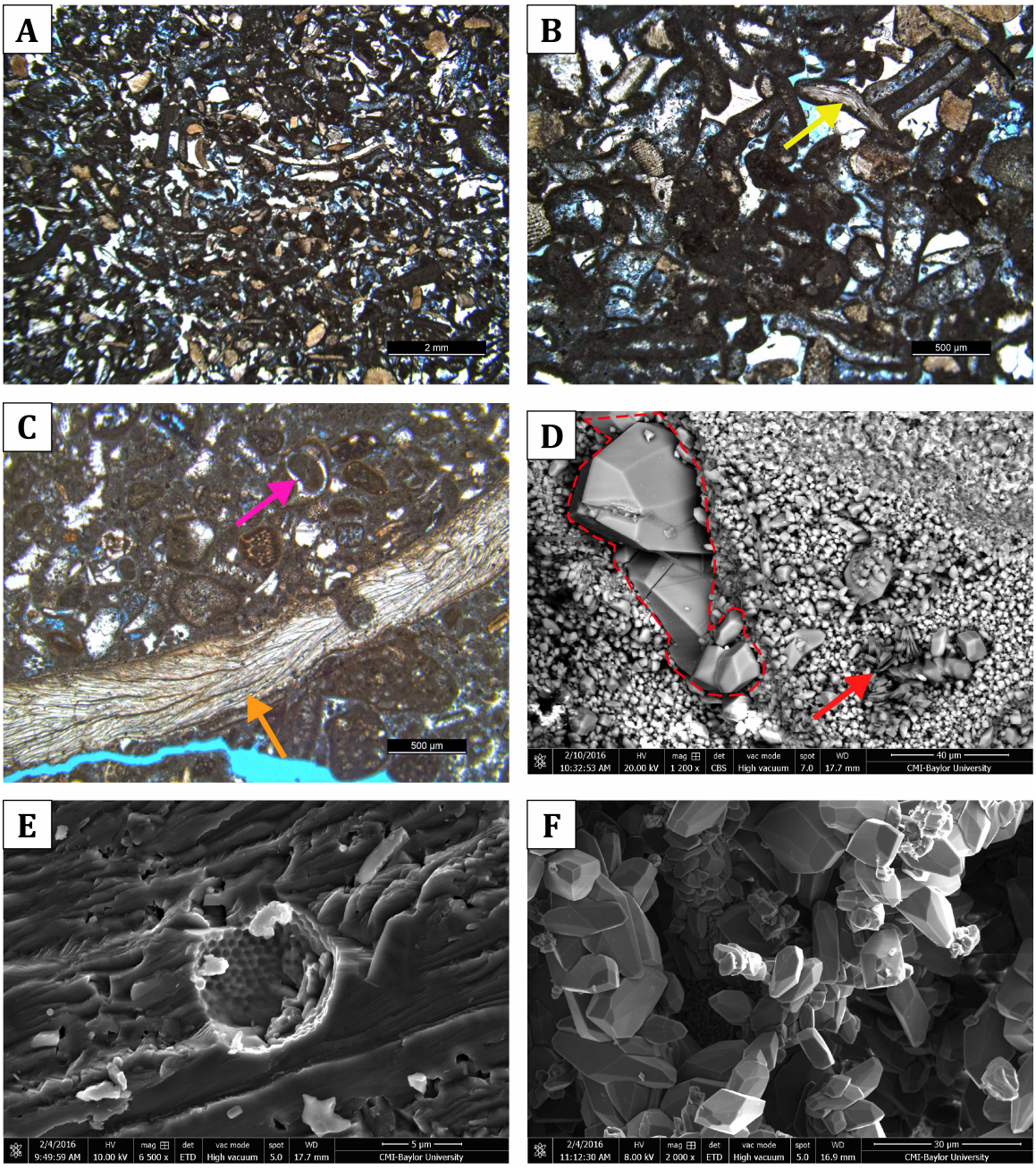

Figure 4.3. Facies 1 photomicrographs and SEM images. A) Photomicrograph (1.25x; B. DeBroeck 33-#1 well at 5,118') showing composition of the packstone-grainstone and distribution of porosity (blue areas). B) Photomicrograph (4x; B. DeBroeck 33-#1 well at 5,118') showing peloids and undifferentiated shell fragments, including a brachiopod fragment (yellow arrow) as well as abundant calcite cement (white areas). C) Photomicrograph (4x; B. DeBroeck 33-#1 well at 5,123') showing a large brachiopod fragment (orange arrow), a gastropod fragment (pink arrow), and peloids. D) Backscatter SEM image (1,200x; B. DeBroeck 33-#1 well at 5,117') showing calcite spar (red outline) surrounded by microcrystalline calcite, and clay booklets (red arrow). E) SEM image (6,500x; B. DeBroeck 33-#1 well at 5,123') showing the mold of a pyrite framboid. F) SEM image (2,000x; B. DeBroeck 33-#1 well at 5,120') showing porosity within calcite microspar.

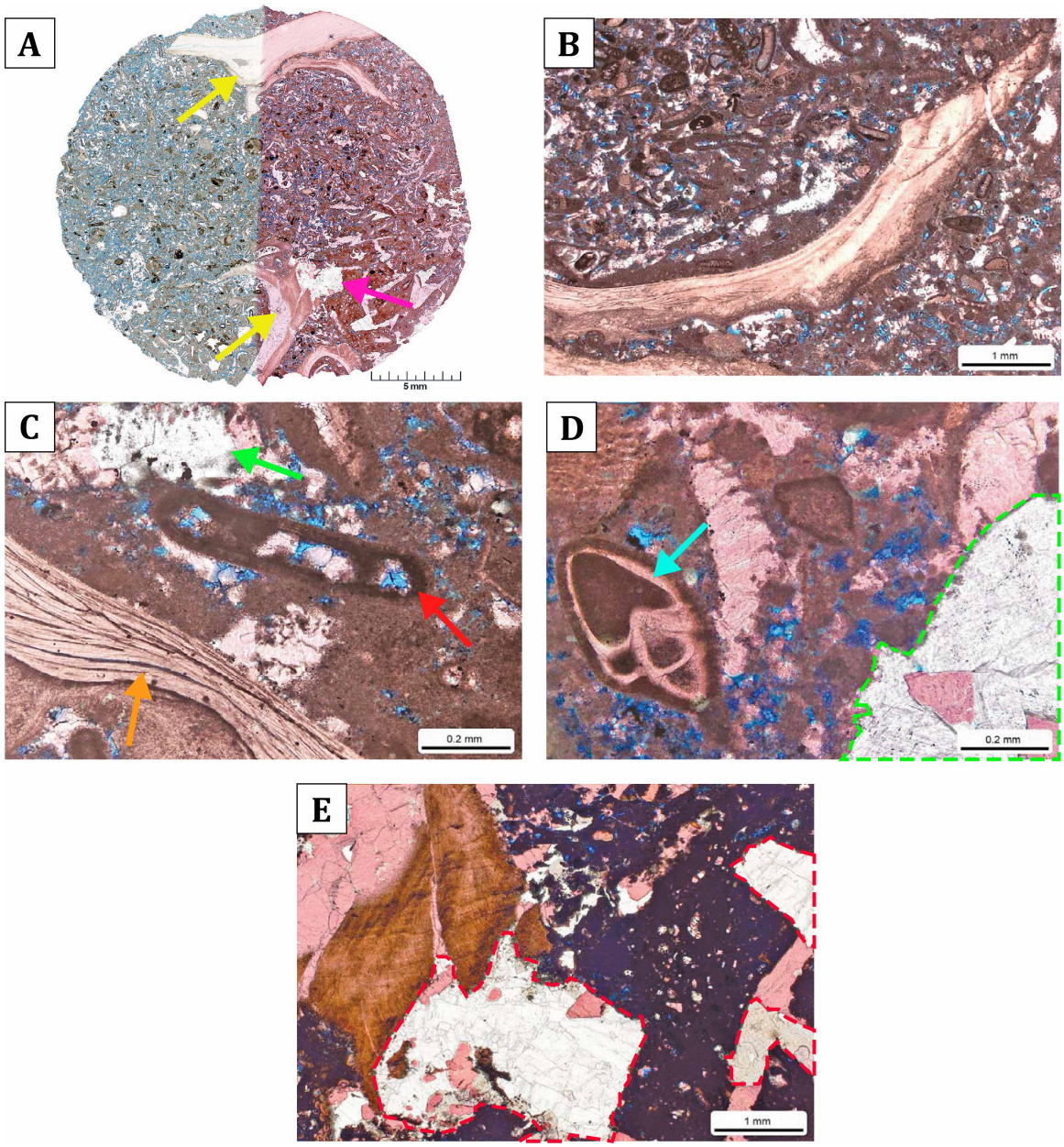

Figure 4.4. Facies 2 photomicrograph images (all photomicrographs are from the B. DeBroeck 33-#1 well at 5,123'). A) Image showing the general texture of the packstone, distribution of porosity (blue space), large brachiopod fragments (yellow arrows), and anhydrite cement (pink arrow). B) Higher magnification image showing packstone texture, porosity, and large brachiopod fragment. C) Image showing large brachiopod fragment (orange arrow), a micritized grain (red arrow) filled with calcite cement, and dolomite cement (green arrow). D) Image showing well preserved miliolid foraminifer filled and rimmed with micrite (teal arrow), and anhydrite cement (green outline). E) Image showing anhydrite cement (red outline) and carbonate mud/micrite (dark areas).

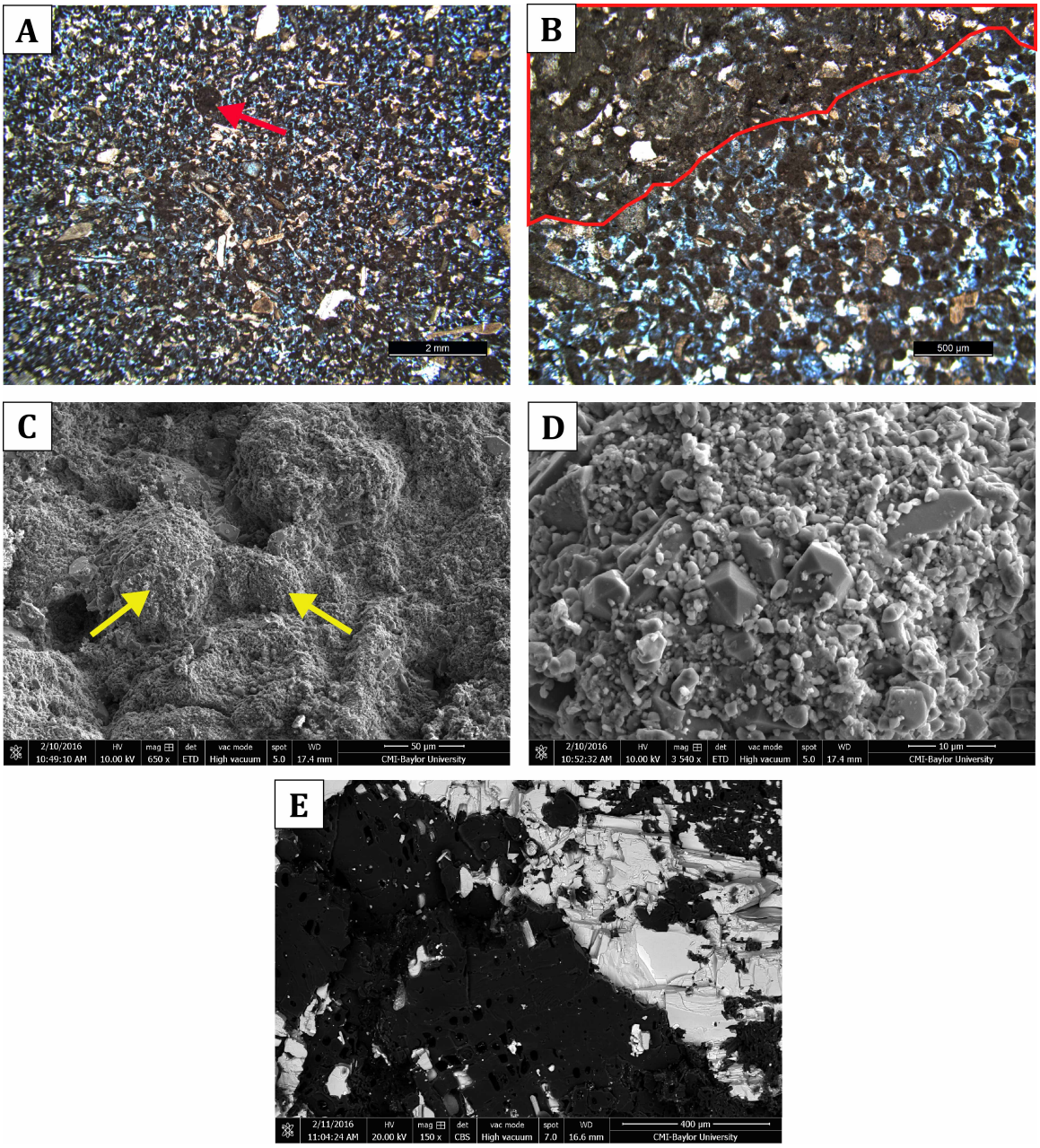

Figure 4.5. Facies 3 photomicrograph and SEM images. A) Photomicrograph (1.25x; B. DeBroeck 33-#1 well at 5,111') showing packstone texture, distribution of porosity, and large micritized peloid (red arrow). B) Photomicrograph (4x; B. DeBroeck 33-#1 well at 5,113') of a burrow preserved in the rock (red outline). C) SEM image (650x; B. DeBroeck 33-#1 well at 5,113') showing fine scale packstone texture and porosity, as well as possible peloids (yellow arrows). D) SEM image (3,540x; B. DeBroeck 33-#1 well at 5,113') of peloid surface showing recrystallized euhedral micrite. E) Backscatter SEM image (150X; B. DeBroeck 33-#1 well at 5,114') showing anhydrite cement (bright areas) filling pore space within carbonaceous material (dark areas).

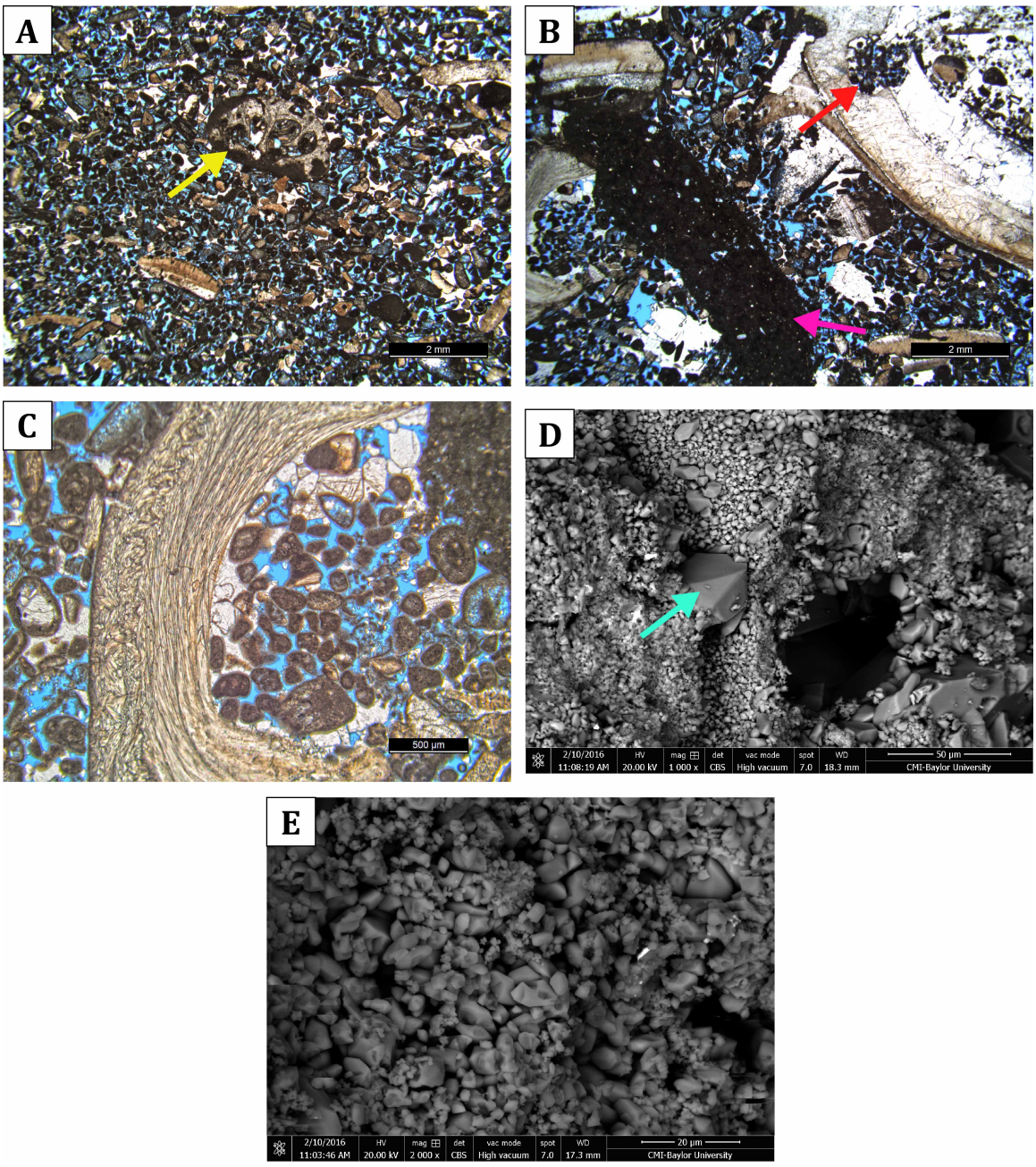

Figure 4.6. Facies 4 photomicrograph and SEM images. A) Photomicrograph (1.25x; B. DeBroeck 33-#1 well at 5,111') showing grainstone texture, distribution of porosity, and possible micritized coral fragment (yellow arrow). B) Photomicrograph (1.25x; B. DeBroeck 33-#1 well at 5,111') showing large intraclast (pink arrow) and a hole within a shell fragment filled with micritized grains (red arrow). C) Photomicrograph (4x; B. DeBroeck 33-#1 well at 5,111') of a large brachiopod fragment surrounded by micritized peloids. D) Backscatter SEM image (1,000x; B. DeBroeck 33-#1 well at 5,111.5') showing fine scale grainstone texture, porosity, and large calcite spar (teal arrow) surrounded by microcrystalline calcite. E) Backscatter SEM image (2,000x; B. DeBroeck 33-#1 well at 5,111.5') showing micritic carbonate texture and microporosity.

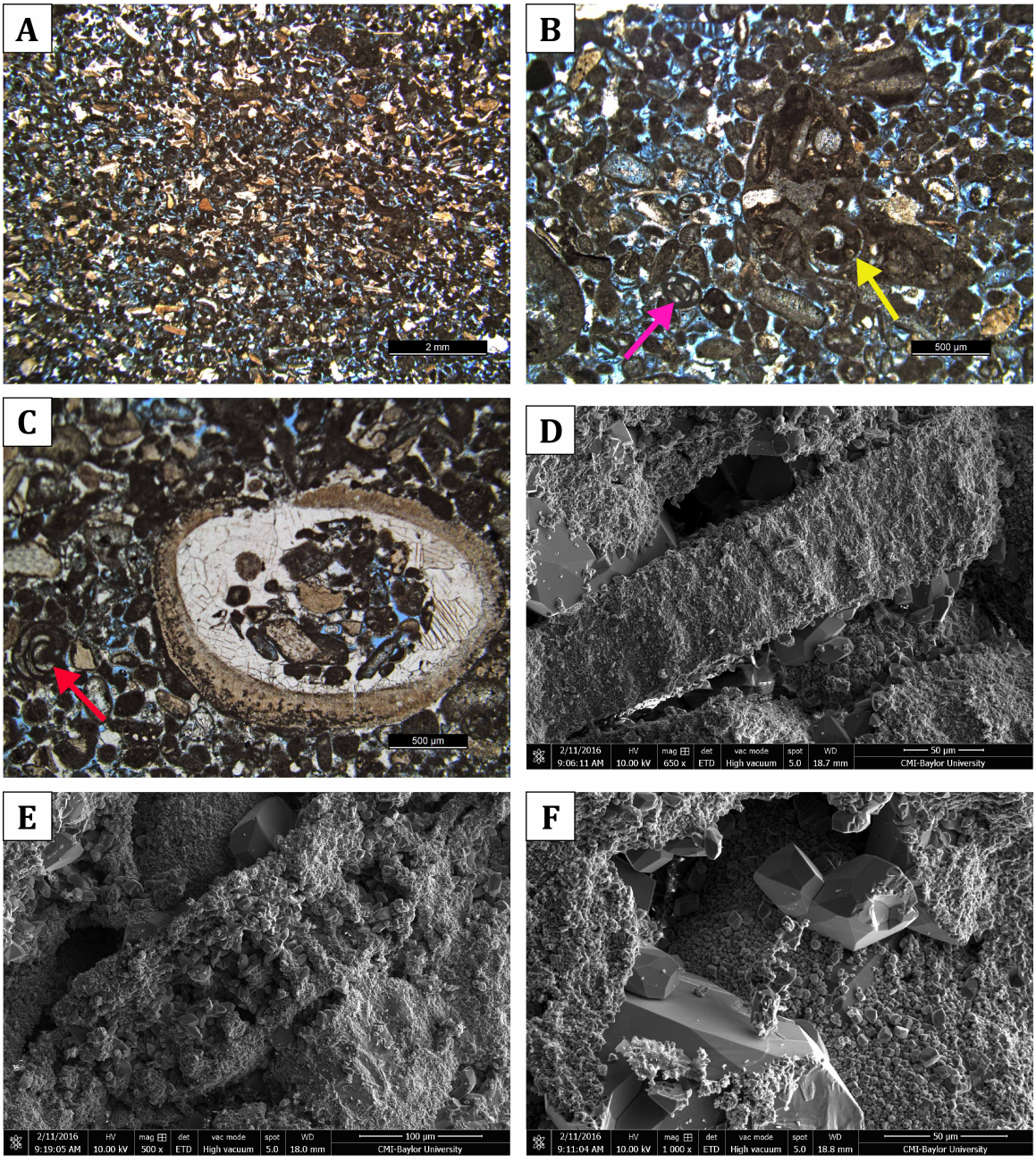

Figure 4.7. Facies 5 photomicrograph and SEM images. A) Photomicrograph (1.25x; B. DeBroeck 33-#1 well at 5,109') showing grainstone texture and distribution of porosity. B) Photomicrograph (4x; B. DeBroeck 33-#1 well at 5,110') showing a gastropod (yellow arrow) and miliolid foraminifer (pink arrow) surrounded by micritized peloids. C) Photomicrograph (4x; B. DeBroeck 33-#1 well at 5,109') showing miliolid foraminifer (red arrow) and a shell fragment filled with micritized grains and blocky cement. D) SEM image (650x; B. DeBroeck 33-#1 well at 5,110') showing fine scale grainstone texture and porosity as well as possible shell fragment structure. E) SEM image (500x; B. DeBroeck 33-#1 well at 5,110') showing fine scale grainstone texture and porosity as well as possible shell fragment structure. F) SEM image (1,000x; B. DeBroeck 33-#1 well at 5,110') showing micritic carbonate and a large intergranular pore as well as microcrystalline calcite surrounding calcite spar.

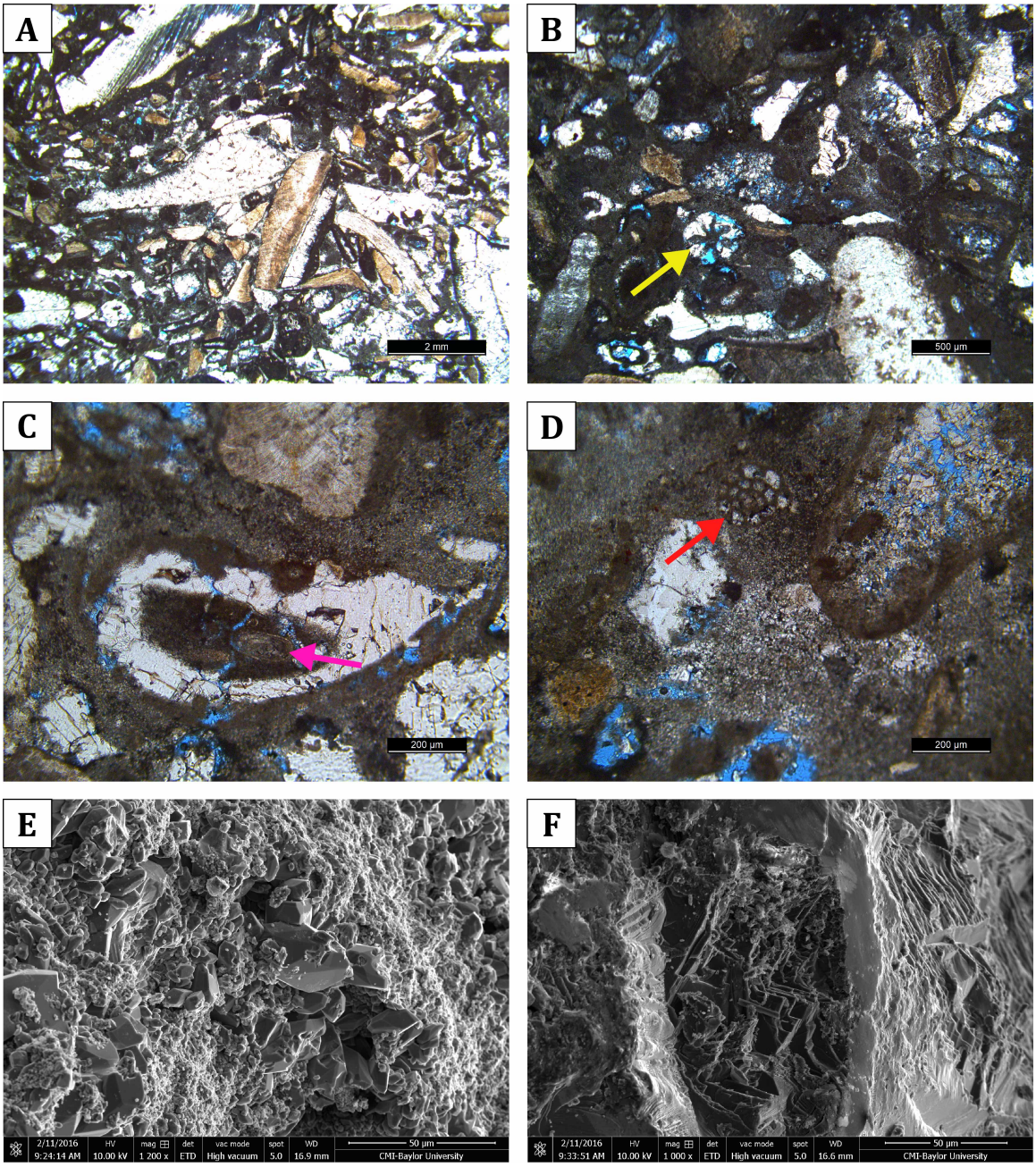

Figure 4.8. Facies 6 photomicrograph and SEM images. A) Photomicrograph (1.25x; B. DeBroeck 33-#1 well at 5,105') showing rudstone texture and distribution of porosity. B) Photomicrograph (4x; B. DeBroeck 33-#1 well at 5,105') showing highly micritized allochems as well as possible coral fragment (yellow arrow) with preserved intragranular porosity. C) Photomicrograph (10x; B. DeBroeck 33-#1 well at 5,105') showing highly micritized rock texture as well as a possible coated grain (pink arrow) surrounded by blocky cement. D) Photomicrograph (10x; B. DeBroeck 33-#1 well at 5,105') showing highly micritized rock texture as well as a planispiral foraminifer (red arrow). E) SEM image (1,200x; B. DeBroeck 33-#1 well at 5,106') showing the euhedral to subhedral texture of the carbonate mud. F) SEM image (1,000x; B. DeBroeck 33-#1 well at 5,106') showing the interior structure of a calcite spar crystal.

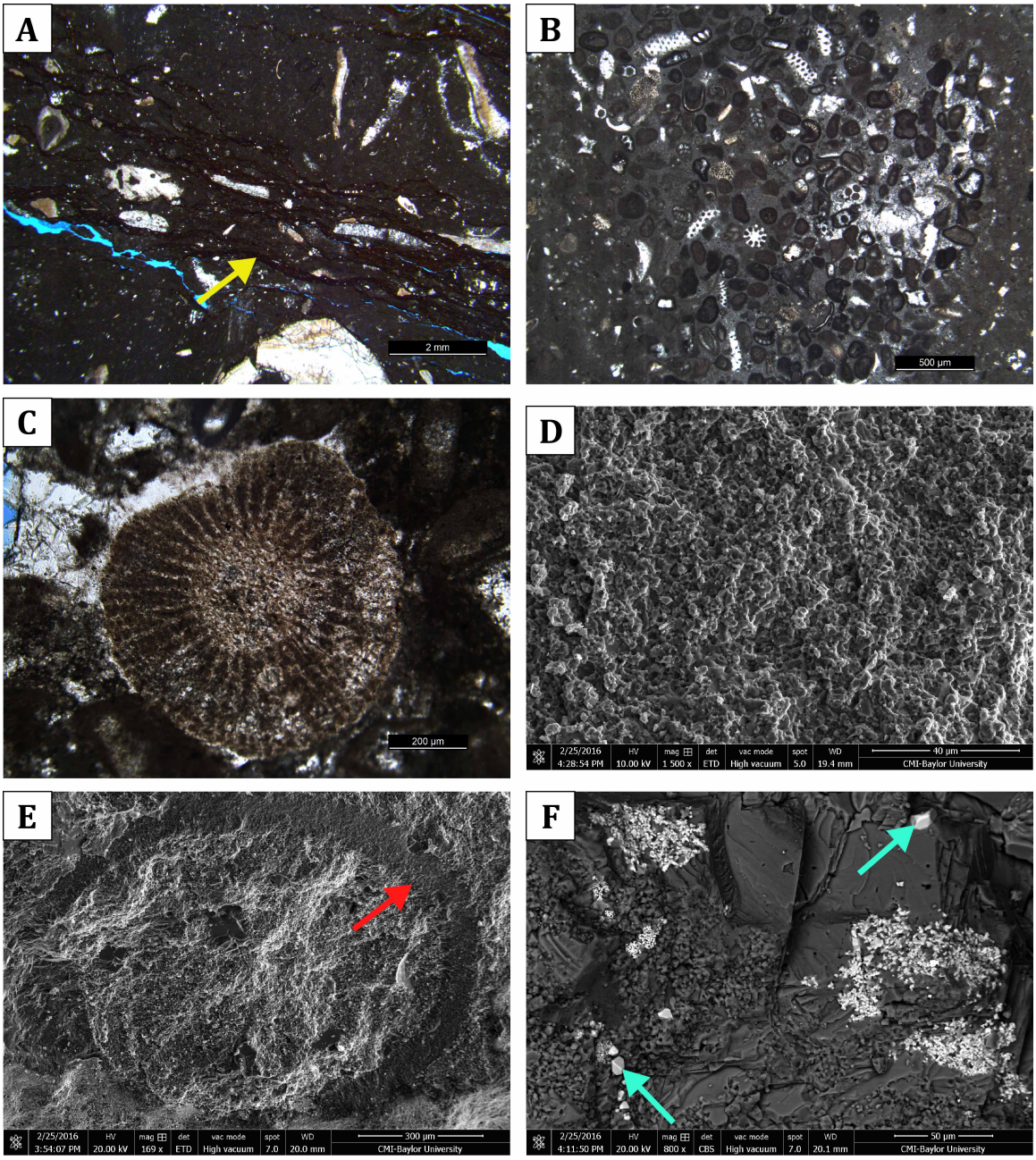

Figure 4.9. Facies 7 photomicrograph and SEM images. A) Photomicrograph (1.25x; McFerren 36-#2 well at 5,041') showing floatstone texture, distribution of porosity, and stylolites (yellow arrow). B) Photomicrograph (4x; B. DeBroeck 33-#1 well at 5,096') showing the composition of a preserved burrow. C) Photomicrograph (10x; B. DeBroeck 33-#1 well at 5,104') showing an echinoderm fragment surrounded by micritized allochems and cement. D) SEM image (1,500x; B. DeBroeck 33-#1 well at 5,104') showing fine scale floatstone texture and porosity. E) SEM image (169x; McFerren 36-#2 well at 5,041') showing fine scale floatstone texture and porosity as well as possible shell fragment structure. F) Backscatter SEM image (800x; McFerren 36-#2 well at 5,041') showing fine-grained disseminated pyrite (bright areas) as well as larger pyrite octahedrons (teal arrows).

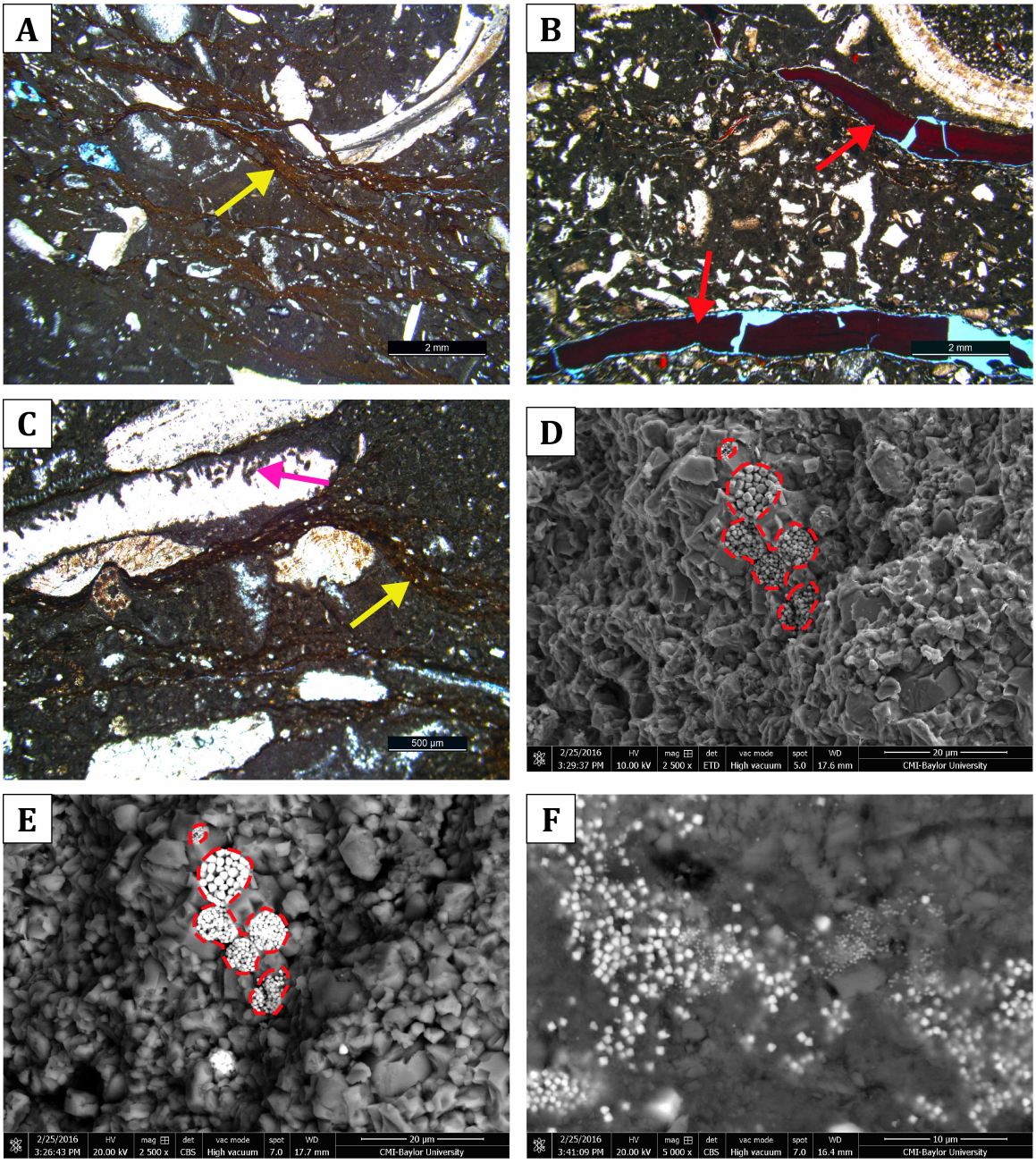

Figure 4.10. Facies 8 photomicrograph and SEM images. A) Photomicrograph (1.25x; McFerren 36-#2 well at 5,043') showing wackestone-packstone texture, distribution of porosity, and stylolites (yellow arrow). B) Photomicrograph (1.25x; B. DeBroeck 33-#1 well at 5,103') showing highly micritized rock texture as well as carbonaceous material (red arrows). C) Photomicrograph (4x; B. DeBroeck 33-#1 well at 5,101') showing stylolites (yellow arrow) and borings into a shell fragment (pink arrow). D) SEM image (2,500x; McFerren 36-#2 well at 5,043') showing fine scale wackestone-packstone texture and porosity, as well as pyrite framboids (red outline). E) Same image as D (2,500x; McFerren 36-#2 well at 5,043') but using backscatter SEM imaging to highlight the pyrite framboids (red outline). F) Backscatter SEM image (5,000x; McFerren 36-#2 well at 5,043') showing distribution of pyrite (bright areas).

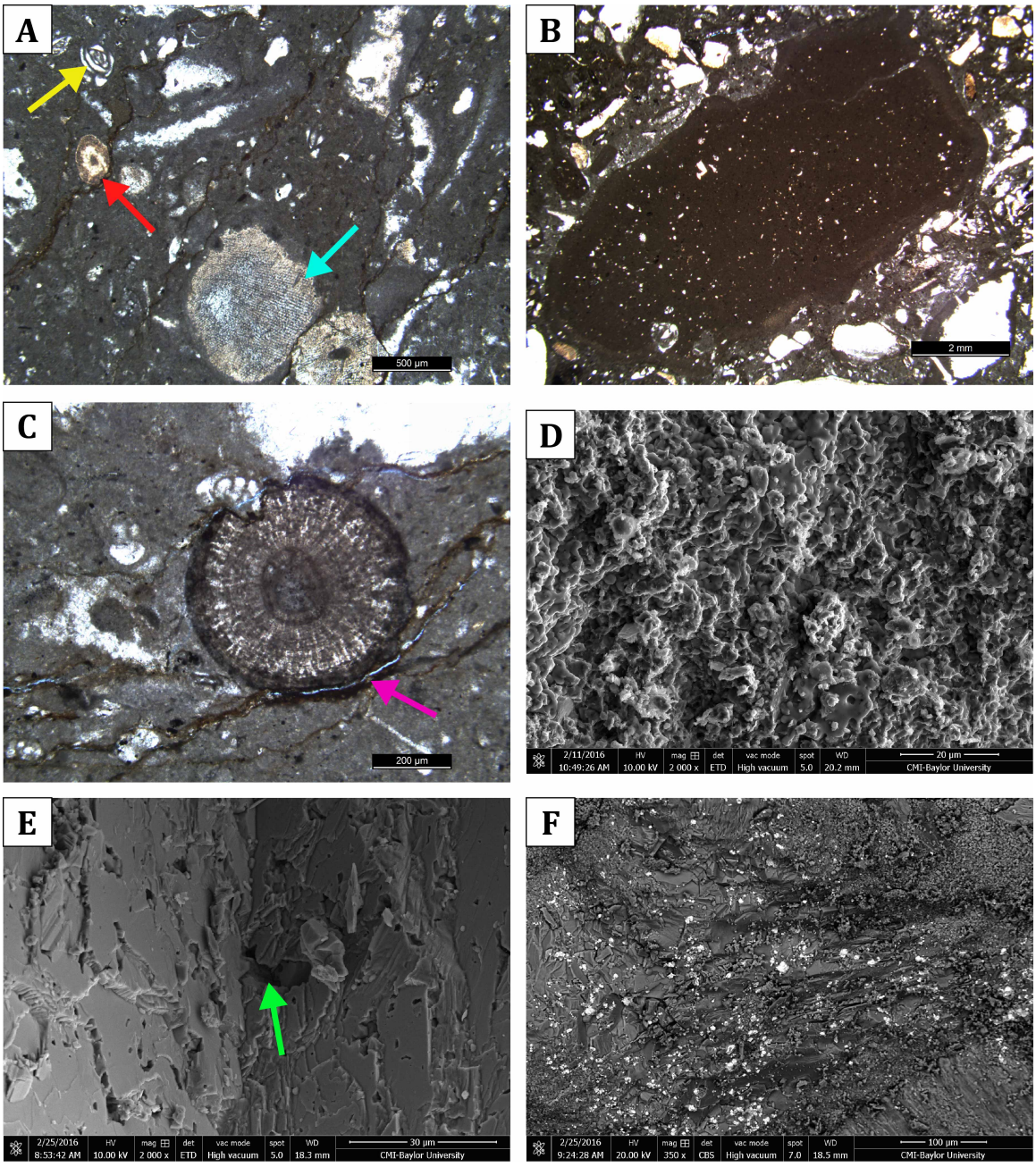

Figure 4.11. Facies 9 photomicrograph and SEM images. A) Photomicrograph (4x; B. DeBroeck 33-#1 well at 5,098') showing floatstone texture and distribution of porosity, as well as a miliolid foraminifer (yellow arrow), a possible ooid (red arrow), and an algae fragment (teal arrow). B) Photomicrograph (1.25x; B. DeBroeck 33-#1 well at 5,101') showing a large intraclast surrounded by highly micritized allochems. C) Photomicrograph (10x; B. DeBroeck 33-#1 well at 5,098') showing an ooid with preserved structure and a micritized rim and stylolites (pink arrow). D) SEM image (2,000x; B. DeBroeck 33-#1 well at 5,098') showing fine scale floatstone texture and porosity. E) SEM image (2,000x; McFerren 36-#2 well at 5,071') showing porosity within dissolution holes in large calcite spar. F) Backscatter SEM image (350x; McFerren 36-#2 well at 5,071') showing distribution of pyrite (bright areas).

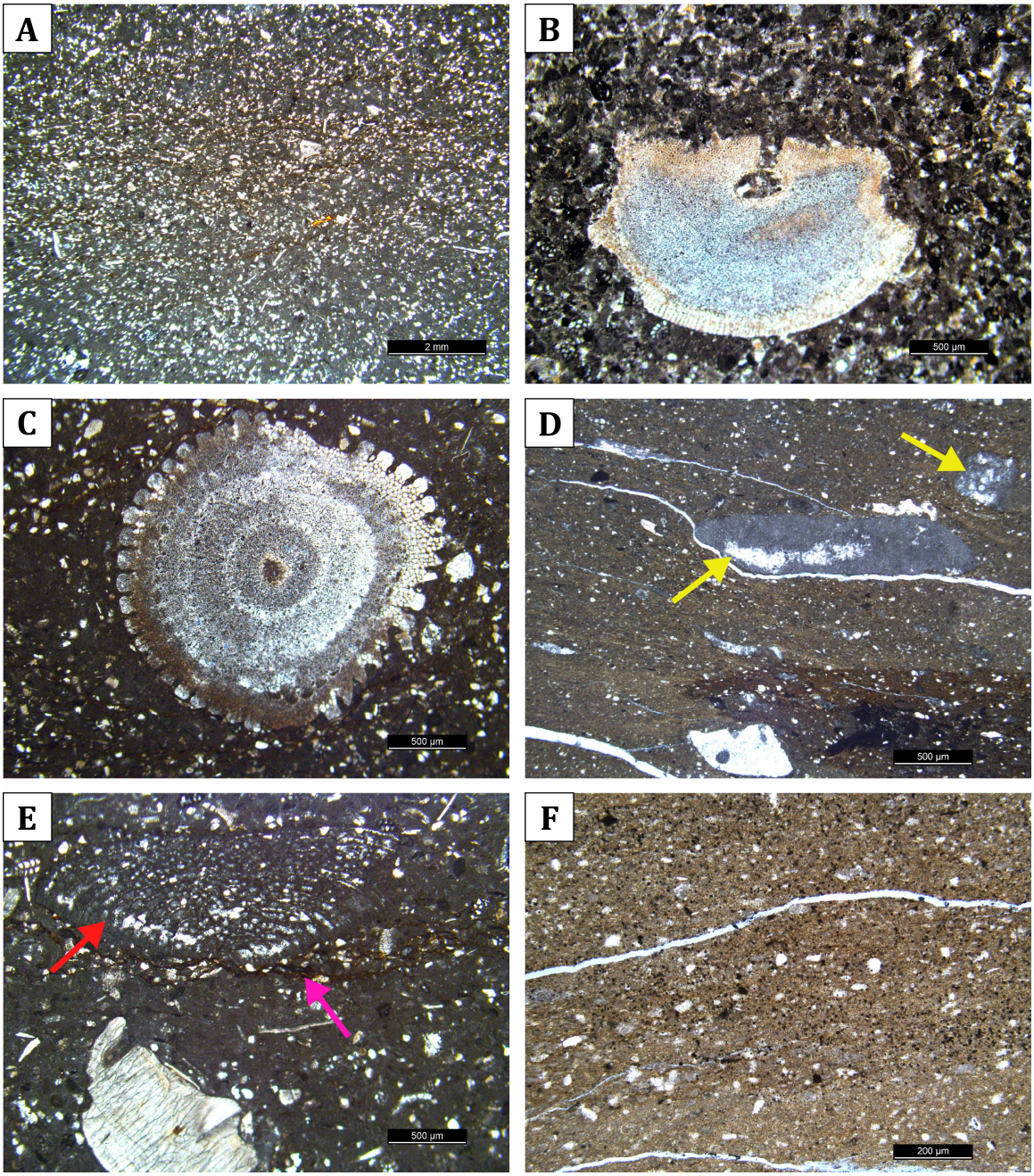

Figure 4.12. Facies 10 photomicrograph images. A) Image (1.25x; McFerren 36-#2 well at 5,063') showing mudstone-wackestone texture and distribution of porosity. B) Image (4x; McFerren 36-#2 well at 5,067') showing an echinoderm fragment surrounded by highly micritized peloids. C) Image (4x; McFerren 36-#2 well at 5,063') showing a cross-section of an echinoderm spine surrounded by highly micritized allochems and carbonate mud. D) Image (4x; B. DeBroeck 33-#1 well at 5,097') showing large intraclasts (yellow arrows). E) Image (4x; McFerren 36-#2 well at 5,063') showing stylolites (pink arrow) and orbitolinid foraminifer (red arrow) with preserved intragranular porosity, as well as large, blocky calcite cement. F) Image (10x; B. DeBroeck 33-#1 well at 5,097') showing mudstone-wackestone texture and distribution of porosity.

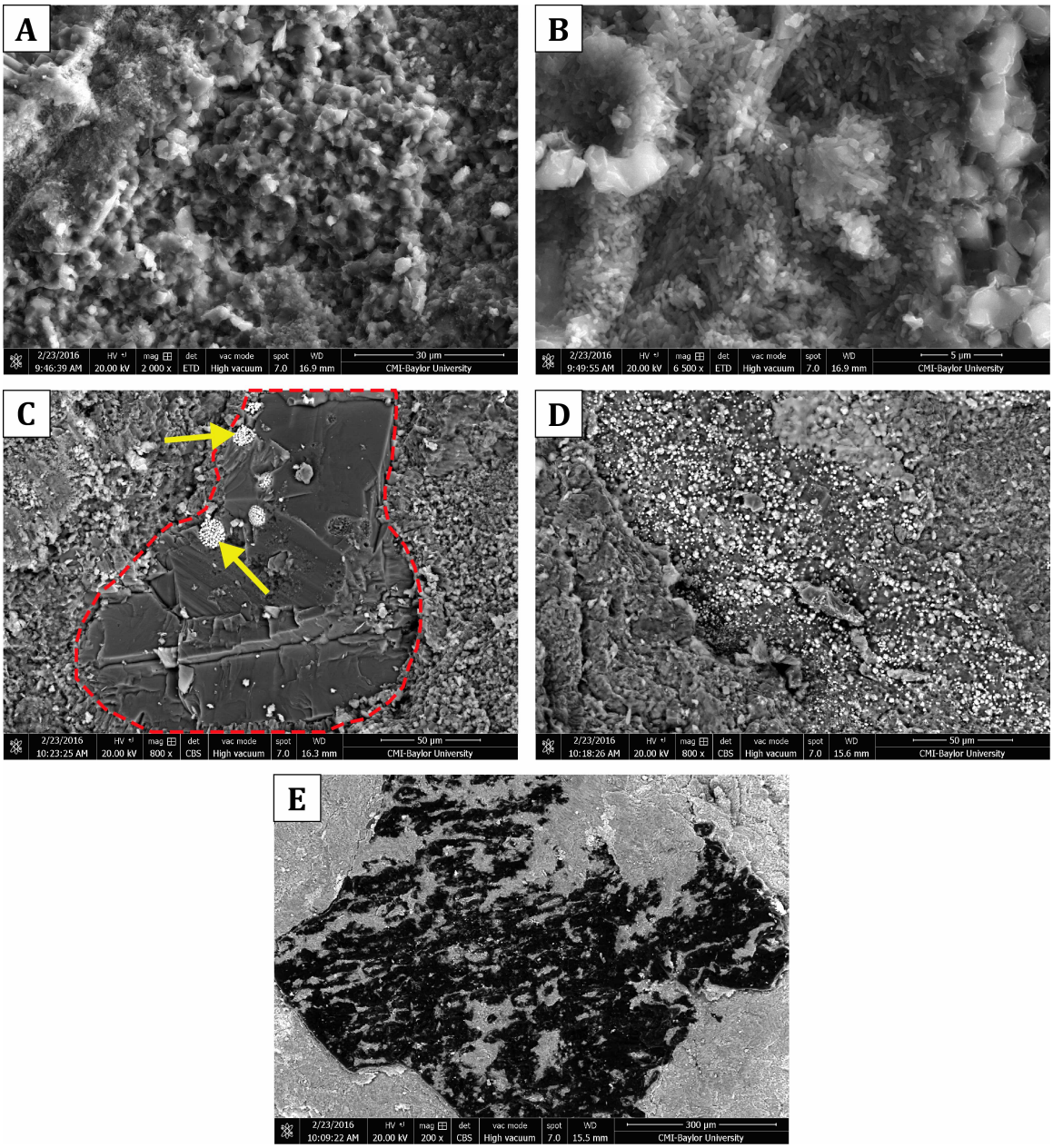

Figure 4.13. Facies 11 SEM images. A) SEM image (2,000x; McFerren 36-#2 well at 5,061') showing fine scale packstone texture and porosity. B) SEM image (6,500x; McFerren 36-#2 well at 5,061') showing subhedral to euhedral microspar crystal cement with abundant microporosity. C) Backscatter SEM image (800x; McFerren 36-#2 well at 5,061') showing pyrite framboids (yellow arrows) within large calcite spar (red outline) surrounded by microcrystalline calcite. D) Backscatter SEM image (800x; McFerren 36-#2 well at 5,061') showing distribution of pyrite (bright areas) within a stylolite. E) Backscatter SEM image (200x; McFerren 36-#2 well at 5,061') showing pyrite (bright areas) and calcite filling in porosity and surrounding carbonaceous material (dark areas).

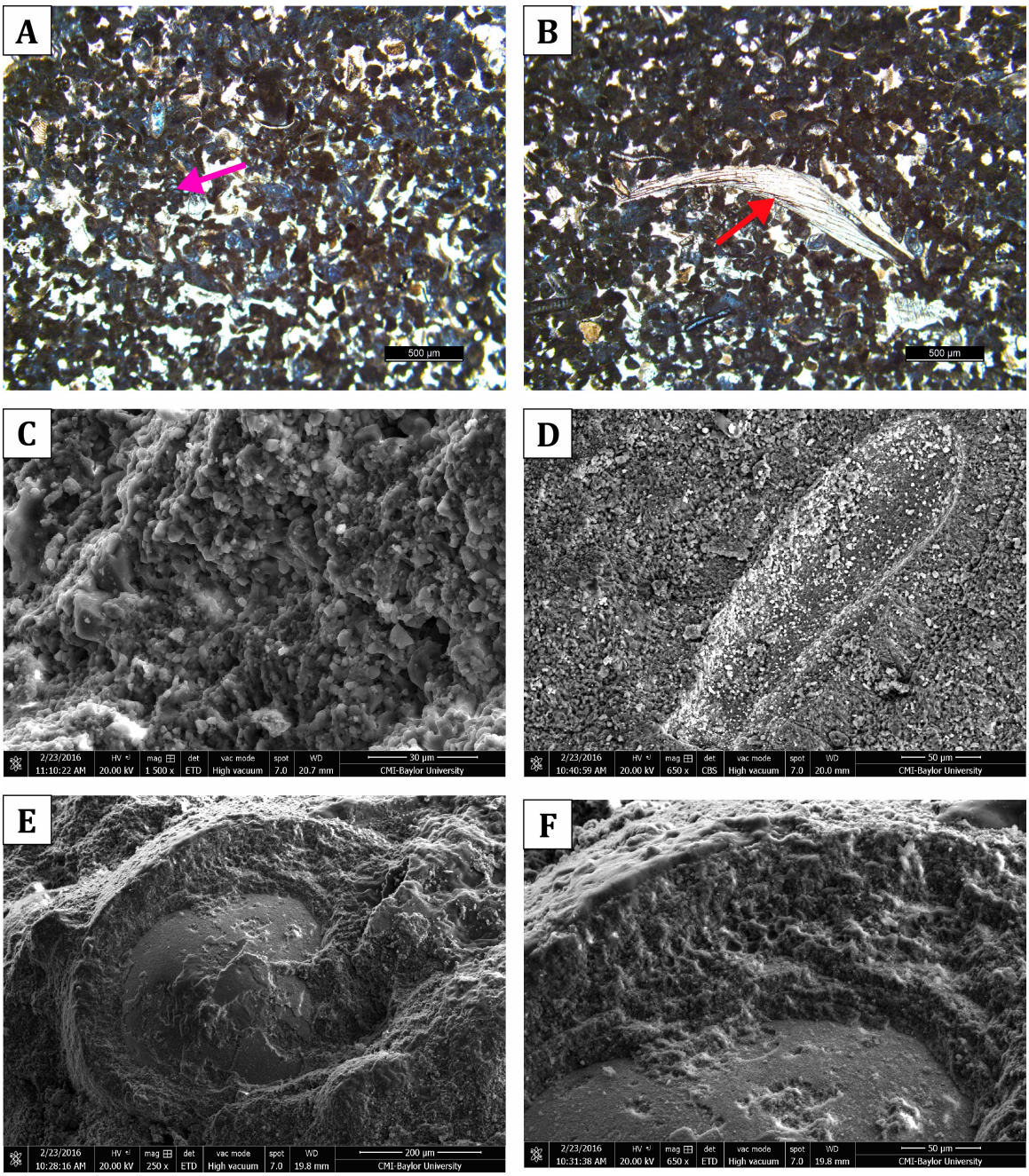

Figure 4.14. Facies 12 photomicrograph and SEM images. A) Photomicrograph (4x; McFerren 36-#2 well at 5,059') showing grainstone texture, distribution of porosity, and a biserial foraminifer (pink arrow). B) Photomicrograph (4x; McFerren 36-#2 well at 5,059') showing a large rudist fragment (red arrow) surrounded by highly micritized peloids and other grains. C) SEM image (1,500x; McFerren 36-#2 well at 5,059.5') showing fine scale grainstone texture and porosity. D) Backscatter SEM image (650x; McFerren 36-#2 well at 5,059.5') showing possible allochem mold with pyrite filling the pore space (bright areas). E) SEM image (250x; McFerren 36-#2 well at 5,059.5') showing an ooid. F) SEM image (650x; McFerren 36-#2 well at 5,059.5') showing the interior structure of an ooid with the layering preserved.

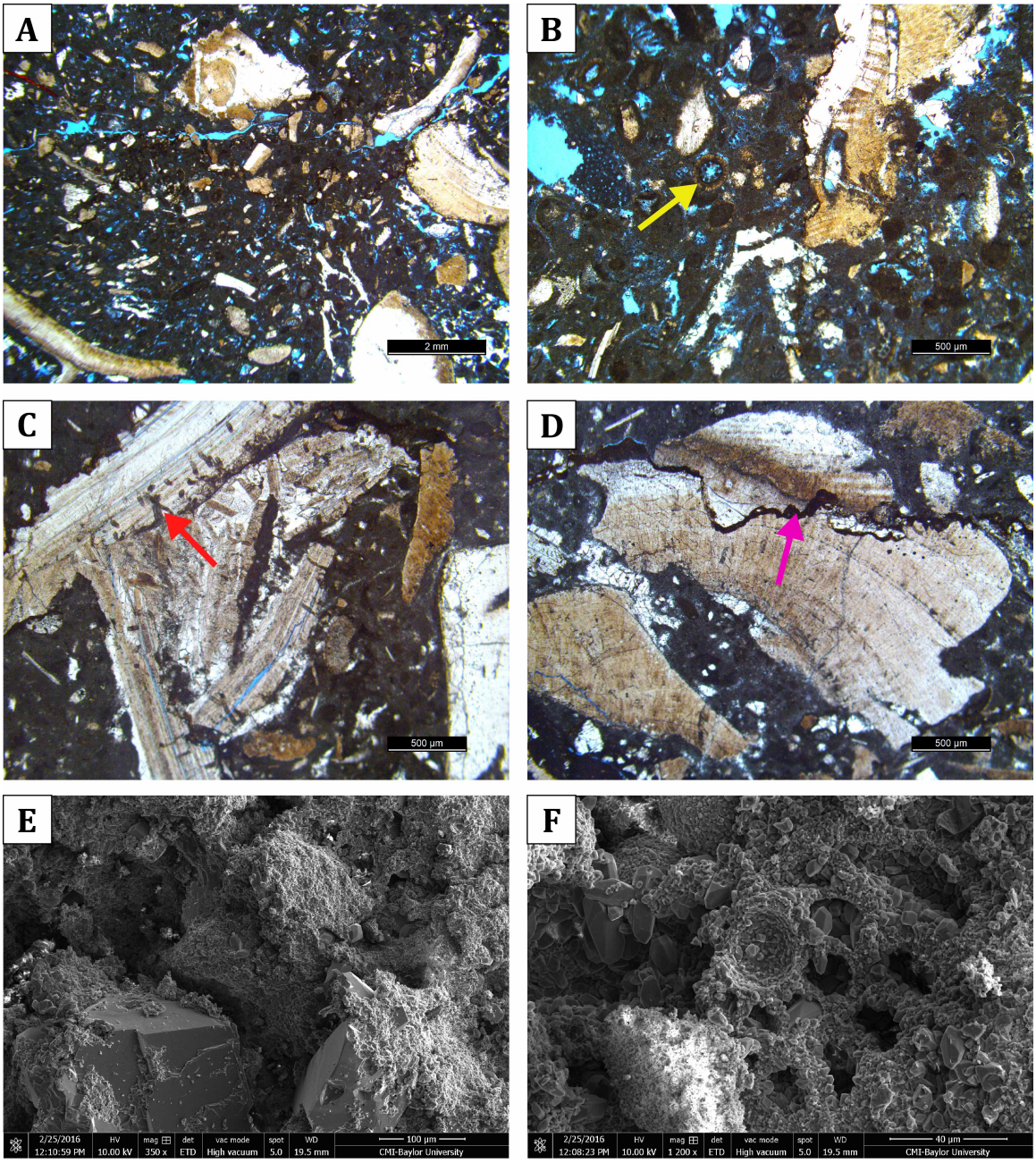

Figure 4.15-1. Facies 14 photomicrograph and SEM images. A) Photomicrograph (1.25x; McFerren 36-#2 well at 5,048') showing framestone texture and distribution of porosity. B) Photomicrograph (4x; McFerren 36-#2 well at 5,048') showing a coated grain (yellow arrow) surrounded by micritized allochems. C) Photomicrograph (4x; McFerren 36-#2 well at 5,055') showing borings into shell fragments (red arrow) with preserved internal structure. D) Photomicrograph (4x; McFerren 36-#2 well at 5,055') showing a stylolite (pink arrow) cutting through a shell fragment. E) SEM image (350x; McFerren 36-#2 well at 5,048') showing fine scale framestone texture and porosity. F) SEM image (1,200x; McFerren 36-#2 well at 5,048') showing moldic porosity.

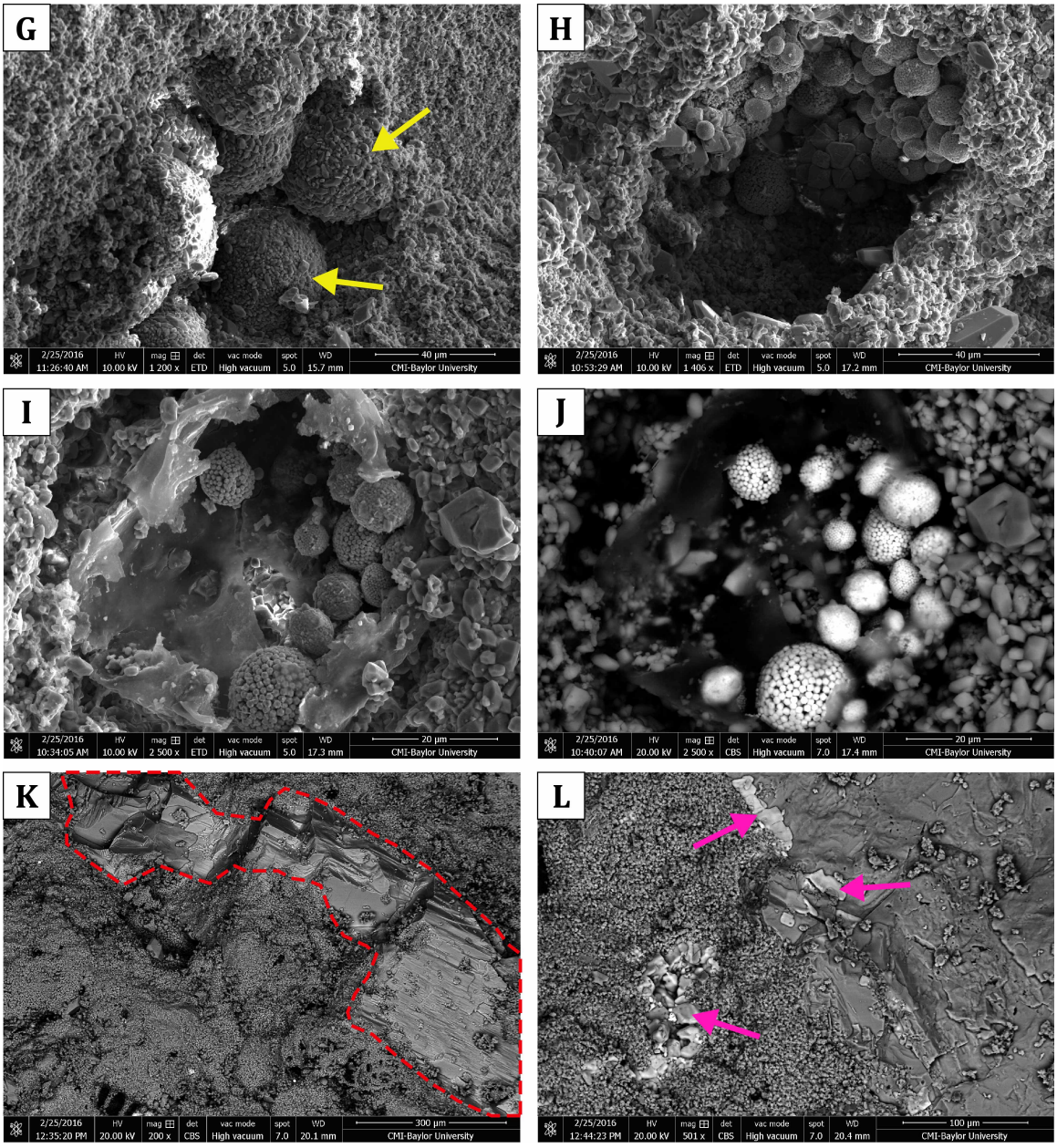

Figure 4.15-2. Facies 14 SEM images. G) SEM image (1,200x; McFerren 36-#2 well at 5,049') showing fine scale framestone texture and porosity, as well as possible peloids (yellow arrows). H) SEM image (1,406x; McFerren 36-#2 well at 5,050') showing pyrite framboids within a large secondary pore. I) SEM image (2,500x; McFerren 36-#2 well at 5,050') showing pyrite framboids within a secondary pore surrounded by carbonaceous film. J) Same image (2,500x; McFerren 36-#2 well at 5,050') as I but using backscatter imaging to highlight pyrite framboids (bright areas). K) Backscatter SEM image (200x; McFerren 36-#2 well at 5,048') showing anhydrite crystal (red outline) within microcrystalline calcite. L) Backscatter SEM image (501x; McFerren 36-#2 well at 5,048') showing NaCl salt (pink arrows) within calcite.

Facies Description Summary

Of the fourteen lithofacies identified, five occur in both core. Figures 4.16 and 4.17 are full core photographs showing the B. DeBroeck 33-#1 core and the McFerren 36-#2 core. A stratigraphic depiction of both core showing the distribution of facies, lithologies, major grains, and sedimentary structures is presented in Figure 4.18. Additionally, a summary table of the 14 lithofacies and their attributes is presented in Table 4.1-1 and 4.1-2.

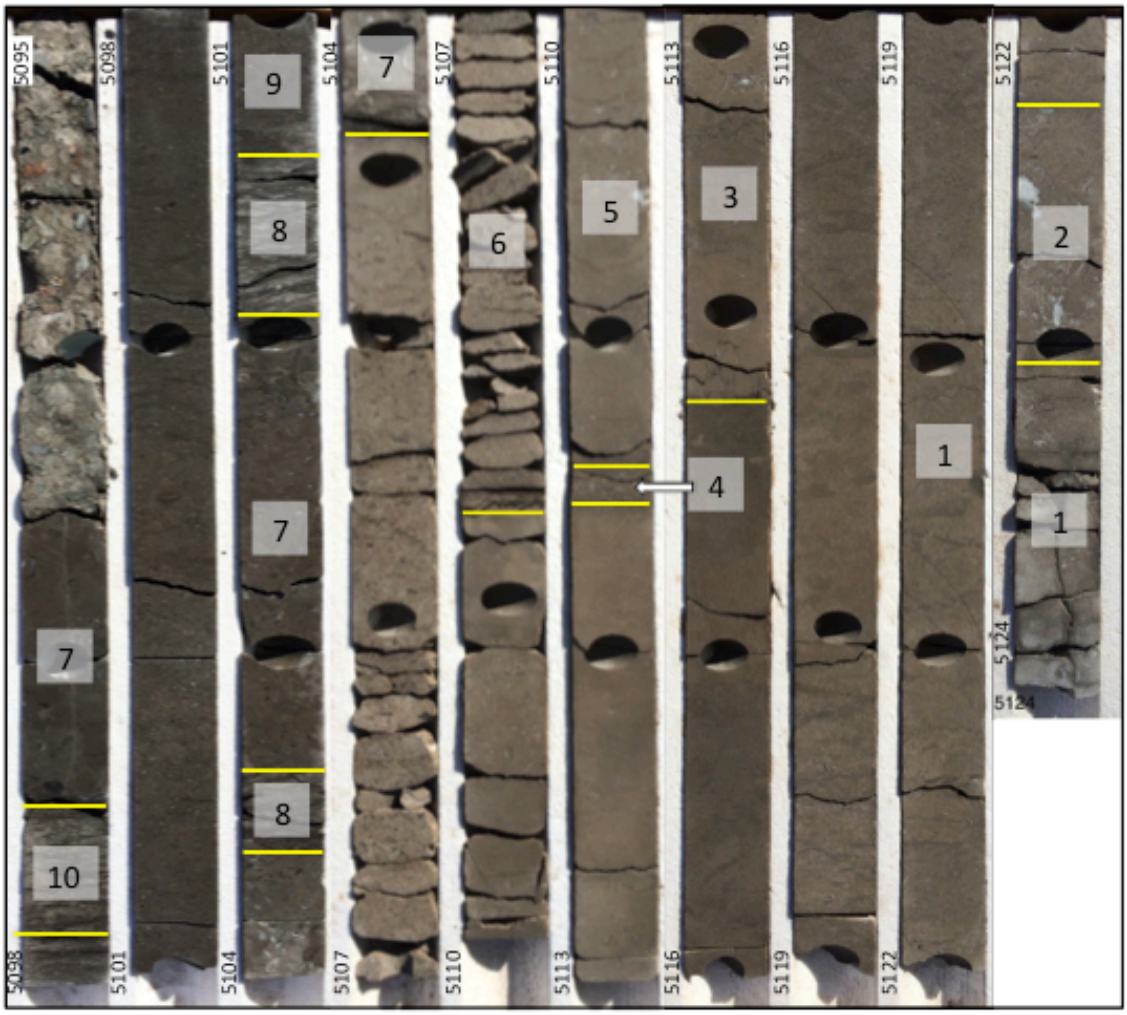

Figure 4.16. Core photograph of the B. DeBroeck 33-#1 core layout annotated with facies distributions. Depths (feet) are noted in the sidetracks.

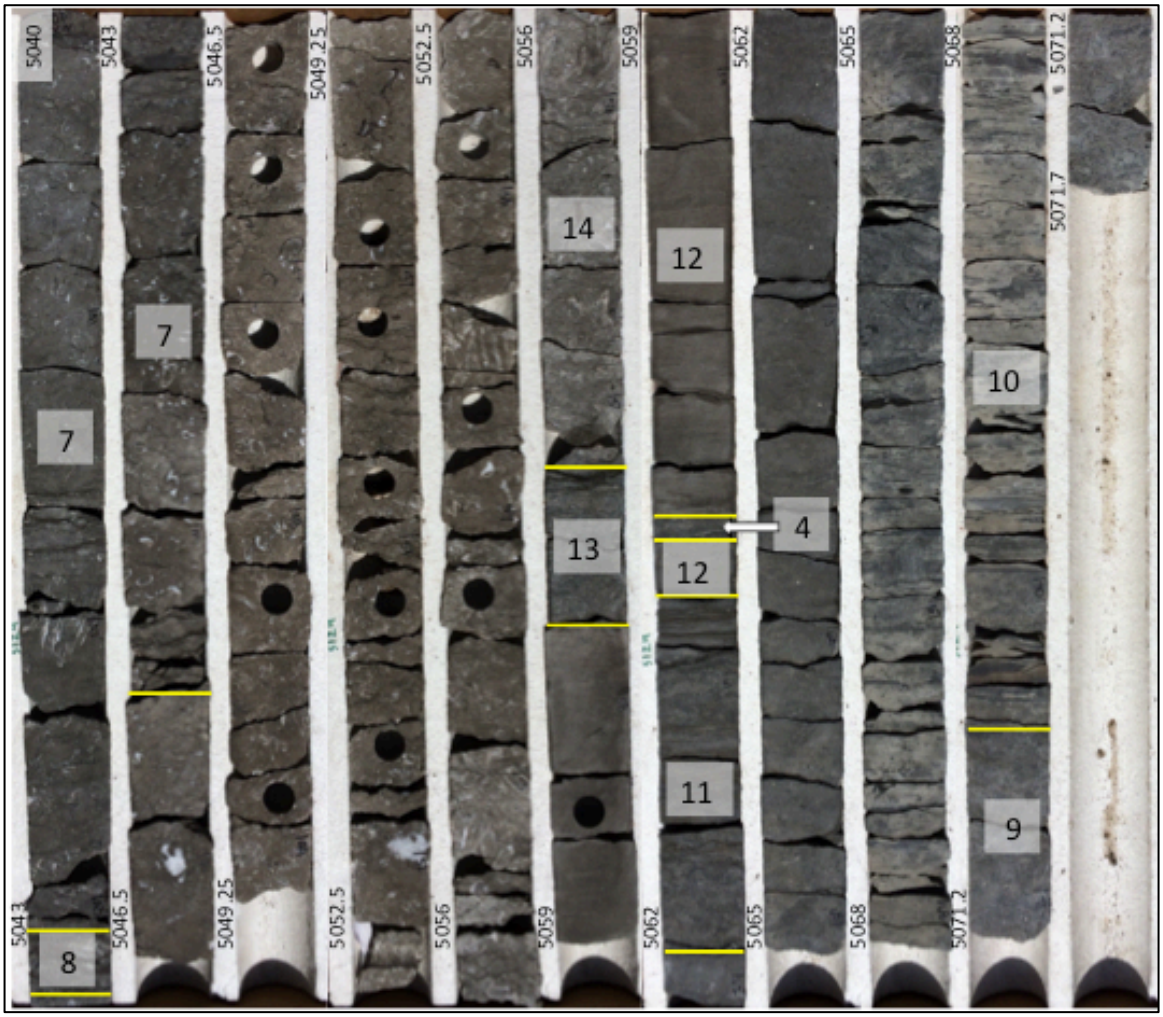

Figure 4.17. Core photograph of the McFerren 36-#2 core layout annotated with facies distributions. Depths (feet) are noted in the sidetracks.

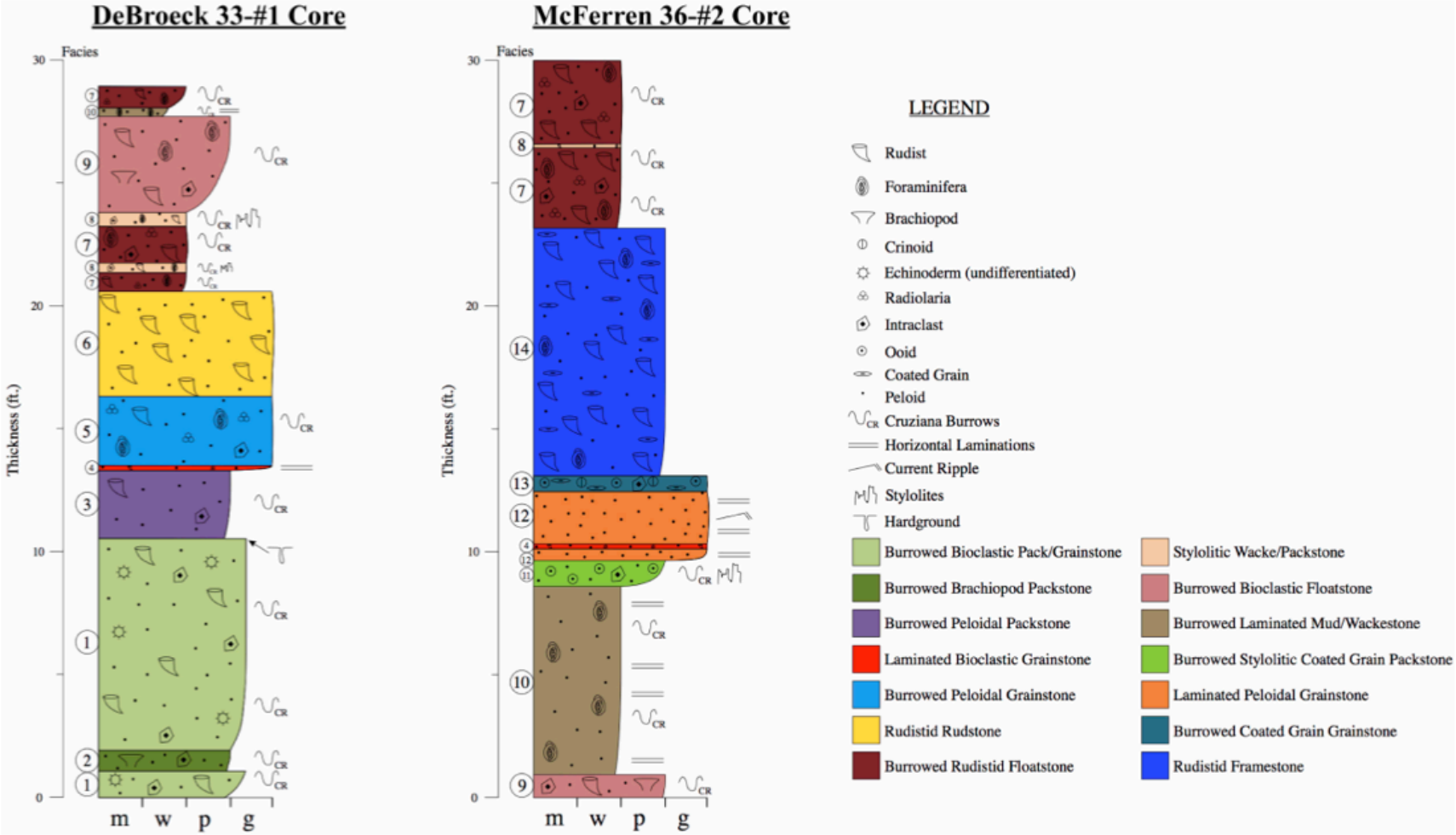

Figure 4.18. Core stratigraphic columns for each cored well showing the distribution of facies, major grains, and sedimentary structures present.

Table 4.1-1. Facies 1 through 7 Summary Table

Facies Label	1	2	3	4	5	6	7
Lithofacies Name	Burrowed Bioclastic Pack/Grainstone	Burrowed Brachiopod Packstone	Burrowed Peloidal Packstone	Laminated Bioclastic Grainstone	Burrowed Peloidal Grainstone	Rudistid Rudstone	Burrowed Rudistid Floatstone
Depositional Environment	Open Marine (below wave base)	Open Marine (below wave base)	Open Marine (below wave base)	Open Marine (below wave base)	Open Marine (below wave base)	Patch Reef Margin Debris	Subtidal (edge of patch reef)
Whole-Rock Texture	N/A	N/A	N/A	N/A	N/A	Rudstone	Floatstone
Matrix Texture	Pack/Grainstone	Packstone	Packstone	Grainstone	Grainstone	Grainstone	Wacke/Packstone
Major Grains	Rudist Fragments, Peloids, Echinoderm, Intraclasts	Brachiopod Fragments, Peloids, Intraclasts	Peloids, Intraclasts, Rudist Fragments	Peloids, Intraclasts, Rudist Fragments	Peloids, Rudist Fragments, Miliolid Forams, Intraclasts, Radiolaria	Rudist Fragments, Peloids	Rudist Fragments, Intraclasts, Peloids, Radiolaria, Miliolid Forams, Biserial Forams
Minor Grains	Gastropods, Radiolaria, Bryozoa, Biserial Forams, Miliolid Forams, Orbitolinid Forams, Coral, Grapestones, Coated Grains, Ostracods, Charophyte, Brachiopod Fragments	Echinoderm, Coated Grains, Biserial Forams, Miliolid Forams, Radiolaria	Radiolaria, Echinoderm, Miliolid Forams, Orbitolinid Forams, Biserial Forams, Planispiral Forams, Gastropods	Radiolaria, Echinoderm, Miliolid Forams, Gastropods, Brachiopod Fragments, Biserial Forams, Coral	Brachiopod Fragments, Gastropods, Coatred Grains, Ostracod, Biserial Forams, Echinoderms, Radiolaria, Planispiral Forams	Intraclasts, Coated Grains, Echinoderm, Planispiral Forams, Miliolid Forams, Biserial Forams, Bryozoa, Gastropods	Gastropods, Bivalve Undiff., Planispiral Forams, Algae, Echinoderm, Ostracod, Bryozoa, Charophyte
Sedimentary Structures	*Thalassinoides* Burrows	*Thalassinoides* Burrows	*Thalassinoides* Burrows	Horizontal Laminations	*Thalassinoides* Burrows	N/A	*Thalassinoides* Burrows
Notes			Hard Ground	Tempestite			

Table 4.1-2. Facies 8 through 14 Summary Table

Facies Label	8	9	10	11	12	13	14
Lithofacies Name	Stylolitic Wacke/Packstone	Burrowed Bioclastic Floatstone	Burrowed Laminated Mud/Wackestone	Burrowed Stylolitic Coated Grain Packstone	Laminated Peloidal Grainstone	Burrowed Coated Grain Grainstone	Rudistid Framestone
Depositional Environment	Deeper Marine (above 30m depth)	Open Marine (below wave base)	Deeper Marine (above 30m depth)	Carbonate Shoal Margin	Shallow Marine (above fair-weather wave base)	Carbonate Shoal	Rudist Patch Reef
Whole-Rock Texture	N/A	Floatstone	N/A	N/A	N/A	N/A	Framestone
Matrix Texture	Wacke/Packstone	Packstone	Mud/Wackestone	Packstone	Grainstone	Grainstone	Packstone
Major Grains	Rudist Fragments, Intraclasts, Biserial Forams, Peloids, Miliolid Forams	Rudist Fragments, Miliolid Forams, Intraclasts, Peloids, Brachiopod Fragments	Quartz Grains, Miliolid Forams, Planispiral Forams, Biserial Forams, Peloids	Peloids, Intraclasts, Ooids	Peloids	Ooids, Coated Grains, Crinoids, Intraclasts	Rudist Fragments, Miliolid Forams, Coated Grains, Peloids
Minor Grains	Crinoid, Algae, Planispiral Forams, Charophyte, Ostracod, Radiolaria, Coated Grains, Intraclasts, Brachiopod Fragments	Ooids, Coral, Algae, Biserial Forams, Radiolaria, Crinoids, Echinoderms, Planispiral Forams, Gastropods, Ostracod, Orbitolinid Forams, Radiolaria	Radiolaria, Intraclasts, Ostracod, Echinoderms, Brachiopod Fragments, Orbitolinid Forams	Bracchiopod, Rudist, Crinoid	Miliolid Forams, Biserial Forams, Planispiral Forams, Ostracod, Rudist Fragments	Gastropod, Peloids	Peneroplid Forams, Biserial Forams, Planispiral Forams, Bryozoa, Radiolaria, Intraclasts, Echinoderms
Sedimentary Structures	N/A	*Thalassinoides* Burrows	*Thalassinoides* Burrows Undulatory-Horizontal Laminations	*Thalassinoides* Burrows	Horizontal Laminations Current Ripples	*Thalassinoides* Burrows	N/A

Environmental Interpretation Summary

The majority of the facies identified in the DeBroeck Member were deposited in a shallow marine environment, below fair-weather wave base, with normal temperatures and salinity. Facies 7, 8, and 10 seem to have been deposited in a deeper environment based on their mud content, while Facies 11, 12, and 13 seem to have been deposited in shallower, higher energy environments than the rest of the cored facies because of the allochems and sedimentary structures present. Finally, Facies 14 was likely deposited in a rudist patch reef based on the presence of rudists in growth position.

Diagenesis

Diagenetic processes have affected the texture, porosity, and permeability of the DeBroeck Member of the Rodessa Formation. Diagenetic processes include the formation of micritic envelopes, grain dissolution, recrystallization of intergranular carbonate mud, and the precipitation of calcite, anhydrite, dolomite, and pyrite cements. The paragenetic history of the DeBroeck Member of the Rodessa Formation is summarized in Figure 4.19.

Marine Diagenesis

The formation of micritic envelopes, the complete micritization of allochems, and the formation of bladed calcite cement are common diagenetic processes that modify carbonate sediments on the seafloor (Longman 1980; Bathurst 1966; Boggs 1995; Keith and Pittman 1983). Longman (1980) describes an active marine phreatic zone in which seawater flows readily into the carbonate sediment resulting in the first stage of the diagenetic process. This active marine phreatic zone in combination with endolithic algae

ultimately leads to the creation of micritic calcite rims on allochems and these can be observed in many facies of the DeBroeck Member (Figures 4.3.B, 4.4.D, 4.6.C, and 4.11.C). SEM images of the surfaces of DeBroeck allochems show the development of an irregular external surface created by subhedral to euhedral microspar crystals that are the result of micritization (Figures 4.3.D, 4.5.C, 4.8.E, and 4.13.B) These SEM images also show that the process of micritization creates microporosity in the newly formed microspar (Figures 4.5.D, 4.6.E, 4.11.D, and 4.13.B). Large-scale borings into allochems is also commonly observed in several facies (Figures 4.10.C and 4.15-1.C) and wholesale micritization of allochems may be responsible for the abundance of peloids.

Meteoric Diagenesis

Subaerial exposure and infiltration by meteoric waters is indicated by the presence of abundant secondary porosity in the form of moldic pores, many of which have been subsequently filled with coarse calcite spar (Figures 4.4.C, 4.6.C, 4.8.D, 4.14.B, 4.15-1.B, and 4.15-1.F) (Esteban 1983). Meteoric diagenesis is also likely responsible for the recrystallization of micritic matrix into euhedral to subhedral microspar (Figures 4.3.F, 4.5.C, 4.5.D, 4.6.E, 4.8.E, and 4.13.A).

Burial Diagenesis

Coarse, blocky calcite spar is present in many of the DeBroeck facies and precipitated in intergranular and secondary pores (Figures 4.4.E, 4.6.B, 4.7.C, 4.8.C, and 4.12.E). Basinal fluids have been documented as potentially expelled and pushed through shallower strata, resulting in the precipitation of blocky calcite and dolomite cements (Loucks and Budd 1984). The small amounts of anhydrite cement present within the

DeBroeck Limestones likely formed later than the calcite spar as indicated by anhydrite cement encompassing blocky calcite cement (Figure 4.4 D and 4.4.E). The likely source of the sulphate for the anhydrite is the Ferry Lake Massive Anhydrite, which lies directly above the Rodessa Formation. After this massive anhydrite formed above the Rodessa Formation, water saturated with sulphate likely flowed through the formation, resulting in the precipitation of anhydrite and pyrite cement.

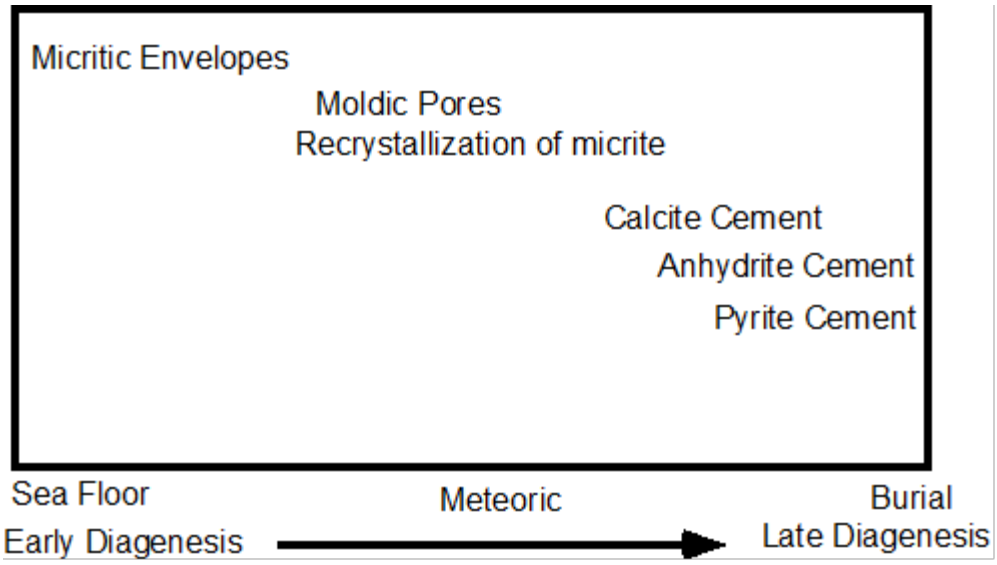

Figure 4.19. Paragenetic history diagram for the DeBroeck Member of the Rodessa formation.

Determination of Pyrite Abundance

Pyrite cement occurs in small amounts throughout the DeBroeck interval. Pyrite precipitation appears to be a late stage diagenetic event as evidenced by its occurrence in moldic pores (Figures 4.13.C, 4.14.D, 4.15-2.H, and 4.15-2.J). In order to estimate pyrite abundance, backscatter SEM images were analyzed using image analysis software. The image analysis software (Cell ^F) provides the ability to specify a particular gray scale

spectrum that is subsequently calculated as a percentage of the entire image. This type of analysis works well with the backscatter images because pyrite shows up as bright areas due to its high atomic density. This method has limitations, however, because it was found that some parts of backscatter images contain shades of grey that duplicate pyrite. Additionally, these images only represent a small part of the total rock volume preserved in core.

Image analysis was conducted on five backscatter images from Facies 7, 8, 9, and 11. The figures show the original image alongside the analyzed image to point out what portions of the image were determined to be pyrite. The image from Facies 7, shown in Figure 4.20, has a pyrite abundance of 7.03%. The image from Facies 8, shown in Figure 4.21, has a pyrite percentage of 19.92%. Two images from Facies 9 were analyzed, (Figures 4.22 and 4.23) and yielded pyrite percentages of 6.04% and 2.61% respectively. The image from Facies 11, shown in Figure 4.24, has a pyrite abundance of 9.51%. The average pyrite abundance for these five images is 9.02%.

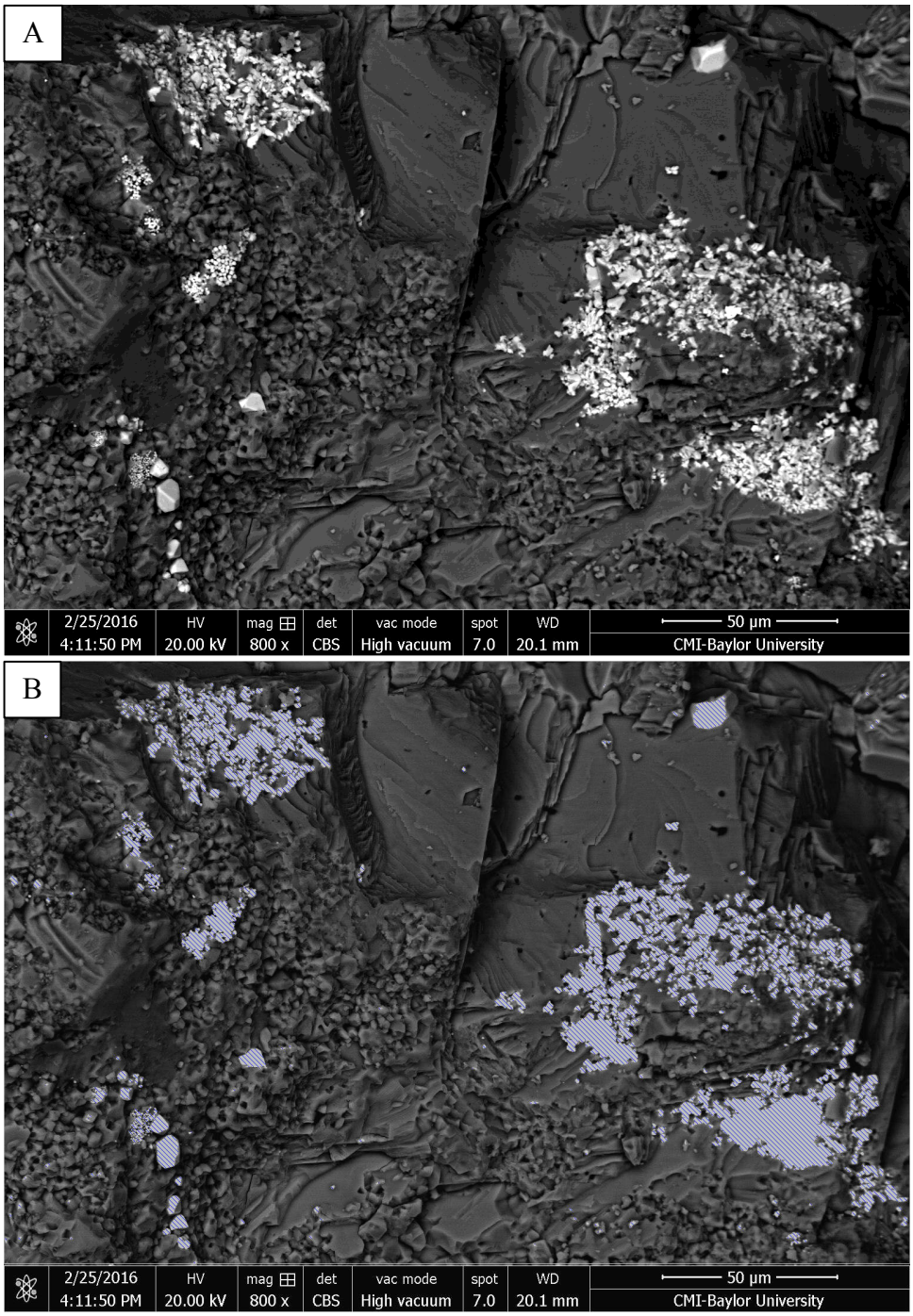

Figure 4.20. Facies 7 pyrite analysis (photos from the McFerren 36-#2 well at 5,041'). A) Backscatter SEM image from Facies 7 showing pyrite (bright areas). B) Same backscatter SEM image after using image analysis software to determine percentage of pyrite (7.03%), which is marked as shaded in areas.

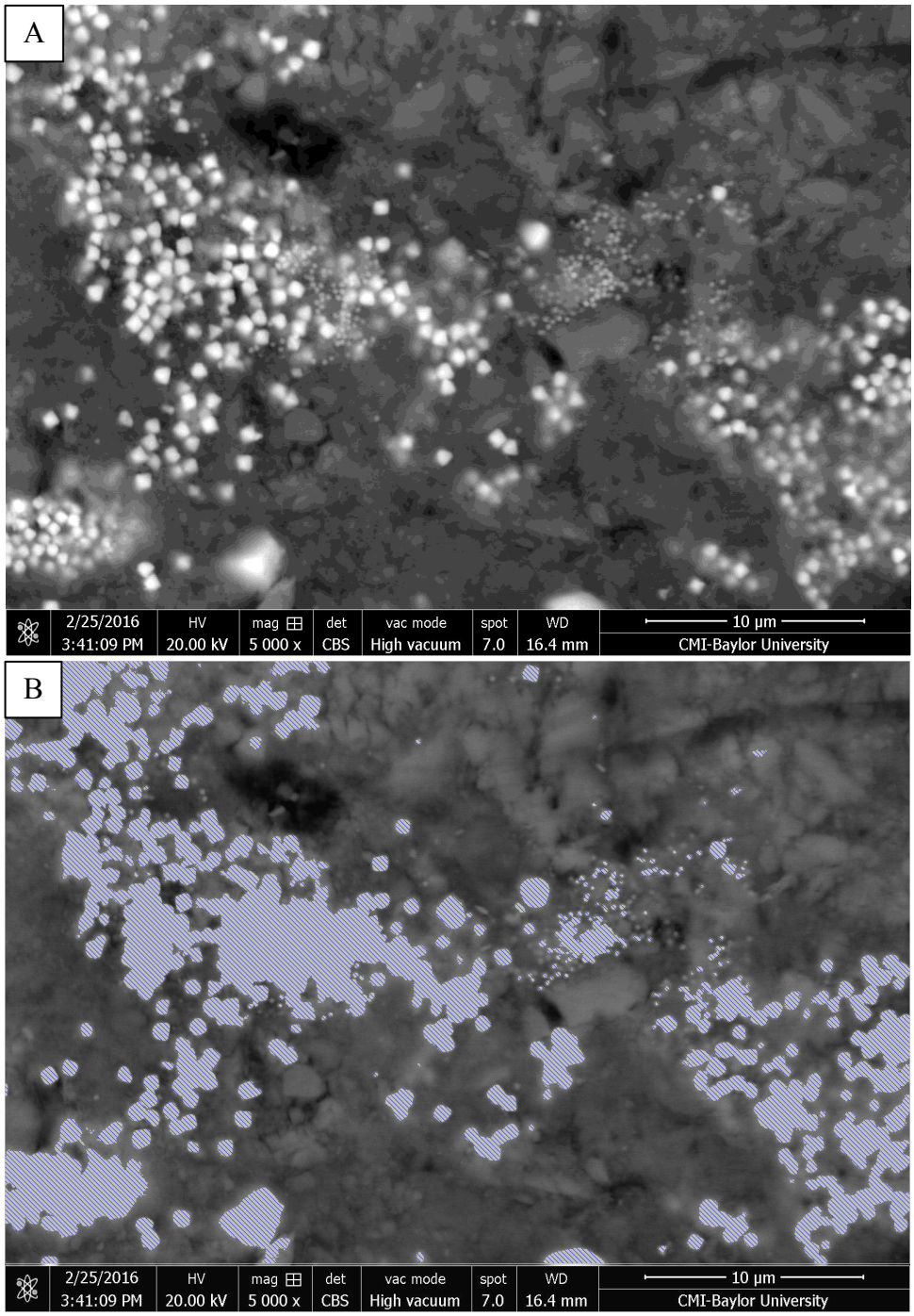

Figure 4.21. Facies 8 pyrite analysis (photos from the McFerren 36-#2 well at 5,043'). A) Backscatter SEM image from a stylolite in Facies 8 showing pyrite (bright areas). B) Same backscatter SEM image after using image analysis software to determine percentage of pyrite (19.92%), which is marked as shaded in areas.

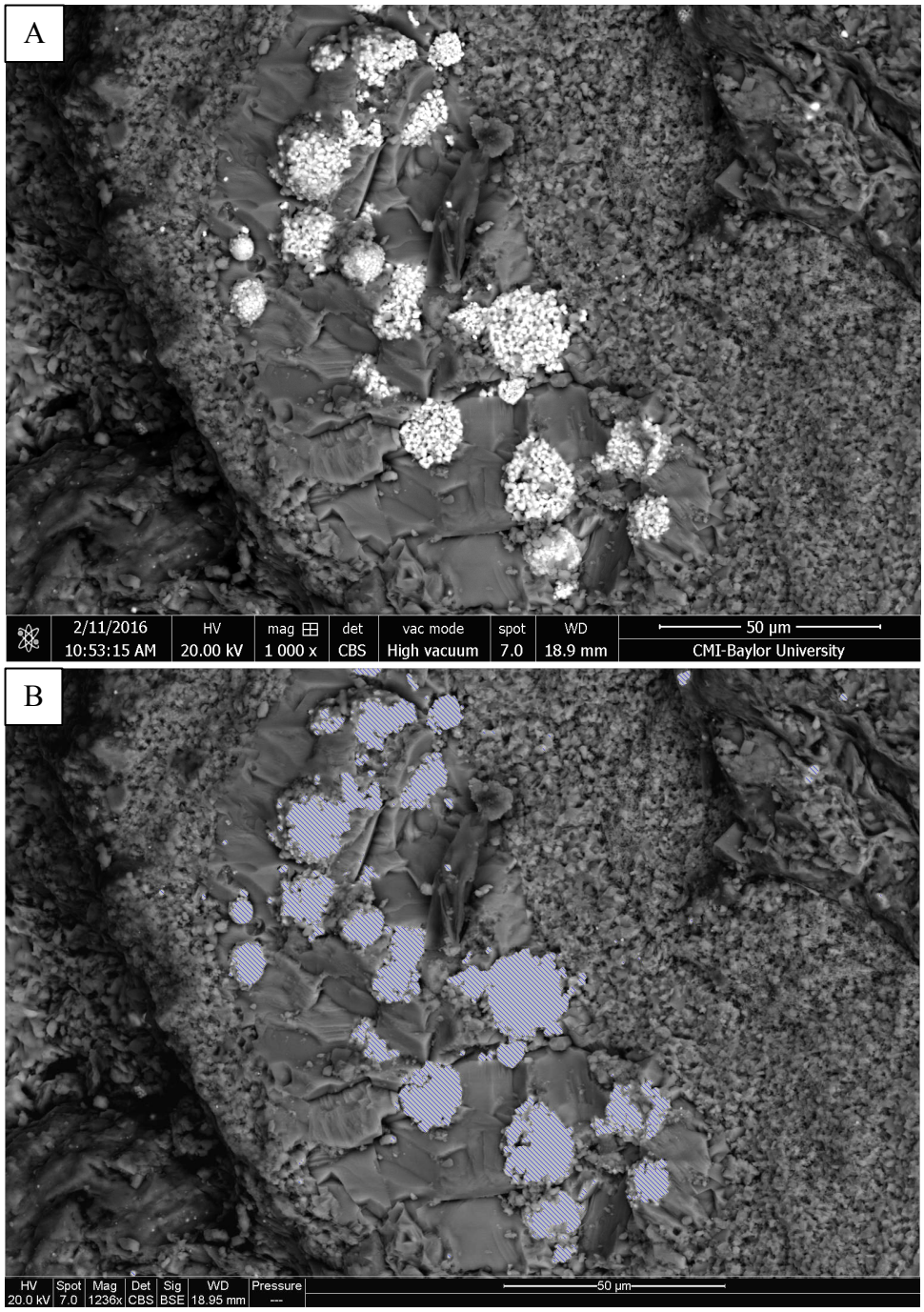

Figure 4.22. Facies 9 pyrite analysis (photos from the DeBroeck 33-#1 well at 5,098'). A) Backscatter SEM image from Facies 9 showing pyrite (bright areas). B) Same backscatter SEM image after using image analysis software to determine percentage of pyrite (6.04%), which is marked as shaded in areas.

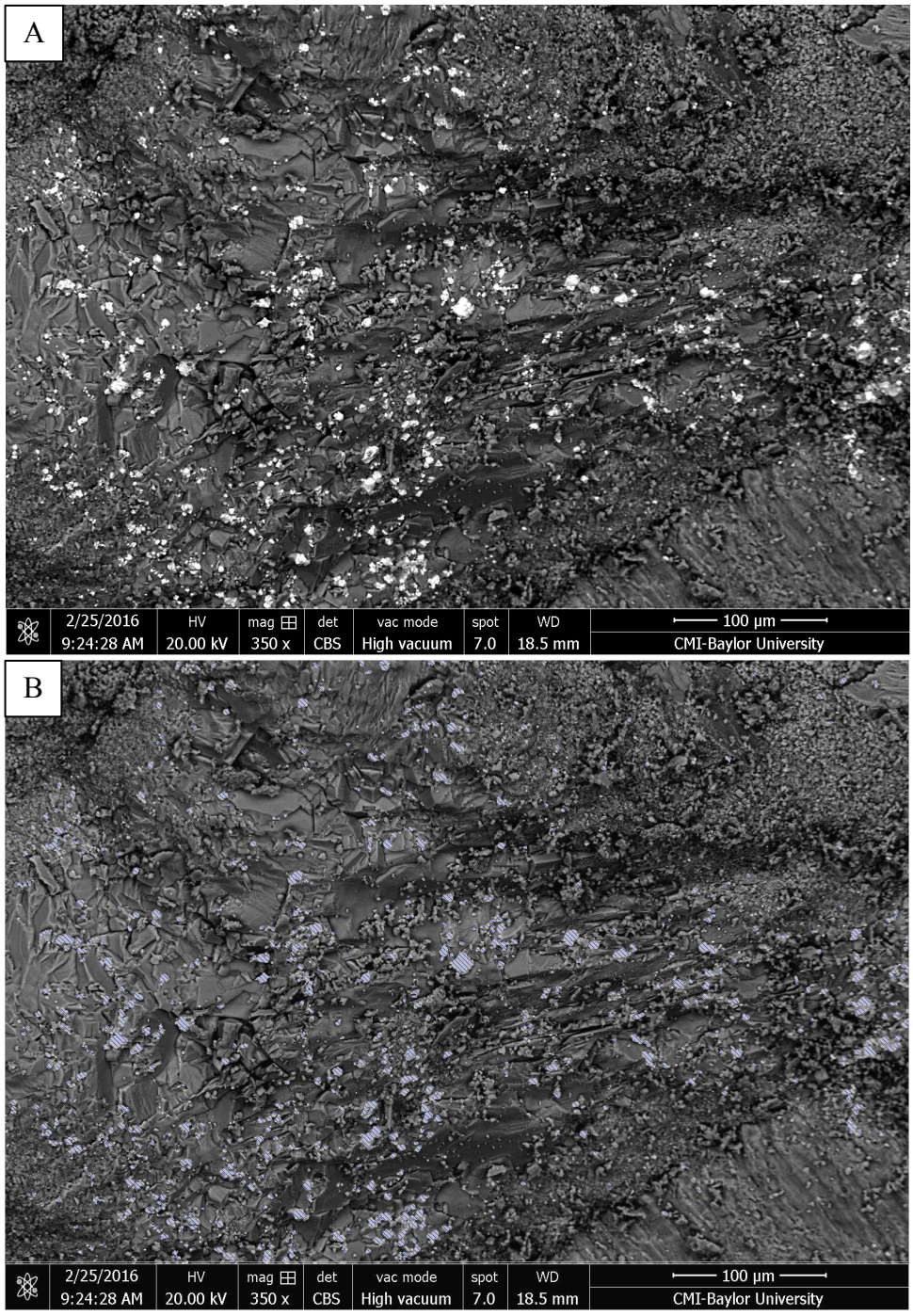

Figure 4.23. Facies 9 pyrite analysis #2 (photos from the McFerren 36-#2 well at 5,071'). A) Backscatter SEM image from Facies 9 showing pyrite (bright areas). B) Same backscatter SEM image after using image analysis software to determine percentage of pyrite (2.61%), which is marked as shaded in areas.

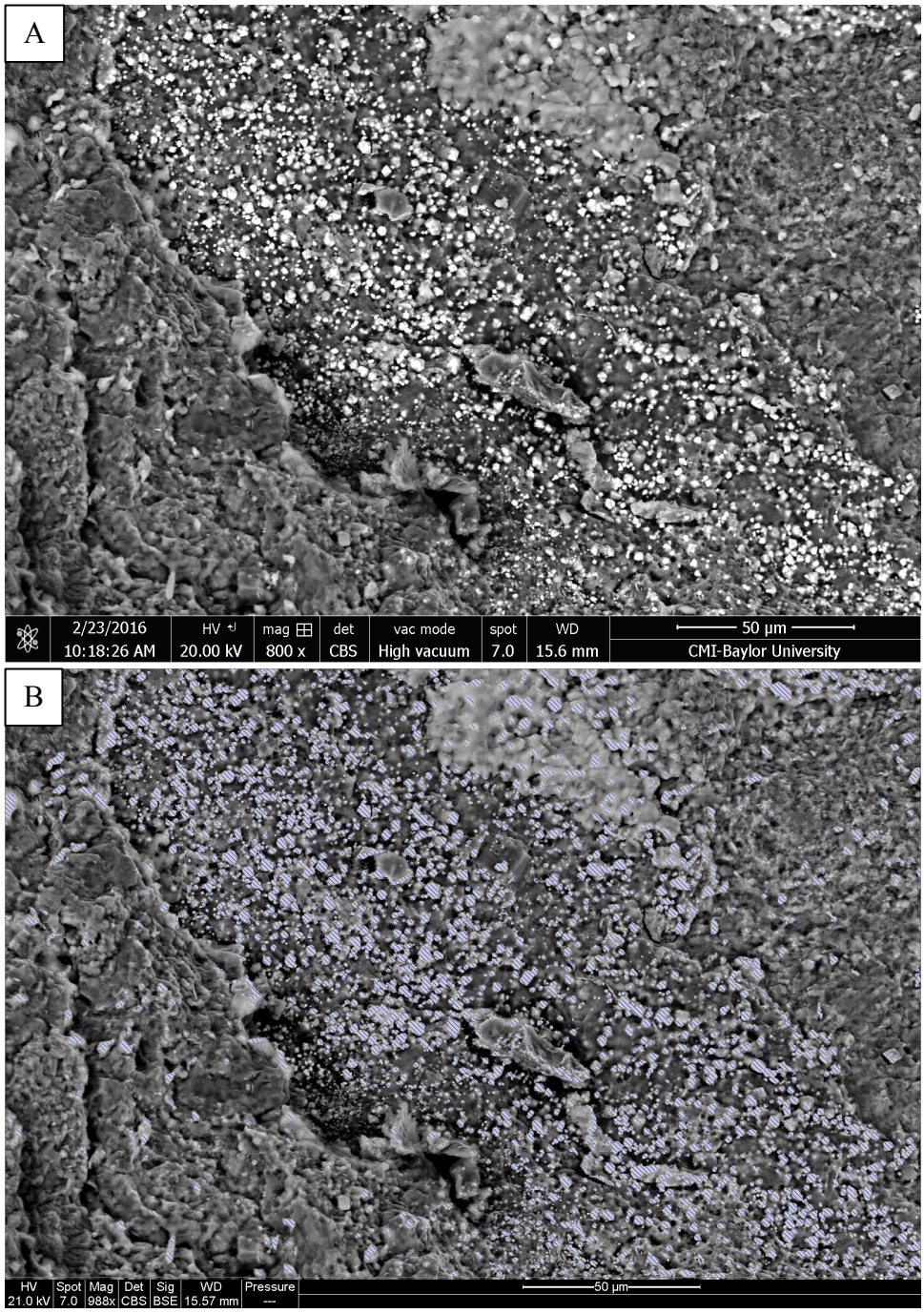

Figure 4.24. Facies 11 pyrite analysis (photos from the McFerren 36-#2 well at 5,061'). A) Backscatter SEM image from a stylolite in Facies 11 showing pyrite (bright areas). B) Same backscatter SEM image after using image analysis software to determine percentage of pyrite (9.51%), which is marked as shaded in areas.

The Effect of Pyrite on Log Response

The image analysis conducted on the backscatter SEM images shows that pyrite can locally be quite abundant. According to Clavier et al. (1976), pyrite can impact a number of different logging tools because of its conductive properties and its high density. For porosity logs, pyrite has little effect on sonic and neutron logs, but has a large impact on density porosity logs (Clavier et al. 1976). Pyrite, which can be highly conductive, also affects resistivity logging tools and Clavier et al. (1976) shows that while the affects can be great, the impact of pyrite largely depends on the frequency of the resistivity tool, the pyrite abundance and connectivity, and the formation water resistivity. This study is concerned with the impact on resistivity logs.

The relationship of frequency and pyrite impact is one that when a higher frequency resistivity logging tool is used, the affect of pyrite is amplified. Laterolog and induction-electric logging tools operate with frequencies ranging from 15 Hz to 1 KHz, while array induction logging tools operate with frequencies around 20 KHz. This means that if an array induction tool is used in a formation containing pyrite, the impact of the pyrite on the log will be greatly amplified. The abundance and connectivity of pyrite within a formation is also very important when determining if there will be an impact from this mineral. For example, pyrite may be highly abundant in a formation, but if the pyrite is only found in localized areas and is not electrically connected then there will be minimal to no impact on the logging tools (Clavier et al. 1976). However, if there is any sort of connectivity between the pyrite nodules in a formation, a pyrite percentage as small as 7% can make the resistivity log completely useless (Clavier et al. 1976).

The two cored wells analyzed in this study both used array induction resistivity tools operating at frequencies ranging from 12 KHz to 72KHz, and these types of high frequency resistivity tools are used in this area almost exclusively. This means that the pyrite effect is amplified on the logs from the two cored wells and the majority of the well logs available in the area. However, pyrite must be present in the formation and electrically connected to have an impact on the log signature. The SEM backscatter images showed that there are portions of the formation that contain zero pyrite and areas that contain concentrations as high as 19.92%, but it must be determined if the pyrite is connected in order to say that the pyrite is impacting the logging tools. While the pyrite image analysis indicates that the pyrite within this formation seemed scattered and localized, it also showed that the pyrite formed preferentially within stylolites. The two images with the highest pyrite percentages were both taken from stylolites within the cores in Facies 8 and Facies 11. The image analysis shows that the pyrite not only forms preferentially within stylolites, but that it forms in relatively high percentages within these stylolites. The stylolites within this core are all horizontal, and in some places there are as many as ten stylolites per inch (Facies 8). Additionally, eleven of the fourteen facies within this reservoir contain stylolites. This means that there are basically abundant horizontal laminations within this interval that are filled with interconnected pyrite.

While it can be shown that the informal DeBroeck Member of the Rodessa Formation contains pyrite in relatively high proportions, and that the pyrite is likely interconnected, the true quantitative effect of this mineral on the petrophysical response cannot be determined with the available data. Therefore, all that can be determined is that

the pyrite within this formation has some effect on the well logs and that this effect could be great in zones with large concentrations of pyrite filled stylolites.

Porosity and Permeability Analysis

Data obtained from the standard core porosity and permeability analyses is presented in Figure 4.25 and Figure 4.26. HPMI analysis was conducted on one core plug from the B. DeBroeck 33-#1 well at a depth of 5,105.9 ft. (Facies 6). The HPMI analysis is used to determine the proportions of different pore sizes and these data are presented in Figure 4.27. The classes of porosity that are identified by HPMI analysis include nanoporosity with a pore throat radius smaller than 0.10 microns, microporosity with a pore throat radius between 0.10 and 0.75 microns, mesoporosity with a pore throat radius between 0.75 and 5.0 microns, macroporosity with a pore throat radius between 5.0 and 25.0 microns, and megaporosity with a pore throat radius larger than 25.0 microns. The HPMI analysis shows that macroporosity makes up 0.5% of the porosity, mesoporosity 22.6%, microporosity 50.7%, and nanoporosity 26.1%. The smallest pore size categories (micropores and nanopores) make up 76.8% of the total pore space within this portion of the core.

Porosity and Permeability Interpretation

Porosity

One of the intriguing aspects of the DeBroeck Member of the Rodessa Formation is that conventional resistivity logs indicate high water saturation even though the Rodessa is known to contain and produce abundant hydrocarbons. One possible explanation is that microporosity and nanoporosity containing irreducible water (bound-

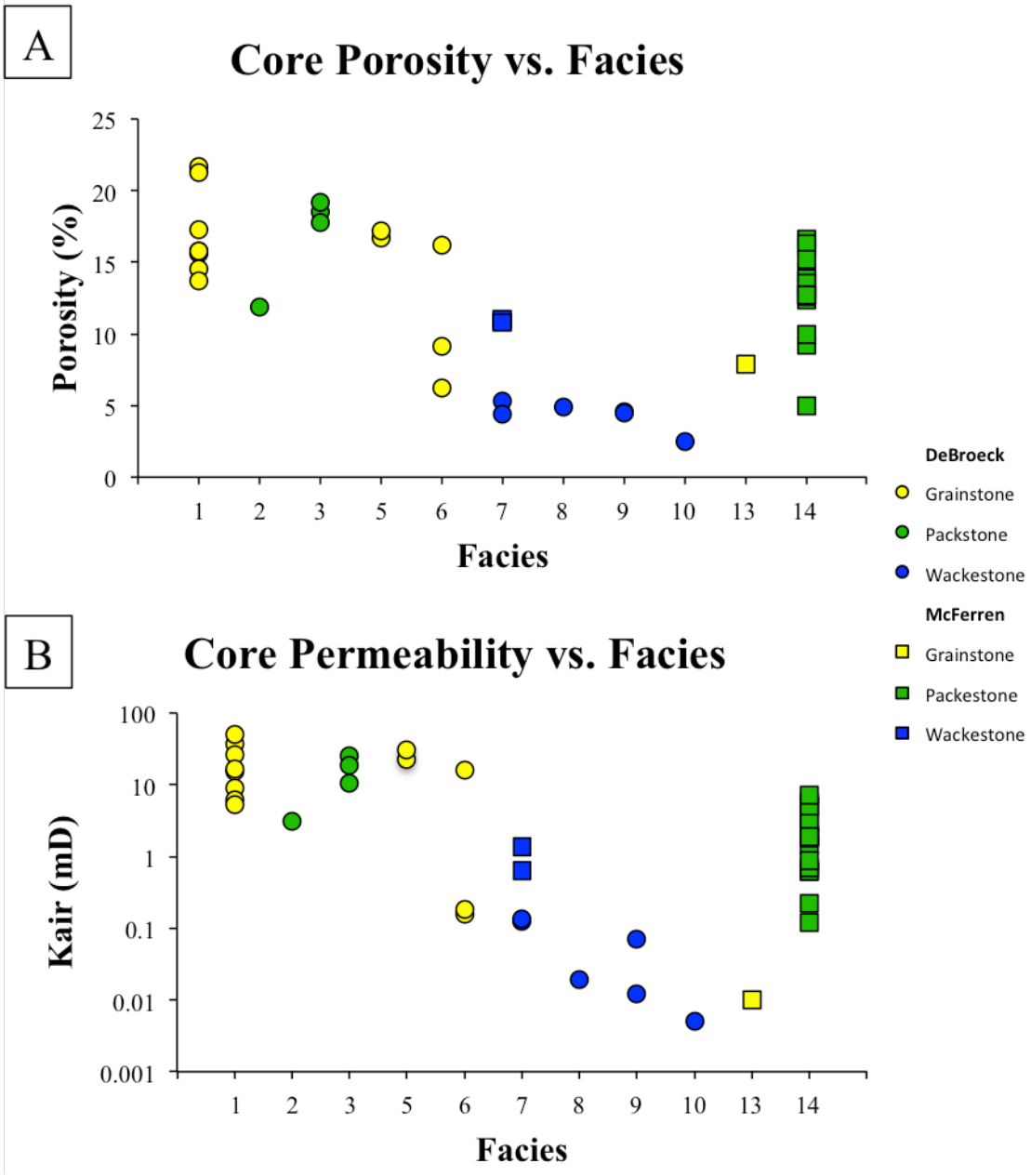

Figure 4.25. Porosity and permeability plots. A) Graph showing the porosity determined from core plugs differentiated by lithofacies; note that no data are available for Facies 4, 11, or 12. B) Graph showing the permeability determined from core plugs differentiated by lithofacies; no data were collected for Facies 4, 11, or 12.

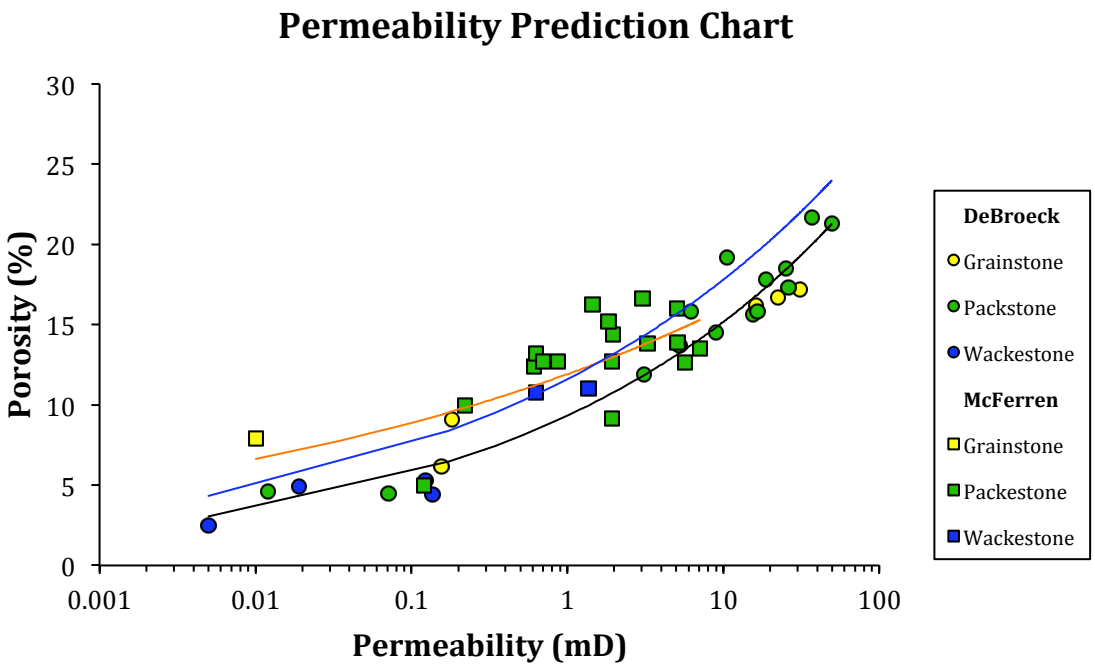

Figure 4.26. Permeability prediction chart showing a plot of core porosity vs. core permeability for both cored wells to help predict permeability. The black line is the best-fit line for the DeBroeck core values ($R^2 = 0.94419$). The orange line is a best-fit line for the McFerren core values and has an ($R^2 = 0.48618$). The blue line is a best-fit line for all of the data points and has an ($R^2 = 0.71553$).

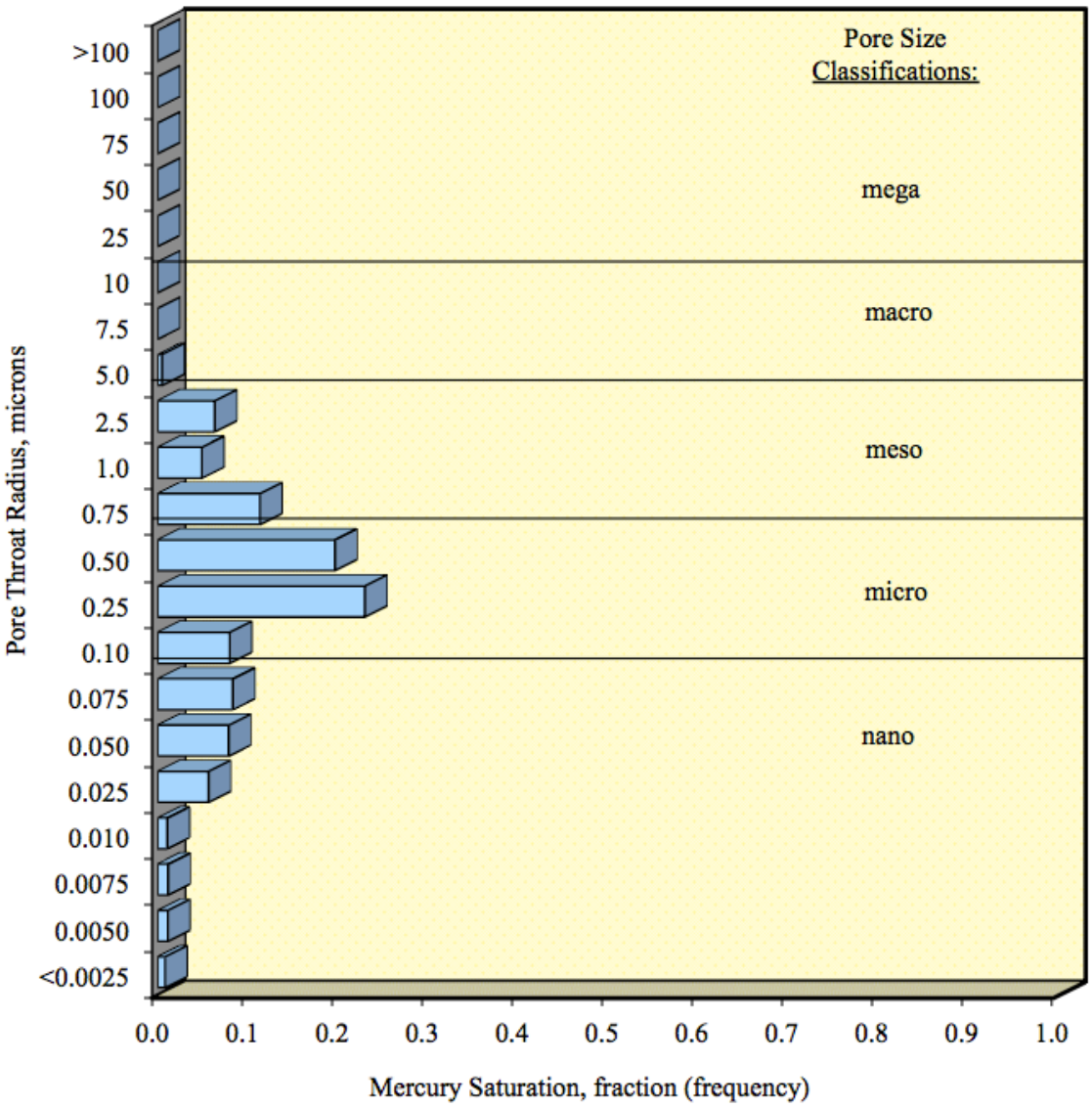

Figure 4.27. Pore throat size histogram showing the relative proportions of different pore sizes, shown as a fraction of mercury saturation, in the B. DeBroeck 33-#1 core at 5,105.9 ft. (Facies 6).

water) are responsible for the petrophysical response. To determine if this is the cause, the nature of the pore space within the informal DeBroeck Member was investigated.

Petrographic microscope and SEM imaging reveal that interparticle, intraparticle, and moldic porosity is common within all of fourteen facies. For example, Figure 4.6.C illustrates interparticle porosity, whereas Figure 4.12.E provides a good example of intraparticle porosity preserved within an orbitolinid foraminifer. High proportions of moldic porosity are illustrated in Figures 4.4.C and 4.6.B. Petrographic analysis also indicates that a large portion of allochems in both cores contain micritized rims as shown in Figures 4.3.B and 4.4.D. The processes of dissolution, cementation, and recrystallization caused by diagenesis likely caused the majority of the moldic and microporosity. Much of the cementation is in the form of microcrystalline calcite, and the microporosity resides in the open spaces between the individual calcite crystals.

In order to determine the proportion of microporosity within the DeBroeck Member, both high-pressure mercury analysis and capillary pressure analysis were conducted. As shown in Figure 4.27, the majority of the pore space at 5,105.9 ft. in the B. DeBroeck 33- #1 well is micro- and nanoporosity. In fact, 76.8% of the porosity at this depth is micro- or nanoporosity. The SEM analysis that was conducted on the two cores showed that microporosity makes up the majority of the porosity throughout the cored interval (Figures 4.5.D, 4.8.D, and 4.14.C). Therefore, even though high-pressure mercury injection was only conducted on one core plug, the assumption can be made that micro- and nanoporosity are present throughout the formation. Micro- and nanopores are typically thought to be so small and have such high surface area and water retention that the water within them is bound (irreducible) and cannot be produced (Keith and Pittman

1983; Asquith and Jacka 1992; Sen 1997). This means that water within micro- or nanopores will still impact the resistivity logging tools and make a reservoir appear wet, even though the water within these pores will never be produced (Sen 1997). If 76.8% of the porosity within this interval is micro- or nanoporosity, only 23.2% of the pore spaces are effective at transmitting fluids.

Figure 4.28 shows the capillary pressure plots from the B. DeBroeck 33-#1 core. The plot for the 5,115 ft. plug shows the graph going asymptotic at around 150 psi, and Table 4.2 shows that at this pressure, 21.2% of the pore space is still water saturated. This means that once the pressure threshold of 150 psi is passed, pressure increases will have very little effect on driving out the remaining fluid saturating the pore spaces. For this depth, the percentage of pore space that can be considered non-effective or irreducible is 21.2%. The plot for the 5,119 ft. plug shows the graph going asymptotic at around 150 psi, and Table 4.2 shows that at this pressure, 32.8% of the pore space is still water saturated. This means that once the pressure threshold of 150 psi is passed, pressure increases will have very little effect on driving out the remaining fluid saturating the pore spaces. For this depth, the percentage of pore space that can be considered non-effective or irreducible is 32.8%.

In addition to micro/nanoporosity, micrite also increase the amount of irreducible water (Keith and Pittman 1983; Sen 1997). The microcrystalline calcite grains that comprise micrite greatly increase the surface area, which in turn increases the areas that attract and hold water (Keith and Pittman 1983; Sen 1997).

High-pressure mercury injection and capillary pressure data shows that micro/nanoporosity are present and abundant in this interval, at least at the depths that

these analyses were conducted. Additionally, the SEM analysis conducted on both cores shows that microporosity and microcrystalline calcite are present and abundant throughout the entire cored interval. The combination of the quantitative data with the SEM data shows that micro/nanoporosity is present and abundant throughout the entire DeBroeck Member. This also means that because of the presence of abundant micro/nanoporosity, there is likely a large amount of irreducible water saturation within this formation (Keith and Pittman 1983; Asquith and Jacka 1992; Sen 1997). Asquith and Jacka (1992) describe that high values of irreducible water saturation will have a large effect on the petrophysical response of resistivity logs and the logs will show the formation as water-wet even if hydrocarbons are present. Therefore, the high irreducible water saturation of the informal DeBroeck Member of the Rodessa Formation produces a misleading resistivity reading and causes the interval to appear wet, even though it contains and produces hydrocarbons in economic proportions.

Table 4.2. Summary of Capillary Pressure Data

	Capillary Pressure (psi)		0	5	15	35	75	150	250	400	650	1,000
Depth (ft.)	Permeability (mD)	Porosity (%)	Initial Saturation (%)	Inlet-Face Water Saturation (% of pore volume)								
5,115	21.5	16.8	100	78.2	44.4	30.5	25.4	21.2	17.8	14.7	11.7	9.3
5,119	0.983	23.8	100	100	88.9	57.5	40.1	32.8	28.2	24.1	20.3	16.9

Permeability

The analysis conducted on both the B. DeBroeck 33-#1 core and the McFerren 36-#2 core indicates that the permeability in the informal DeBroeck Member of the Rodessa Formation can range from as low as 0.005 mD in the burrowed rudistid floatstone facies to as high as 49.6 mD in the burrowed bioclastic pack/grainstone facies. This range of permeability can be attributed to both differences in grain size and mud

content, and diagenetic overprint. Figures 4.3 and 4.9 show the photomicrographs and SEM images from Facies 1 and Facies 7 and suggest that Facies 7 contains much higher mud content and is much finer-grained than Facies 1. However, both facies are impacted by diagenesis and sparry calcite cement. Figure 4.3.B shows that in Facies 1 much of the interparticle porosity is filled with sparry calcite cement. Figure 4.9.C shows an echinoderm fragment surrounded by syntaxial calcite overgrowth that occludes pore space.

Formation Resistivity Factor Analysis

The formation resistivity factor analysis provided data related to the electrical properties of the formation. Most importantly, the analysis helped to determine exact 'm' and 'n' values to be used in the equation to determine the amount of formation water saturation. For the core plug taken from 5,115 ft. the true 'm' value, or cementation factor, was determined to be 2.10 and the true 'n' value, or saturation exponent, was determined to be 1.86. For the core plug taken from 5,119 ft. the true 'm' value was determined to be 2.05 and the true 'n' value was determined to be 2.06.

Saltwater/Formation Water Saturation Analysis

Using Equation 4 (pg. 23), the amount of pore space saturated by formation water was determined for two depths, 5,115 ft. and 5,119 ft. The 'm' and 'n' values that were determined from the formation resistivity factor analysis, as well as the correlation coefficient, the porosity, the formation water resistivity, and the formation resistivity were used within the equation to calculate saturation. It must be noted that because resistivity logs were not run through the Rodessa Formation in the B. DeBroeck 33-#1

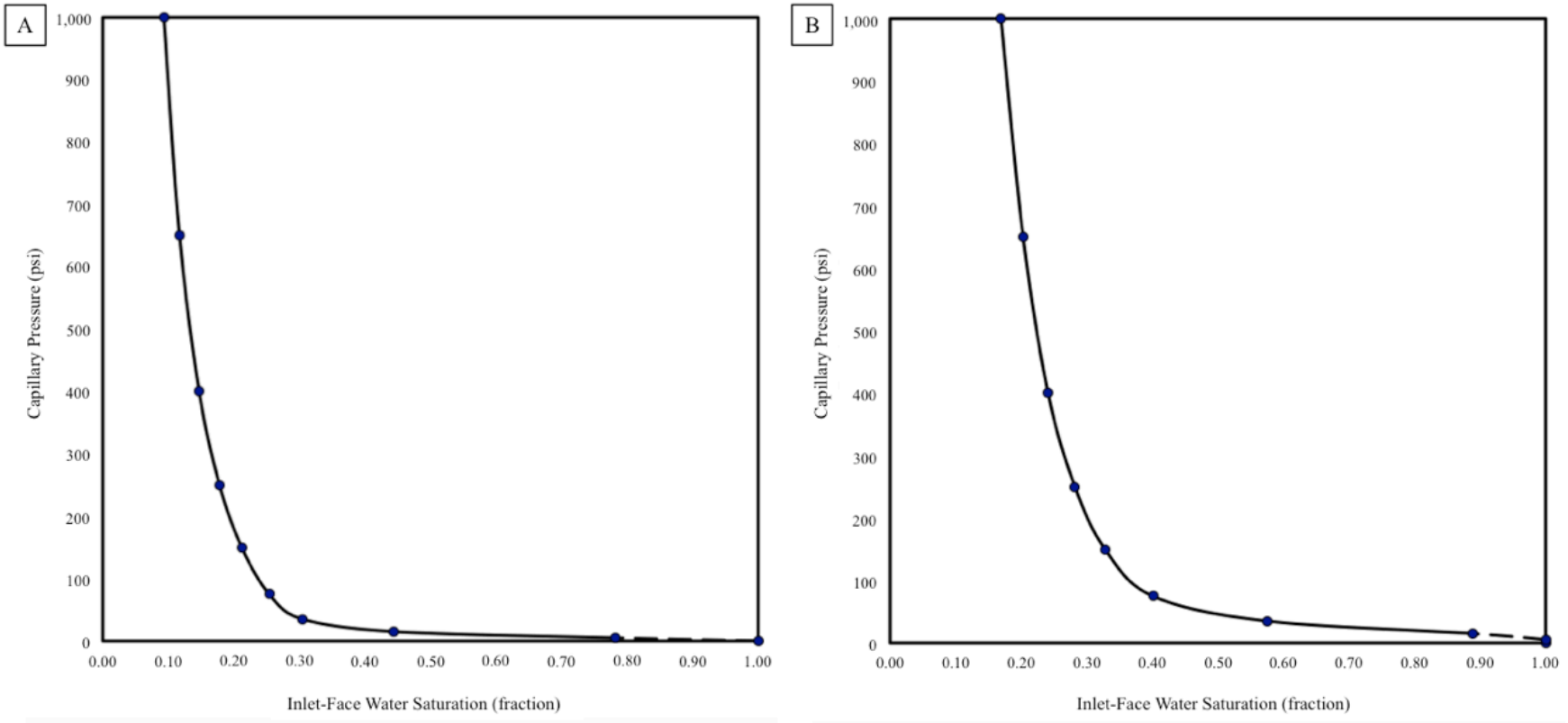

Figure 4.28. Capillary pressure plots from B. DeBroeck 33-#1 well. A) Plot of the capillary pressure data taken from the 5,115 ft. core plug. B) Plot of the capillary pressure data taken from the 5,119 ft. core plug.

well, the value for formation resistivity used in the equation is an estimate from a nearby well. This means that water saturation percentages are an estimate and do not represent the true saturation values of this interval.

For the depth of 5,115 ft. a formation water saturation percentage of 41.5% was calculated. For the depth of 5,119 ft. a formation water saturation percentage of 43.3% was calculated.

Stable Isotope Analysis

Three types of calcite were analyzed for their carbon and oxygen stable isotope ratios. Carbonate mud and rudist shells were analyzed in order to constrain the environmental conditions of deposition and calcite spar was analyzed in order to constrain the timing and conditions of calcite cementation. Stable isotopes are useful for investigating both the temperature of calcite precipitation as well as the source of carbon.

Five fossil shell samples were collected and analyzed from each core. Eleven carbonate mud samples were collected including six from the B. DeBroeck 33-#1 well and five from the McFerren 36-#2 well. Nine calcite spar samples were collected, five from the B. DeBroeck 33-#1 well and four from the McFerren 36-#2 well.

After removing the outliers from the dataset (rf-3, rf-1-mf, rf-2-mf, and rf-4-mf), the rudist shells have $\delta^{13}C$ (‰VPDB) values ranging from 3.19 to 5.31 with an average of 4.09 and $\delta^{18}O$ (‰VPDB) values ranging from -3.19 to -1.99 with an average of -2.56. Based on these oxygen isotopic compositions calculated ocean temperatures at the time of formation ranged from 23.01 °C to 28.96 °C with an average of 25.78 °C.

The analysis of the carbonate mud samples showed that there are two outliers in the dataset (rm-4 and rm-6). After removing the outliers from the dataset, the carbonate

mud has $\delta^{13}C$ (‰VPDB) values ranging from 4.79 to 5.63 with an average of 5.01 and $\delta^{18}O$ (‰VPDB) values ranging from -2.74 to -1.41 with an average of -2.09. Calculated ocean temperatures at the time of formation ranged from 20.22 °C to 26.65 °C with an average of 23.49°C. The similarity in carbon and oxygen isotopic composition of the mud and rudist shells suggests that these carbonate phases equilibrated with the same fluids under similar environmental conditions.

The analysis of the calcite spar samples showed that there is one outlier in the dataset, sample rs-4-mf. The departure from the normal data range may be attributed to sample contamination during drilling. After removing the outlier from the dataset, the calcite spar analysis showed the samples have $\delta^{13}C$ (‰VPDB) values ranging from 4.75 to 5.07 with an average of 4.89, $\delta^{18}O$ (‰VPDB) values ranging from -6.48 to -5.38 with an average of -5.96. Calculated temperatures at the time of formation ranged from 40.81 °C to 47.34 °C, with an average of 44.18 °C. In Figure 4.29, the $\delta^{18}O$ (‰VPDB) and $\delta^{13}C$ (‰VPDB) isotopic values of all the samples and their averages from both cores are plotted to show their distribution. Table 4.3 shows the raw data used for this plot and it also shows the calculated temperatures of calcite precipitation.

In addition to calculating temperatures of precipitation, atmospheric $\delta^{13}CO_2$ at the time of calcite precipitation can also be reconstructed. Using Equation 3, along with the average $\delta^{13}C$ (‰VPDB) and temperature values from the fossil shell and carbonate mud samples, atmospheric $\delta^{13}CO_2$ was reconstructed. The values for the calculations are shown in Table 4.4.

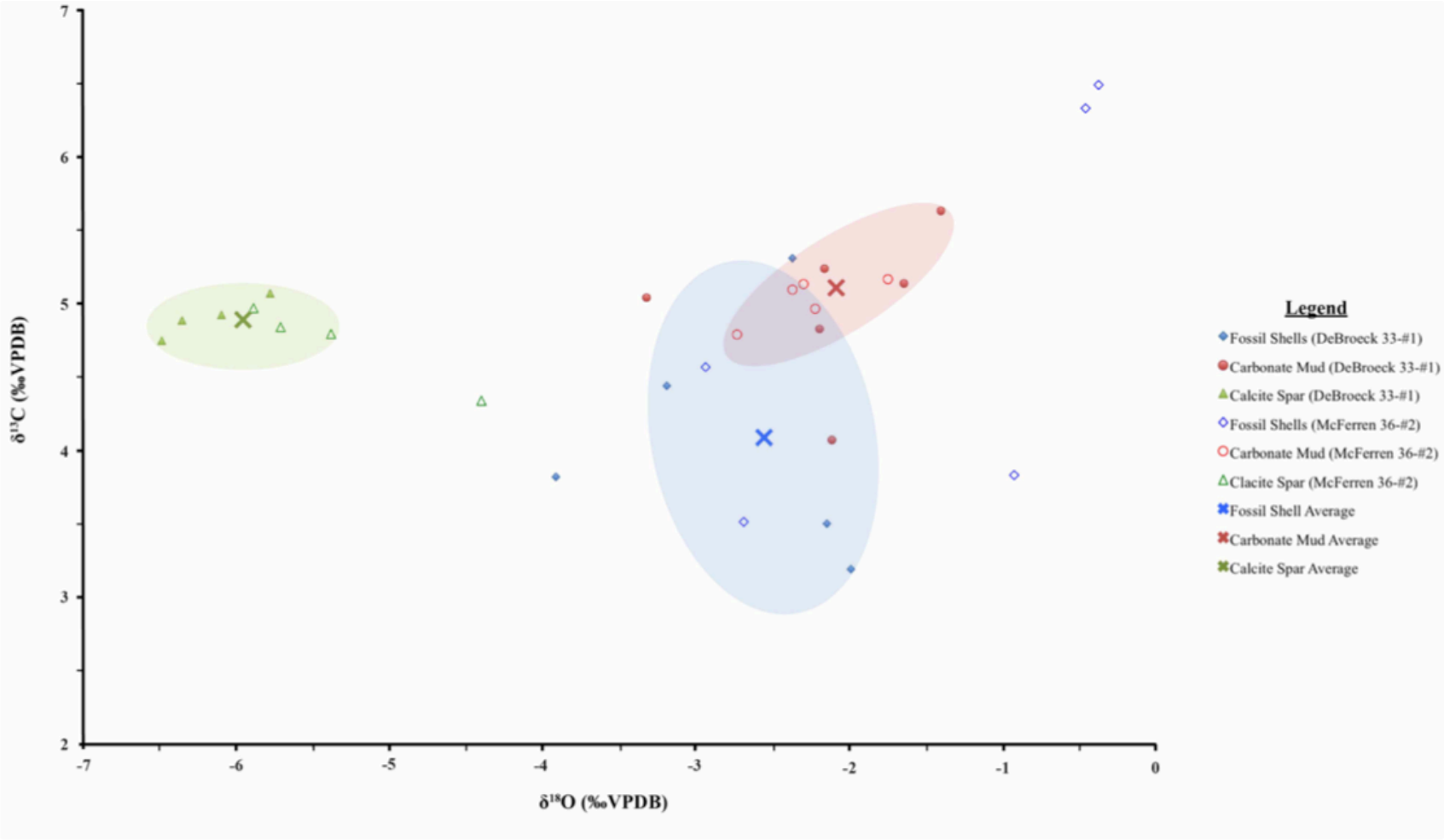

Figure 4.29. Graph showing the $\delta^{18}O$ (‰VPDB) isotopic values plotted against the $\delta^{13}C$ (‰VPDB) isotopic values from the samples taken from both cores, along with the averages.

Table 4.3. Isotopic Values and Calculated Temperatures from Well Core Samples

Sample ID	Well Name	$\delta^{13}C$ (‰VPDB)	$\delta^{18}O$ (‰VPDB)	$\delta^{18}O$ (‰SMOW)	Temp. (K)	Temp. (°C)
Fossil Shell Samples						
rf-1	B. DeBroeck 33-#1	3.51	-2.15	28.65	296.91	23.76
rf-2	B. DeBroeck 33-#1	3.19	-1.99	28.81	296.16	23.01
rf-3	B. DeBroeck 33-#1	3.82	-3.91	26.82	305.87	32.72
rf-4	B. DeBroeck 33-#1	5.31	-2.37	28.41	298.01	24.86
rf-5	B. DeBroeck 33-#1	4.44	-3.19	27.57	302.11	28.96
rf-1-mf	McFerren 36-#2	6.33	-0.46	30.38	289.06	15.91
rf-2-mf	McFerren 36-#2	3.83	-0.93	29.90	291.16	18.01
rf-3-mf	McFerren 36-#2	3.52	-2.69	28.09	299.58	26.43
rf-4-mf	McFerren 36-#2	6.49	-0.38	30.47	288.68	15.53
rf-5-mf	McFerren 36-#2	4.57	-2.94	27.83	300.83	27.68
Carbonate Mud Samples						
rm-1	B. DeBroeck 33-#1	4.83	-2.20	28.60	297.14	23.99
rm-2	B. DeBroeck 33-#1	5.63	-1.41	29.41	293.37	20.22
rm-3	B. DeBroeck 33-#1	5.24	-2.16	28.63	296.99	23.84
rm-4	B. DeBroeck 33-#1	5.04	-3.32	27.43	302.79	29.64
rm-5	B. DeBroeck 33-#1	5.14	-1.65	29.16	294.51	21.36
rm-6	B. DeBroeck 33-#1	4.07	-2.12	28.68	296.76	23.61
rm-1-mf	McFerren 36-#2	5.17	-1.75	29.05	295.00	21.85
rm-2-mf	McFerren 36-#2	4.97	-2.22	28.57	297.28	24.13
rm-3-mf	McFerren 36-#2	4.79	-2.74	28.04	299.80	26.65
rm-4-mf	McFerren 36-#2	5.13	-2.30	28.49	297.65	24.50
rm-5-mf	McFerren 36-#2	5.10	-2.38	28.41	298.02	24.87
Calcite Spar Samples						
rs-1	B. DeBroeck 33-#1	no peaks detected, sample has no calcite		n/a	n/a	n/a
rs-2	B. DeBroeck 33-#1	4.93	-6.10	24.57	318.16	45.01
rs-3	B. DeBroeck 33-#1	4.89	-6.35	24.31	319.68	46.53
rs-4	B. DeBroeck 33-#1	5.07	-5.78	24.90	316.26	43.11
rs-5	B. DeBroeck 33-#1	4.75	-6.48	24.18	320.49	47.34
rs-1-mf	McFerren 36-#2	4.84	-5.71	24.97	315.87	42.72
rs-2-mf	McFerren 36-#2	4.80	-5.38	25.31	313.96	40.81
rs-3-mf	McFerren 36-#2	4.97	-5.89	24.79	316.92	43.77
rs-4-mf	McFerren 36-#2	4.34	-4.40	26.32	308.49	35.34

Table 4.4. Atmospheric $\delta^{13}CO_2$ Reconstruction

Sample ID	$\delta^{13}C$ (‰VPDB)	Temp. (°C)	Atmospheric $\delta^{13}CO_2$ (‰VPDB)
Fossil Shell Average	4.50	23.54	-4.66
Carbonate Mud Average	5.01	24.03	-4.09

Isotopic Interpretation

In order to interpret marine limestone isotopic data it is important to know the range of values expected for different types of environments or marine conditions. The most common conditions under which the types of carbonates within the Rodessa Formation are produced are normal marine, and typical isotopic values for normal marine conditions fall between -2.0 to 2.0 $\delta^{18}O$ (‰VPDB) and 1.0 to 4.0 $\delta^{13}C$ (‰VPDB) (Land 1989). Figure 4.29 shows that, with respect to $\delta^{18}O$, the majority of the fossil shell values and the carbonate mud values plot within or on the fringe of normal marine. This suggests that the carbonate in the fossils and mud formed under normal marine conditions. Note that the average values for both the fossil shells and the carbonate mud are only 0.56‰ and 0.09‰ different from the limit of the normal marine value, in terms of $\delta^{18}O$.

In terms of $\delta^{13}C$, half of the fossil shell values plot within the normal marine range and half plot outside or on the fringe of the normal marine range (excluding outliers). The average fossil shell value is 0.09‰ higher than the range of normal marine $\delta^{13}C$ values. The carbonate mud values, however, are much higher than the range of normal marine $\delta^{13}C$ values, with the average carbonate mud value being 1.01‰ higher than the limit. One possible explanation for the high $\delta^{13}C$ values in the carbonate mud is derivation from brown or green algae. Brown and green algae is reported to have $\delta^{13}C$

values as high 7.00 $\delta^{13}C$ (‰VPDB), while the $\delta^{18}O$ values are within the limits of normal marine conditions (Land 1989).

Application of the temperature of precipitation data using Equation 2 (pg. 22) indicates that the fossil shell samples have an average precipitation value of 25.78 °C whereas the carbonate mud samples have an average precipitation value of 23.49 °C (excluding outliers). These values fall well within the range of temperatures for normal marine conditions, which is typically expected to be between 20-30 °C and suggests formation within the range of normal marine conditions.

In terms of the sparry calcite samples, the fact that the $\delta^{13}C$ values are similar to the fossil shell and carbonate mud values can be described by the spar being 'rock driven'. This means that the spar could have formed from calcite that was dissolved from the shells and mud during diagenesis, and then re-precipitated. In this case, the sparry calcite inherited the isotopic composition of the fossil shells and carbonate mud. However, the very negative $\delta^{18}O$ values of the calcite spar are more difficult to explain. It must be noted that the most common way for $\delta^{18}O$ values to be driven in a negative direction is during recrystallization at higher temperatures. There are multiple ways these recrystallization events can occur. One explanation is that the spar formed from meteoric water during a period of subaerial exposure, which tends to have much more negative $\delta^{18}O$ values than seawater. A second possible explanation is that the spar formed at high temperatures during a deep burial event. The high temperatures experienced during a deep burial recrystallization would drive the $\delta^{18}O$ values in a more negative direction. The average value calculated for calcite spar precipitation is 44.18 °C. This abnormally

high temperature leads to the conclusion that spar within the Rodessa Formation precipitated during deep burial.

Equation 3 (pg. 22) was used along with the average $\delta^{13}C$ (‰VPDB) and temperature of formation values for the fossil shell and carbonate mud samples to reconstruct the $\delta^{13}C$ of the atmosphere at the time of formation. The values, shown in Table 4.3, were calculated to be -4.66 $\delta^{13}C$ for the fossil shells and -4.09 $\delta^{13}C$ for the carbonate mud. Previous studies suggest that for this time period the global atmospheric $\delta^{13}C$ values were around 0.5‰ (Saltzman and Thomas 2012). These reported values are more positive than the calculated values. One possible explanation is that global atmospheric $\delta^{13}C$ experienced an excursion during this time period. However, a more plausible explanation may be that some local perturbation to the carbon cycle caused atmospheric $\delta^{13}C$ values to be more negative. More data in this area is needed to come to a full conclusion on this matter.

CHAPTER FIVE

Conclusions

The DeBroeck Member of the Rodessa Formation in NW Louisiana is comprised of fourteen unique lithofacies: 1) burrowed bioclastic packstone-grainstone, 2) burrowed brachiopod packstone, 3) burrowed peloidal packstone, 4) laminated bioclastic grainstone, 5) burrowed peloidal grainstone, 6) rudistid rudstone, 7) burrowed rudistid floatstone, 8) stylolitic wackestone-packstone, 9) burrowed bioclastic floatstone, 10) burrowed laminated mudstone-wackestone, 11) burrowed stylolitic coated grain packstone, 12) laminated peloidal grainstone, 13) burrowed coated grain grainstone, 14) rudistid framestone. Porosity and permeability analysis conducted on two cores from the informal DeBroeck Member show that, based on the highest porosity and permeability values, the top three reservoir facies are the burrowed bioclastic packstone-grainstone (Facies 1), the burrowed peloidal packstone (Facies 3), and the burrowed peloidal grainstone (Facies 5). Through core description, petrographic analysis, and isotopic analysis the environments of deposition for these facies were determined to range from shallow, open marine, to rudistid patch reef, to low energy marine. Carbon and oxygen isotopic analysis suggest that the fossil shells and carbonate mud within the two cores formed in normal marine conditions with normal water temperatures, whereas the calcite spar within the core formed after the formation underwent burial. Petrographic and SEM analysis were used to show that the formation underwent two stages of diagenesis. The first stage, marine diagenesis, led to micritization and the formation of bladed calcite cement on and around the allochems. The second stage, meteoric diagenesis, resulted in

the dissolution of allochems and the formation of moldic porosity. Burial diagenetic events include calcite, anhydrite, dolomite, and pyrite precipitation.

Porosity within the informal DeBroeck Member is described as interparticle, intraparticle, and moldic. Most of the interparticle and intraparticle porosity is primary whereas the moldic porosity is likely secondary and formed during meteoric diagenesis. Permeability within this formation ranges between 0.005 mD and 49.6 mD; however, the permeability was likely reduced due to diagenesis and the precipitation of calcite cement. Facies 1, the Burrowed Bioclastic Packstone-Grainstone, has the highest porosity and permeability values, which are 21.3% and 49.6 mD, respectively. This porosity within this facies is mostly interparticle and moldic.

High-pressure mercury injection, capillary pressure analysis, and SEM imaging were used to investigate the presence and abundance of microporosity. Microporosity was found to be abundant within both cores. In one area of the core micro/nanoporosity was determined to make up 76.8% of the total pore space within the rock. The large amount of microporosity in this formation leads to high values of irreducible water saturation, which in turn drastically lowers the petrophysical response of resistivity logging tools. This effect on the resistivity tools makes the log signature appear "water-wet", which can mask the presence of hydrocarbons in the formation.

Backscatter SEM images were used along with Cell^F image analysis software to determine the abundance and distribution of pyrite within the informal DeBroeck Member of the Rodessa Formation. Pyrite percentages were found to be as high as 19.92% in places. The pyrite was found to form preferentially within stylolites and was determined to be somewhat interconnected within the stylolites. The high abundance of

pyrite filled stylolites within this formation leads to the conclusion that the pyrite has an effect on the resistivity logging tools. However, the effect of the pyrite on the petrophysical log response cannot be quantified with the available data.

BIBLIOGRAPHY

Archie, G.E., 1942, The electrical resistivity log as an aid in determining some reservoir characteristics: Transactions of the AIME, 146(01), p.54-62.

Asquith, G.B., and Jacka, A.D., 1992, Petrophysics of bimodal porosity: Lower Cretaceous Rodessa limestone, Running Duke field, Houston County, Texas: Gulf Coast Association of Geological Societies, v. XLII, p. 1-12.

Bathurst, R.G.C., 1966, Boring algae, micrite envelopes and lithification of molluscan bioapsrites: Journal of Geology, v. 5, p. 15-32.

Boggs, S., 1995, Principles of sedimentology and stratigraphy: New Jersey, Prentice-Hall, p. 194-235.

Budd, D.A. and Land, L.S., 1989, Geochemical imprint of meteoric diagenesis in Holocene ooid sands, Schooner Cays, Bahamas: correlation of calcite cement geochemistry with extant groundwaters: Journal of Sedimentary Petrology, v. 60/3, p. 361-378.

Bushaw, D.J., 1968, Environmental synthesis of the east Texas Lower Cretaceous: Transactions--Gulf Coast Association of Geological Societies, v. XVIII, p. 416-438.

Choquette, P.W., and Pray, L.C., 1970, Geologic nomenclature and classification of porosity in sedimentary carbonates: AAPG bulletin, v. 54, no. 2, p. 207-250.

Clavier, C., Heia, A. and Scala, C., 1976, Effect of pyrite on resistivity and other logging measurements: SPWLA Seventeenth annual logging symposium, June 9-12, 1976: Society of Professional Well Log Analysts, Houston, TX, United States, Denver, Colo., States United, p. 1-37.

Douglass, R. C., 1960, Revision of the family Orbitolinidae: Micropaleontology, v. 6, no. 3, p. 249-270.

Embry III, A.F., and Klovan, J.E., 1971, A late Devonian reef tract on northeastern Banks Island, NWT: Bulletin of Canadian Petroleum Geology, v. 19, no. 4, p. 730-781.

Esteban, M., and Klappa, C.F., 1983, Subaerial exposure environment in P.A. Scholle, D.G. Bebout, and C.H. Moore, eds., Carbonate depositional environments: AAPG Memoir 33, p. 1-95.

Foll, L., 1980, Field Study: Bethany Longstreet-Rodessa, Desoto Parish, Louisiana: Report on Selected Oil and Gas Fields-North Louisiana and South Arkansas, v. 6, p. 43-46.

Forgotson Jr, J.M., 1963, Depositional history and paleotectonic framework of Comanchean Cretaceous Trinity stage, Gulf Coast area: AAPG Bulletin, v. 47, no. 1, p. 69-103.

Friedman, I., and O'neil, J.R., 1977, Chapter kk. compilation of stable isotope fractionation factors of geochemical interest, in Fleischer, M., ed., Data of geochemistry sixth edition: Geological Survey Professional Paper 440-KK, p. KK1-KK12.

Frizzell, L.G., 1987, Field Study: North Shongaloo-Red Rock Field-Hill Sand (Rodessa) Webster Parish, Louisiana: Report on Selected Oil and Gas Fields-Ark-La-Tex and Mississippi, v. VII, p. 80-84.

Hensel, W. M., 1982, An Improved Summation-of-Fluids Porosity Technique. Society of Petroleum Engineers Journal, v. 22, no. 2, p. 193-102

Hudsmith, S.L., 1987, Field Study: Elm Grove (Extension) Field, Tuscaloosa, Rodessa, Hosston, Caddo and Bossier Parishes, Louisiana: Report on Selected Oil and Gas Fields-Ark-La-Tex and Mississippi, v. VII, p. 76-79.

Jackson, M.L., and Laubach, S.E., 1988, Cretaceous and Tertiary compressional tectonics as the cause of the Sabine Arch, east Texas and northwest Louisiana: Transactions--Gulf Coast Association of Geological Societies, v. XXXVIII, p. 245-256.

Keith, B.D., and Pittman, E.D., 1983, Bimodal Porosity in Oolitic Reservoir–Effect on Productivity and Log Response, Rodessa Limestone (Lower Cretaceous), East Texas Basin: AAPG Bulletin, v. 67, no. 9, p. 1391-1399.

Klitgord, K.D., and Schouten, H., 1980, Mesozoic evolution of the Atlantic, Caribbean and Gulf of Mexico, in Pilõer Jr., R.J., ed., The Origin of the Gulf of Mexico and the Early Opening of the Central North Atlantic Ocean, Proceedings of a Symposium February 20-21, 1981: Houston, Houston Geological Society, p. 100-101.

Land, L.S., 1989, The carbon and oxygen isotopic chemistry of surficial Holocene shallow marine carbonate sediment and Quaternary limestone and dolomite, in Fritz, P., Fontes, J.C., eds.: Handbook of Environmental Isotope Geochemistry, The Marine Environment, v. 3, Elsevier, Amsterdam, Netherlands, p. 191-217

Li, P., 2006, Reconstruction of burial history of strata in the north Louisiana salt basin area: Transactions--Gulf Coast Association of Geological Societies, v. 56, p. 455-471.

Longman, M.W., 1980, Carbonate diagenetic textures from near-surface diagenetic environments: AAPG Bulletin, v. 64, no. 4, p. 461-487.

Loucks, R.G., and Budd, D.A., 1984, Diagenesis and reservoir potential of the Upper Jurassic Smackover Formation of South Texas in Wm.P.S., Bebout, D.G., Perkins, B.F., and Moore, C.H., eds., The Jurassic of the gulf rim: Proceedings from the Third Annual Research Conference of the Gulf Coast Section of SEPM, Austin, Texas, Earth Enterprises, Inc., p. 195-205.

Lowrie, A., Sullivan, N.M., Krotzer, C., Carter, J., Lerche, I., and Petersen, K., 1993, Tectonic and Depositional Model of the North Louisiana-South Arkansas Basin: Gulf Coast Association of Geological Societies, p. 231-238.

Mancini, E.A., Li, P., Goddard, D.A., and Zimmerman, R.K., 2005, Petroleum source rocks of the onshore interior salt basins, north central and northeastern Gulf of Mexico: Transactions--Gulf Coast Association of Geological Societies, v. 55, p. 486-504.

Nunn, J., 1990, Relaxation of Continental Lithosphere: An Explanation for Late Cretaceous Reactivation of the Sabine Uplift of Louisiana-Texas: Tectonics, v. 9, no. 2, p. 341-359.

Rainwater, E.H., 1970, Regional Stratigraphy and Petroleum Potential of the Gulf Coast Lower Cretaceous: Transactions--Gulf Coast Association of Geological Societies, v. XX, p. 145-157.

Roberts, J.L., and Lock, B.E., 1988, The Rodessa Formation in Bossier Parish, Louisiana: Lithofaceis Analysis of a Hydrocarbon-Productive Shallow Water Clastic-Carbonate Sequence: Transactions--Gulf Coast Association of Geological Societies, v. XXXVIII, p. 103-111.

Romanek, C. S., Grossman, E. L,, and Morse, J. W., 1992, Carbon isotopic fractionation in synthetic aragonite and calcite: Effects of temperature and precipitation rate: Geochimica et Cosmochimica Acta, v. 56, p. 419-430

Ross, C.A., 1979, Ecology of large, shallow-water, tropical Foraminifera: Foraminifera ecology and paleoecology: SEPM Short Course no. 6, Houston, Texas, p. 54-61

Saller, A.H. and Moore, C.H., 1991, Geochemistry of meteoric calcite cements in some Pleistocene limestones: Sedimentology, v. 38, p. 601-621.

Saltzman, M.R., and Thomas, E., 2012, Chapter 11—Carbon isotope stratigraphy: in Gradstein, F., Ogg, J., Schmitz, M., Ogg, G., eds, The Geologic Time Scale 2012, Elsevier, Boston, p. 207-232.

Sen, P.N., 1997, Resistivity of partially saturated carbonate rocks with microporosity: Geophysics, v. 62, no. 2, p. 415-425.

Scholle, P.A., 1978, A Color Illustrated Guide to Carbonate Rock Constituents Textures Cements and Porosities: AAPG Memoir, The American Association of Petroleum Geologists, Tulsa, Oklahoma, p. 241

Triyana, Y., 2004, Characterization of Rodessa Formation Reservoir (Lower Cretaceous) in Van Field, Van Zandt County, Texas.

Yurewicz, D.A., Marler, T.B., Meyerholtz, K.A., and Siroky, F.X., 1993, Early Cretaceous carbonate platform, north rim of the Gulf of Mexico, Mississippi and Louisiana: Memoirs-American Association of Petroleum Geologists, p. 81-96.